

Laboratory Investigation of Shear Ruptures:
Supersonic Propagation and Nucleation by Fluid Injection

Thesis by:
Marcello Gori

In Partial Fulfillment of the Requirements for the Degree of
Doctor of Philosophy

Caltech

CALIFORNIA INSTITUTE OF TECHNOLOGY
Pasadena, California

2018
Defended on March 19th, 2018

© 2018

Marcello Gori

ORCID: <https://orcid.org/0000-0002-7380-3723>

All rights reserved

All humanity is one undivided and indivisible family. I cannot detach myself from the wickedest soul.

Mahatma Gandhi

To my family.

Acknowledgements

Having graduated from Italy and completed an internship at Airbus, beginning a PhD at Caltech represented a once-in-a-lifetime opportunity. After a one-year “adventure” with professor Dale I. Pullin in his computational fluid dynamics group, I had the chance to join the laboratory earthquake dynamics group of professor Ares J. Rosakis, to whom I am deeply grateful for the opportunity. I can imagine his initial skepticism to accept a student coming from a research group focused on computational fluid dynamics, with the endeavor of starting a PhD career in experimental solid mechanics. However, not only he has offered me the opportunity, but he has always been an incredibly supportive advisor valuing my creative scientific spirit and fostering it to the research in solid mechanics.

None of this would have been possible without professor Nadia Lapusta, who interviewed me and decided to support my application. She has thereafter represented a fundamental guide throughout my PhD, enriching my work with her vast understanding of solid mechanics and geophysics, which, together with

her long-lasting experience in applied mathematics and numerical simulations, has represented a milestone throughout the years at Caltech. Ares and Nadia have grown over the years an outstanding collaboration, whose benefits I had the fortune to experience. Being advised by both of them, I could always count on an wide perspective, spanning from the minute details to the large-scale view of the research horizons. I am honored to have been their student and to have contributed to their academic bequest.

At Caltech, and more specifically at GALCIT, the spirit of the solid mechanics community is embodied by a key figure, who I had the pleasure to meet during my first year when he taught two terms of the solid mechanics course, professor Guruswami “Ravi” Ravichandran. Many would describe him as a great human being. His gentle and unassuming nature hide an incredibly deep knowledge of the field, which make him a very influential individual in the community. I personally recall two distinctive traits: his astonishing memory (he memorized the notes of his entire course); and his gentleman way of providing suggestions for my research, with the care of complementing my work to instill a sense of security and satisfaction, like a parent would do. The long-lasting friendship between Ares and Ravi, which began during their years at Brown University, enriched their careers and, most importantly, their personal lives.

Together with my advisors, Nadia and Ares, and Ravi, I would like to thank professor José E. Andrade for having accepted to be a member of my thesis committee. I am especially grateful for the support over the years, starting from my candidacy exam and concluding with my PhD defense. I had the opportunity to take two courses with José, one on plasticity and the other one on porosity, and I can state that he is a very fine instructor, whose clarity and attention for details led me to appreciate those topics to the fullest.

I would also like to extend my gratitude to Vito Rubino. He started at

Caltech as a post-doctoral scholar and then became a research scientist, a position that he is still recovering. Vito has been more than an officemate and I consider him a companion of research adventures. He was a guide in the initial portion of the PhD, and introduced me to the earthquake dynamic laboratory and its protocols. As I became more independent, Vito has always been available for scientific discussions, especially to clarify key discoveries prior to the group meetings, where he or I could present them to Ares and Nadia.

From behind the scenes, there are two people, who undoubtedly contributed to the success of my PhD: Michael (Mike) Mello and Emilio Graff. Emilio taught a course on experimental methods, which I took during my first year at Caltech. Despite it being characterized by an intense workload, due to the large amount of material covered, Emilio and I soon developed a sense of mutual respect and appreciation which we preserved over the years. He is the person that introduced me to the secret of the experimental world once I joined Ares' earthquake dynamic laboratory. I am grateful for the undivided help he provided me then, leading to the design and assembly of the fluid injection setup, which, with few upgrades over the years, is the one still used in Ares' laboratory nowadays.

I have the privilege to call Mike my friend. I served as a TA for Mike's experimental course twice but, most importantly, I had the occasion over the years to learn from him the passionate and meticulous approach to the scientific problems. Michael has a minute attention for the details, which, together with his sharp critical thinking, guarantees him a thorough knowledge of every aspect under his interest. Mike and I openly shared our researches and unpublished results, driven by the natural trust and respect that characterized our friendship since the very beginning. Mike has an innate sense of ethics and justice which has been a driving light during my years at Caltech and, being an example for the students he teaches to, I wish he can spread his philosophy and approach to

research far into the academic world. I am honored to have met such a special human being.

Vahe Gabuchian has been a graduate student in Ares' group before me. I am grateful for the time he dedicated me teaching how to polish and bead blast the Homalite specimens. I followed his meticulous attention to reproduce analogous surface conditions for his specimens in order to maximize the repeatability of the experimental conditions. This guaranteed the best surface preparation for my samples, during the following years, when I worked autonomously. In addition, he also trained me on how to use the loading frame, the laser vibrometers, the laser beam, together with all the components of the setup, and the Cordin high speed camera, which I eventually abandoned in favor of the HPV-X that Vito introduced in the laboratory for ultra-high-speed digital image correlation.

Of the many incredible people I have met over the years at Caltech, I had the fortune to become close friend with few of them. In particular, I would like to mention Federico Bosi, Morgane Grivel, Pablo Guerrero, Panagiotis (Panos) Natsiavas, Matteo Ronchi, Kirsten Siebach and Tom Stokkermans. These few very special people affected my life in such a unique positive way, that I consider them family. Despite some of them already moved to other frontiers, our close affection remains unaltered.

At last, my family, to which I would like to dedicate this thesis and my entire PhD. Their loving support has always represented a certainty, which I am grateful for and I hope I can reciprocate. None of my accomplishments would have been possible without such a solid foundation on top of which I could develop my life and all the achievements in it. Grazie!

Abstract

Shear rupture nucleation and dynamic propagation is a challenging, non-linear, highly interactive process with important practical implications. Here we focus on two aspects of this problem: propagation speeds and shock front radiation from the dynamic crack tip as well as nucleation of dynamic rupture due to fluid injection.

Spontaneously propagating cracks in solids emit pressure and shear waves and are, in part, driven by energy transfer due to them. When a shear crack propagates faster than the shear wave speed of the material, the coalescence of the shear wavelets emitted by the near-crack-tip region forms a shock front that significantly concentrates particle motion. The equivalent scenario involving a pressure shock front should not be possible, since cracks should not be able to exceed the pressure wave speed, at least in an isotropic linear-elastic solid. Here we present full-field experimental evidence of dynamic shear cracks in viscoelastic polymers that result in the formation of a pressure shock front, in addition to the shear one. In that sense, the crack appears to be supersonic. The

apparent violation of classic theories is explained by the strain-rate-dependent material behavior of polymers: the increased wave speeds within the highly-strained region around the crack tip allow for supersonic crack propagation with respect to the (lower) wave speeds at short distances away from the interface, resulting in the formation of the pressure shock front. The crack speed remains below the pressure wave speed prevailing locally, about its tip, in agreement with basic physics and energy considerations of linear-elastic theories.

We find that the shock fronts emitted by the shear cracks in the viscoelastic materials are curved and propose a novel method to quantify the viscoelastic wave speeds of the solids in the dynamic range of strain rates based on the curvature. Only kinematic relationships are used in the method, without the need for the constitutive relationship of the material. Measuring or inferring the material properties at elevated strain rates in viscoelastic solids is a difficult task, because of practical limitations of obtaining accurate measurements in that regime. Under the quasi-elastic solid approximation, in which the strain-rate history is neglected, we use the pressure-wave speed measurements to infer the associated value of the Young's modulus, estimated by assuming a constant value of the Poisson's ratio. We complement these results with the characterization of the Young's modulus at lower strain rates via canonical compressive tests. Our results not only confirm previous findings that the Young's modulus dependence on the strain rate in PMMA is significant but also demonstrate that its variation is more pronounced in the dynamic strain-rate range, with important consequences for the design of structures employing viscoelastic materials that are required to withstand elevated strain rates.

The second part of the study concentrates on the nucleation of shear dynamic rupture due to fluid injection or, more broadly, on the interaction of frictional faulting with fluids. Fluid overpressure is recognized to play a fundamental role

in promoting fault motion. A large number of observations has shed light on the interplay between fluids and faulting, both in natural events and in earth-quakes induced by human activities, such as wastewater disposal associated with oil and gas extraction. Fluids can induce a variety of earthquake source behaviors ranging from unstable, dynamic motions to stable, quasi-static ones, which a number of field studies suggests that can coexist on the same fault areas at different times, depending on the local conditions. In fact, a higher pore pressure plays the dual role of reducing the frictional strength of the fault and of increasing the nucleation size, e.g., the critical length for a shear crack to transition from quasi-static to dynamic motions. However, due to the complexity of the frictional problem at the fault interface, the understanding of which of these two effects prevails remains elusive. The assumption of a critical nucleation length represents a powerful, yet simplified concept, which currently does not include the dependence on the rate of the pore pressure increase.

Here, we explore the effect of the rate of the pore pressure increase on the rupture nucleation. We find that elevated injection rates induce triggering of the rupture at lower pressure values and minimal volumes of the injected fluid, if compared to slow injection rates. For the slow injection rates, we experimentally observe a much larger portion of interface wetted by the fluid and a phase of accelerated slip prior to the dynamic event (quasi-dynamic nucleation process). In some cases, we record much smaller foreshock-like events at the injection site. These findings suggest the presence of a prominent quasi-static nucleation process over the interface. In cases of rapid pore pressure increase, the nucleation process is much shorter in time and much more compact in space, being highly concentrated around the injection location. The dynamic events, once initiated, are qualitatively similar across different injection rates, but quantitatively different, with the slow-injection ones experiencing higher stress drops and higher slips, perhaps due to the effect of fluids on the friction properties.

These findings suggest the need to develop nucleation size estimates that include the rate of the pore pressure increase and motivate further investigation of how friction properties depend on the presence of fluids. The details of the obtained experimental findings, once analyzed through numerical modeling, will place important constraints on the forms of the acceptable friction laws, including the effects of pore fluid pressure and its rate of change.

TABLE OF CONTENTS

Acknowledgements	iv
Abstract	viii
Table of Contents	xii
List of Illustrations	xiv
List of Tables	xli
Introduction	1
Chapter I: Fluid-Injection Experimental Setup	9
Haskel Pump	10
Driving Fluid (Air)	14
Driven Fluid (Water)	15
1.A An informative curiosity on patophysiology of alternating current	20
1.B Relay-based electric circuit to operate the solenoid valve	25
I Pressure and shear shock fronts	28
Chapter II: Pressure shock fronts formed by ultra-fast shear cracks in viscoelastic materials	29
2.1 Introduction	29
2.2 Experimental Setup	31
2.3 Results and Discussion	33
2.4 Methods	41
Laboratory setup	41
Wave speed computation	43
Rupture speed computation	45
Chapter III: Inferring dynamic material properties from curved shock fronts of supersonic shear cracks in viscoelastic solids	50
3.1 Introduction	50
3.2 Experimental Design	52
3.3 Results and Discussion	57
The Strain-Rate Dependence of the Wave-Speeds	57
The Curvature of the Shock Fronts due to Viscoelastic Effects	60
Shock Fronts: a Comparison Between Viscoelastic Solids and Fluids	64
Shock Fronts Tracking Method	68
Deriving the Viscoelastic Material Properties from the Shock Fronts	69

3.4	Conclusions	74
3.A	Rupture propagation regimes through materials characterized by different wave speeds	77
II	Shear ruptures due to fluid injection	80
Chapter IV:	Triggering fault slip by fluid injection: effect on slip stability and dynamic rupture properties	81
4.1	Introduction	81
4.2	Fluid-Injection Experimental Setup	85
	Specimen Configuration and Fluid-Injection Setup	85
	Diagnostics	88
	Local and Global Pressure Measurements	88
	Full-field Imaging and Digital Image Correlation	90
	Strain Measurement System	91
	PMMA vs. Natural Rock	92
4.3	Results and Discussion	93
	Pressure Measurements: Slow vs. Fast Injection	93
	Pressure Diffusion over the Interface	96
	Pressure Tactile Sensor Film	96
	Pressure-Diffusion Model	97
	Rapid Fluid-Injection and Locally-Elevated Slip Rate	102
	Imaging the Fluid Diffusion	104
	Strain measurements unveil non-uniform slip leading to rupture nucleation	107
	Stress variation at the lateral surface during a rapid pressure ramp-up nucleation protocol	109
	Stress variation at the lateral surface during a slow pressure ramp-up nucleation protocol	113
	Detection of a foreshock during a slow pressure ramp-up nucleation protocol	115
	DIC to capture surface motion during precursory activity	119
4.4	Conclusions	122
	Bibliography	125

LIST OF ILLUSTRATIONS

<i>Number</i>	<i>Page</i>
1.1 Newly-developed laboratory earthquake setup featuring a fluid-injection circuit capable of delivering pressurized fluid to the specimen's fault and trigger laboratory-scale earthquakes. The sample contains an interface that mimics a crustal fault prestressed in compression and shear. This setup can host both thin (2D) and thick (3D) specimen configuration and possesses an enhanced capability to control rate of injection and fluid pressure. The diagnostics consists of an ultra high-speed camera, laser velocimeters, and strain gages (not shown in the picture).	10
1.2 Schematic of the fluid-injection setup. The components have been arranged following their natural position on the optical table in Figure 1.1. The light blue arrows indicate the air flow, the darker blue arrows indicate the water flow, and the purple arrow indicates the electrical signal produced by the pressure transducers. The key components in this Figure will be presented in the following sections where the setup is introduced.	11

- 1.3 Representation of an intermittent hydraulic pump with air-driven elastic diaphragm (https://en.wikipedia.org/wiki/Diaphragm_pump). **(a)** The air, in brown, actuates the diaphragm, in black, and pressurizes the water on the left hand side, in blue. The water inlet at the bottom is separated from the the outlet at the top by four ball-valves, dark-gray spheres, which are synchronized with diaphragm’s lateral motion in order to guarantee the correct sealing. **(b)** As the cycle continues, the air deflects the diaphragm toward the right where the water is pressurized and release, while simultaneously the left hand side is replenished with ambient pressure water. **(c)** A similar principle is adopted by the MS-36 Haskel M-Pump, which rather than a deformable diaphragm contains a rigid piston capable of significantly higher pressures (<http://www.haskel.com>). 13
- 1.4 Diagram of the MS-36 Haskel M-Pump performance. The colored lines are loci of the combination of pressure and volumetric flow rate the pump will be able to deliver given a specific pressure by the working fluid, i.e., the green corresponds to 0.52 MPa (75 psi), the pink to 0.69 MPa (100 psi) and the red to 0.86 MPa (125 psi). The blue dash lines are level curves of the required air volumetric flow rate. This Figure was converted to IS units from the original vendor chart. 14

- 1.5 The pressure is regulated via a hand-screw adjuster by compressing a spring, which is connected to a valve (or poppet), inserts **(a)** and **(b)**. As this gets gradually opened, a certain amount of pressurized fluid flows through from upstream, starting to increase the pressure downstream the valve. While the pressure builds up, a diaphragm is compressed against the spring in the opposite direction of the screw adjuster, eventually closing back the valve. At this time, an equilibrium is reached between the screw adjuster exerting a force downwards on the spring and the fluid pressure downstream the valve, exerting an opposite force onto the diaphragm connected to the spring. If a higher pressure is desired downstream, the spring needs to be further compressed via the screw adjuster in order to create a higher force downwards to be eventually balanced by the fluid pressure acting upwards on the diaphragm. Evidently, the downstream pressure cannot physically exceed the one upstream. 16
- 1.6 When unpowered, the solenoid valve is in close position (left). The sealing is guaranteed by a spring and the fluid pressure upstream both acting in closing the plunger. Upon the delivery of electricity to the coil, a magnetic field is generated which interacts with that of the plunger (a magnetic element) driving it upwards and opening the seal. The fluid can now flow downstream (right) as long as the power to the coil is maintained. The characteristic time of opening for this valve is in the order of few tens of milliseconds. 18
- 1.7 Out of a wall outlet in the US. The I-shaped slot (left) can carry up to 15 A and is usually employed for domestic appliances, while the T-shaped slot (right) can carry up to 20 A, usually for commercial or industrial use. 20

- 1.8 Log-log graph of the effect of alternating current (AC) I flowing from left hand to feet – through the heart – as a function of time-duration T (Wang, Wang, and Peng, 2013). 23
- 1.9 The transistor technology has several advantages that made it successful in the relay industry (as much as in many other ones): it consumes less current in the “on” state than the electromechanical counterpart, it doesn’t have wearable-by-usage parts such as the contacts or the moving parts, and it is much faster – electromechanical relays typically require 50 ms to switch, while transistors can be as fast as picoseconds ($1 \text{ ps} = 10^{-12} \text{ s}$). 25
- 1.10 Schematic of the electric circuit to power the solenoid valve (upper-right portion). At the center of the Figure is represented the relay: the green portion represents the safe-for-humans 5 V direct current (DC) powered by a DC generator (lower-left portion); the red side represents the dangerous-for-humans 120 V alternating current (AC) powered by the wall outlet (upper-left portion). When the toggle switch (lower-right portion) is closed, the 5 VDC current is driven to the relay, which will close the 120 VAC circuit and power the valve to switch open. 27

- 2.1 Laboratory setup and the captured supersonic shear ruptures. **(a)** The dynamic rupture is produced on a sample interface (green-shaded area) loaded in compression and shear by a compressive vertical load (yellow arrows). The rupture is triggered by the sudden disintegration of a Ni-Cr wire filament and subsequently propagates spontaneously over the interface. Its dynamics is captured using a speckle pattern applied over a portion of the specimen's surface, ultra-high-speed photography, and DIC algorithms. The inset exhibits the distribution of interface-parallel particle velocity, \dot{u}_1 , 58 μs after nucleation. The white lines highlight the peaks associated to the pressure and shear shock fronts, and the white circles are representative of how the shear shock front is generated by the coalescence of the shear wavelets. An analogous construction – not shown here – applies to the pressure cone. **(b)** The profile of the particle velocity, \dot{u}_1 , along the violet line (at a distance $x_2 = -27.5$ mm from the interface), plotted at time intervals of 5 μs , exhibits two recognizable peaks associated to the pressure and shear Mach fronts. **(c)** The rupture speed versus position along the interface, x_1 , is computed by tracking the rupture tip in the temporal sequence of velocity maps. The comparison with the pressure wave speed in the bulk material, where low strain rates are attained (Figs. 2.3 and 2.6), confirms the supersonic nature of the rupture, $V_r > c_p^{\text{LSR}}$ (see text). At the crack tip, where considerably higher strain rates develop (Fig. 2.3, lower inset), the rupture is locally intersonic, $c_s^{\text{HSR}} < V_r < c_p^{\text{HSR}}$. . 32

2.2 Full-field particle velocities and strain measures for supersonic ruptures. Both PMMA (left) and Homalite-100 (right) exhibit two pairs of shock fronts, the pressure and the shear one (colored dashed lines). The PMMA snapshots correspond to $58 \mu\text{s}$ after the triggering and the Homalite-100 ones to $66 \mu\text{s}$. **(a)** and **(b)**, Interface-parallel particle velocity, \dot{u}_1 . **(c)** and **(d)**, Volumetric strain rate, $\text{tr}(\dot{\boldsymbol{\epsilon}})$. **(e)** and **(f)**, Shear strain rate, ϵ_{12} . The volumetric strain-rate field (**c** and **d**) enhances the presence of the pressure shock front, while “hides” that of the shear Mach cone. The shear strain-rate field (**e** and **f**) does the opposite, by showing a healthy shear shock front and a less developed pressure one. Therefore, the pressure and shear shock fronts, highlighted in colored dashed lines, are traced as the loci of maxima of the volumetric strain rate (**c, d**) and shear strain rate (**e, f**), respectively. The fronts thus determined are then reported in the velocity fields above (**a, b**). . 34

2.3 Strain-rate dependence of the pressure wave speed in PMMA.

The values of the pressure wave speeds have been computed by converting the elastic moduli versus strain-rate data acquired from the literature (Fig. 2.6). Linear-elastic wave relations have been adopted, assuming a density $\rho = 1180 \text{ kg/m}^3$ (measured) and a constant Poisson's ratio $\nu = 0.35$ (Mulliken and Boyce, 2006; Richeton, Ahzi, Vecchio, Jiang, and Makradi, 2007). The blue triangles indicate compressive tests with the exception of the diamonds, which indicate tensile tests. The cyan hexagon represents the value of c_p measured from the inclination angle, as shown in the inset. The horizontal black dashed line represents the rupture speed $V_r = 2.57 \text{ km/s}$, computed by tracking the rupture tip in the temporal sequence of full-field images (Fig. 2.1, see section 2.4). The upper inset exhibits a snapshot of the equivalent strain-rate field, $|\dot{\epsilon}|$, at $58 \mu\text{s}$ after triggering. The strain-rate measurements obtained from the full-field images (insets) are reported on the c_p vs. $|\dot{\epsilon}|$ plot for two locations: at the crack tip (green star in upper inset), and behind the shock fronts ($x_1 = 42 \text{ mm}$, $x_2 = -29 \text{ mm}$) (purple star in the upper inset). The green and purple vertical dashed lines refer to the equivalent strain-rate levels for these near-field and far-field measurements, and the corresponding values of the pressure wave speeds are indicated by the horizontal green and purple dashed lines. The strain-rate level at the crack tip is obtained from a similar test performed on a sample at an angle $\alpha = 29^\circ$ (rather than 30°) under the same loading conditions, by focusing on a smaller field of view, which enables a higher strain-rate resolution (lower inset).

- 2.4 Rupture speed computation via DIC and strain gage measurement techniques. Two nominally identical tests are conducted using either the DIC technique or the strain gages. **(a)** Back-side view of the PMMA sample, where an array of three strain gages has been applied along the interface. These strain stations are positioned approximately 40 mm away from each other, with the first one 40 mm away from the wire's location. The field-of-view window of the speckled pattern is applied on the front side of the specimen and is indicated by a dashed rectangle ($19 \times 12 \text{ mm}^2$). **(b)** Time history of the direct strain in the direction parallel to the interface $-\varepsilon_{11}$, measured at the three locations shown in Fig. 2.4a. The color of each strain signal matches that of the corresponding locations in Fig. 2.4a. The transit of the rupture is associated with the initial peaks, where positive sign of $-\varepsilon_{11}$ indicates compression, in accordance with the right-lateral motion of the rupture. The rupture arrival time has been computed considering a threshold of $|\varepsilon_{11, \text{th}}| = 10^{-3}$ (horizontal dashed line). **(c)** Rupture speed computed using the full-field velocity maps obtained with DIC over the small field of view indicated in Fig. 2.4a. The pressure (red lines) and shear (blue lines) wave speeds are reported, where the LSR and HSR conditions correspond to the solid and dashed lines, respectively. This plot confirms that the rupture is propagating supersonically with respect to the low-strain-rate pressure-wave speed of PMMA. The black horizontal dashed line represents the rupture speed averaged between the three strain-measurement stations. 42

- 2.5 Snapshots of full-field images showing the progression of the supersonic rupture. Left column: strain component in the direction parallel to the interface, ε_{11} . Right column: strain rate magnitude $|\dot{\varepsilon}|$. The collection of images is from the large field of view ($128 \times 80 \text{ mm}^2$) and, as the rupture propagates from left to right in the positive x_1 -direction, each image corresponds to a snapshot from 18 to 68 μs , every 10 μs . In analogy with Fig. 2.2, a double pair of shock fronts is clearly discernible, as they become well developed in the later frames. 44

2.6 Strain-rate dependence of the pressure wave speed in PMMA.

The values of the pressure wave speeds have been computed by converting the elastic moduli versus strain-rate data acquired from the literature reported in the legend. Linear-elastic wave relations have been adopted, assuming a density $\rho = 1180 \text{ kg/m}^3$ (measured) and a constant Poisson's ratio $\nu = 0.35$ (Mulliken and Boyce, 2006; Richeton, Ahzi, Vecchio, Jiang, and Makradi, 2007). All symbols indicate compressive tests with the exception of the diamonds, which indicate tensile tests. The cyan hexagon represents the value of c_p measured from the inclination angle (Fig. 2.3, inset). The horizontal black dashed line represents the rupture speed $V_r = 2.57 \text{ km/s}$, computed from the arrival times (Fig. 2.1, see section 2.4). The upper inset exhibits a snapshot of the equivalent strain-rate field, $|\dot{\epsilon}|$, $58 \mu\text{s}$ after triggering. The strain-rate measurements obtained from the full-field images (insets) are reported on the c_p vs. $|\dot{\epsilon}|$ plot for two locations: at the crack tip (green star in upper inset), and after the shock fronts have transitioned ($x_1 = 42 \text{ mm}$, $x_2 = -29 \text{ mm}$) (purple star in the upper inset). The green and purple vertical dashed lines refer to the equivalent strain-rate levels for these near-field and far-field measurements, and the corresponding values of the pressure wave speeds are indicated by the horizontal green and purple dashed lines. The strain-rate level at the crack tip is obtained from a similar test performed on a sample at an angle $\alpha = 29^\circ$ (rather than 30°) under the same nominal conditions, yet by focusing on a smaller field of view, which enables a higher strain-rate resolution (lower inset).

- 2.7 Strain-rate dependence of shear wave speed in PMMA. The shear wave speed values have been computed by converting the elastic moduli versus strain-rate experimental data from the literature reported in the legend, using the plane-strain linear-elastic wave relations and assuming a density $\rho = 1180 \text{ kg/m}^3$ (measured) and a constant Poisson's ratio $\nu = 0.35$ (Mulliken and Boyce, 2006; Richeton, Ahzi, Vecchio, Jiang, and Makradi, 2007). All symbols indicate compressive tests with the exception of the diamonds, which indicate tensile tests. The cyan hexagon represents the value of c_p measured from the inclination angle (Fig. 2.3, inset). The green and purple vertical dashed-lines refer to the equivalent strain-rate levels from the corresponding the green and purple stars presented in Figs. 2.3 and 2.6. The resulting values of the shear wave speeds are indicated by the horizontal green and purple dashed lines. 47

- 2.8 Strain dependence of elastic modulus in PMMA. **(a)** In a quasi-static test on PMMA, $|\dot{\epsilon}| \sim 10^{-4} \text{ s}^{-1}$, the stress shows a linear dependence with strain, up to stresses of 25 MPa and strains of 7×10^{-3} . **(b)** The elastic modulus, computed as the local tangent of the stress-strain curve, does not show the presence of stiffening. **(c)** The full-field equivalent strain $|\epsilon|$ shows that our propagating dynamic cracks does not produce elevated levels of strain (smaller than 3.2×10^{-3}) while inducing elevated levels of strain rate at the crack tip (well above 10^3 s^{-1} , Fig. 2.3 inset below), which would fail to activate hyperelastic effects, in favor of viscoelastic ones. **(d)** Setup employed to produce the results presented in **a** and **b**. Three strain gages equally spaced around the circumference (blue line) of a PMMA cylinder (from the same manufacturer of our samples) measure the vertical component of strain as the load is applied vertically (yellow arrows). 49

3.1 Laboratory setup and the captured supersonic shear ruptures. (a)

The dynamic rupture is produced on a sample interface (red-shaded area) loaded in compression and shear by a compressive vertical load (green arrows). The rupture is triggered by the sudden disintegration of a Ni-Cr wire filament and subsequently propagates spontaneously over the interface. Its dynamics is captured using a speckle pattern applied over a portion of the specimen's surface, ultrahigh speed photography, and DIC algorithms. The inset exhibits the full-field strain-rate magnitude, $|\dot{\epsilon}|$, 58 μs after nucleation. The white lines highlight the peaks associated to the pressure and shear Mach cones, and the white circles are representative of how the shear shock front is generated by the coalescence of the shear wavelets. An analogous construction – not shown here – applies to the pressure cone. (b) The profile of the strain-rate magnitude, $|\dot{\epsilon}|$, along the violet line (at a distance $x_2 = -16.5$ mm from the interface), plotted at time intervals of 6 μs , exhibits two recognizable peaks associated to the pressure and shear shock fronts. (c) The rupture speed versus position along the interface, x_1 , is computed by tracking the rupture tip in the temporal sequence of velocity maps. The comparison with the pressure wave speed in the bulk material, where low strain rates are attained (see chapter 2), confirms the supersonic nature of the rupture, $V_r > c_p^{\text{LSR}}$. At the crack tip, where considerably higher strain rates develop, the rupture is locally intersonic, $c_s^{\text{HSR}} < V_r < c_p^{\text{HSR}}$.

- 3.2 Snapshot of the shear strain-rate field (top and center left), $\dot{\epsilon}_{12}$, and volumetric strain-rate one (to and center right), $\text{tr}(\dot{\epsilon})$, $51 \mu\text{s}$ after the rupture initiation. The curved shear Mach cone (**a**) and bow pressure shock front (**b**) are traced as the locus of maxima (blue line) of the shear strain-rate field (**a** and **c**) and volumetric strain-rate field (**b** and **d**), respectively. (**d**) The volumetric strain-rate field enhances the presence of the pressure shock front, while 'hiding' that of the shear Mach cone. (**c**) The shear strain-rate field does the opposite, by showing a healthy shear shock front and a less developed pressure one. In (**a**) and (**b**), the red line superimposed to the blue one is the result of a moving average smoothing procedure, which is employed in order to eliminate spurious effects. (**e** and **f**) 3D snapshots of strain-rate magnitude allow the correlation of each location of the shock fronts (red lines) with a corresponding value of strain rate (Fig. 3.3 and 3.5a). 55
- 3.3 Mach cone angle and strain-rate magnitude variation along the shear (**a**) and pressure (**d**) Mach cones obtained from Fig.3.2a and b, $51 \mu\text{s}$ after the rupture initiation. The black portion corresponds to locations along the Mach cone in proximity to the rupture tip, which gradually turns green while moving away from it. (**b**) The shear Mach cone angle, computed by differentiating the shear Mach cone with respect to x_2 , is higher in proximity to the crack tip ($\approx 34^\circ$), and gradually reduces moving away from it ($\approx 30^\circ$). Similarly, (**e**) the pressure shock front angle approaches 90° close to the rupture tip and decreases to about 65° away from it. (**c**) The strain-rate magnitude along the shear Mach cone varies between 2×10^2 and $4 \times 10^2 \text{ s}^{-1}$, while (**f**) the one along the pressure shock front varies between 1.5×10^2 and $1 \times 10^3 \text{ s}^{-1}$ 56

3.4 Shock fronts profiles and local inclination angles. A shock front (thick darker blue and purple lines) is formed as the coalescence of multiple wavelets (thin lighter blue and purple lines) emanated by the rupture tip at several time instances, as it propagates along the interface. As a shear wavelet (thin lighter blue lines) travels through the viscoelastic solid, it encounters regions at different levels of strain-rates, loses circularity and, consequently, the locus of points of tangency with the Mach cone assumes a curvature (black dashed lines). Two consecutive wavelets are emanated at a distance $dx_1 = V_r(t) dt$. Due to their proximity with each other, they follow the same strain-rate history during their propagation. The additional distance traveled by the first of the two is $c_s(t) dt$ (inset), while $V_r(t) dt$ is the distance traveled by the rupture tip before emitting the second wavelet into existence. The shear Mach cone local inclination angle β_s is computed by using the general formula $\beta_s = \sin^{-1}(c_s/V_r)$, provided that the local values of c_s and V_r are considered. In addition, the pressure shock front forms ahead of the shear one, as a testimony that the rupture tip exceeds the pressure wave speed of the undisturbed, bulk material ($V_r > c_p^{\text{LSR}}$) (see chapter 2). The small field of view (Fig. 3.5, insets) highlights the presence of an offset – or “process zone” – between the two shock fronts at the interface ($x_2 = 0$), which is related to the presence of a high strain-rate region ahead of the rupture tip. The normality ($\beta_p \rightarrow 90^\circ$) of pressure shock front at the interface ($x_2 = 0$) is an indication of the high levels of strain rates and the generation of a subsonic region ($M_p < 1$) between the front and the rupture tips. Moving away from the interface ($x_2 \neq 0$), the shock front curves and loses strength until, at some point, the strain-rate level behind it is not high enough for the pressure wavelets to outrun the rupture tip, which is thus supersonic ($M_p > 1$) with respect of that region. The x_1 - t -diagram – at $x_2 = 0$ – qualitatively shows the coalescence of

- 3.5 Strain-rate dependence of the shock fronts inclination angles **(a)** and the local pressure and shear wave speeds **(b)**. **(a)** The shock inclination angles are calculated by differentiating the shock fronts (Fig. 3.2, red lines) with respect to the x_2 -direction (Fig. 3.3b and e) and at each coordinate along the shock front the corresponding strain-rate values are obtained (Fig. 3.3c and f). From the values of the angles, **(b)** the shear and pressure wave speeds are computed using equations 3.11 and 3.12. Both profiles increase with strain rate and the pressure one appears to saturate for higher strain rate, corresponding to the shock front approaching the normal condition ($\beta_p \rightarrow 90^\circ$). The black dots, corresponding to points along the Mach cone in proximity to the rupture tip, gradually turn to green moving away from it, analogously to Figure 3.3. The two insets show the shear (top) and pressure (bottom) fields acquired via the DIC technique applied to a small field-of-view ($19 \times 12 \text{ mm}^2$). A thick white line is superimposed to the respective shock fronts to help with their visualization. The three traces represent the volumetric (black) and the shear strain rate (violet) along the interface. The location of their maxima has been included in order to highlight the gap between them, corresponding to the process zone (Fig. 3.4). 70

- 3.6 Young's modulus strain-rate dependence in PMMA. The Young's modulus in the dynamic region of strain rates has been obtained from the knowledge of the pressure wave speed (Fig. 3.5b) by using the linear-elastic wave relations in plane-strain conditions (see equation 3.14), assuming a density $\rho = 1180 \text{ kg/m}^3$ (measured) and a constant Poisson's ratio of 0.35 (Davies and Hunter, 1963; Mulliken and Boyce, 2006; Richeton, Ahzi, Vecchio, Jiang, and Makradi, 2007). The values in the low strain-rate range (yellow triangles), between 10^{-5} and 10^{-2} s^{-1} , have been obtained by performing a compression test on a PMMA cylinder and simultaneously measuring the vertical and hoop strains (see chapter 2, Fig. 2.8). These results are compared to those derived from the literature on PMMA, where the diamonds indicate tensile tests, the hexagons indicate shear tests, and all other symbols indicate compressive tests. The vertical solid black line separates the region of dynamic strain rates, where measurements are performed via SHPB experiments, from the one where servo-hydraulic compressive tests are capable of reaching the required strain-rate levels of interest. 72
- 3.7 Schematics of the shear and pressure shock fronts in different materials and rupture regimes. 79

- 4.1 Laboratory setup featuring a fluid-injection circuit capable of delivering pressurized fluid to the specimen's fault and trigger laboratory-scale earthquakes. The sample has been cut into two identical halves joined together to form an interface that mimics a crustal fault pre-stressed in compression and shear. This setup possesses the capability to control the rate of injection, the fluid pressure and its temporal rate of increase. The diagnostics consists of a high-speed camera, laser velocimeters (only one is used in this study), strain gages (not shown in the Figure), and two cameras, one for measurements of creep (not shown in the Figure), and one for tracking the fluid front as it propagates over the interface prior the dynamic rupture nucleation (not shown in the Figure). 82

- 4.2 Specimen setup front and back side views. A $250 \times 200 \times 12.5\text{-mm}^3$ PMMA sample is separated into two halves by an oblique interface (green-shaded area) at an angle $\alpha = 29^\circ$, and is preloaded by a vertical component $P = 15\text{ MPa}$ (yellow arrows). A thin duct of 1-mm diameter enables the injection of pressurized fluid directly onto the interface. **(a)** On the front side, a pattern of random black dots is painted over a flat white background in a region of $50 \times 40\text{ mm}^2$ in order to allow displacement measurements through the DIC technique. The temporal derivative of the displacement fields produces velocity fields, of which the horizontal component \dot{u}_1 is shown in the inset during a foreshock event (Fig. 4.14). **(b)** On the back side, two strain rosettes are glued just below the interface and 20 mm from each other, which are each capable of measuring three strain tensorial components, separated by 45° angles. These components can be converted into the strains along the fault ε_{11} , normal to it ε_{22} , and the shear one ε_{12} 86
- 4.3 Drawing of the bottom half of the specimen, divided by a cut at an angle $\alpha = 0^\circ$. Over the interface a constellation of holes 0.5-mm in both diameter and depth allows the measurement of the pore pressure as the water fills them and the local pressure is increased. 88

- 4.4 Fluid-injection setup. **(a)** Close-up view of the interface of the specimen about the injection location, on the back side where the strain gages are placed (Fig. 4.2b). The laser vibrometer signal is used to detect dynamic motion in the x_1 -direction associated with the laboratory-scale seismic event and trigger the acquisition of the strain gage signals at high-bandwidth (1 MHz). **(b)** The water, after being pressurized by the pump, crosses a series of components: a high-pressure regulator for manual pressure modulation in the range of few MPa over several minutes to few MPa per second; a pressure transducer for pressure readings upstream of the solenoid valve; a solenoid valve activated by a switch, allowing sharp pressure ramp-up profiles in the order of few MPa per hundred milliseconds; and another pressure transducer downstream with bandwidth capability of 3 kHz. This second transducers measures the fluid pressure just upstream of the duct prior to its delivery to the interface. 92
- 4.5 Pressure ramp-up profiles. Two protocols are employed to deliver pressurized fluid onto the interface of the specimen: (left) a slow pressure ramp-up over 27 minutes; and (right) a rapid one over few hundred of milliseconds, achieved via the quick opening of the solenoid valve. For the sake of clarity, the color code of the pressure data mimics that of the labels of the pressure transducers in Figure 4.4b: purple for upstream of the valve and blue for downstream. The red star indicates the triggering of the dynamic rupture recorded by the laser velocimeter (Fig. 4.4a), which is set at the origin of our temporal scale. The green dashed line represents the resolved normal stress $\sigma_n = P \cos^2(\alpha)$ the fluid pressure is competing with. 94

- 4.6 Pressure measurement from the Fujifilm tactile pressure-indicating sensor film. The sensor changes color as it experiences pressures in the range between 2.4 and 9.7 MPa. The specimen has been loaded to $P = 15 \cos^2(29^\circ) = 11.5$ MPa, which chromatically saturates the pressure film, except in correspondence to the holes (darker dots). The pore-pressure time history at the injection duct mimics that of the gradual ramp up (Fig. 4.5a), while the final distribution over the interface, corresponding to the same conditions the dynamic rupture occurred (at 8.7 MPa), is measured by the holes. 97
- 4.7 Pressure measurement corresponding to the 0.5-mm wide holes using the Fujifilm tactile pressure-indicating sensor film, derived from Figure 4.6. The pore pressure rapidly decays away from the injection duct due to the ambient pressure along the boundaries of the sample. 98
- 4.8 Fluid-pressure distribution over the interface at rupture initiation. The pressure distribution is estimated by numerically solving equation 4.3, where the pressure ramp-up profiles from Figure 4.5 are imposed at the node corresponding to the injection location, for the slow case (left) and the rapid one (right), respectively. The rapid decay of pressure away from the injection channel is due to the ambient-pressure boundary condition along the lateral sides of the interface. The bottom panels represent a slice through the plane $x_3 = 0$ and highlight the substantial different pressure distribution scenario under which the dynamic rupture nucleates. 99

- 4.9 Slip rate temporal history of a loaded specimen. The blue curve represents the data obtained from quasi-static DIC measurements averaged and filtered, while the red curve is an exponential fitting, in compliance to the rate-and-state friction law. After the application of an external load of $P = 15$ MPa, the specimen is left untouched for the entire duration of the test. The slip rate spontaneously evolves from 3×10^{-10} m/s to 10^{-11} m/s. These values, despite being very small, prove that the interface is never fully locked. 100
- 4.10 Fluid diffusion on the interface driven by pressure gradient. (left) Snapshot of the back side of the specimen (Fig. 4.2b) during a slow pressure ramp-up (Fig. 4.5a). For sake of clarity, we present a snapshot from another test, where no pattern for DIC was applied over the interface and the strain gages have been placed on the front side of the specimen. Instead, two $1 \times 1\text{-mm}^2$ squares of retro-reflective tape are positioned corresponding to the strain gages on the back side. The wet portion of the interface has been enhanced and enclosed into blue lines for better visibility. (right) Top view of the interface for the case corresponding to the test exhibited in Figure 4.5a. The wet portion (enclosed by the blue lines) is shown at several temporal instances, indicated by the green label on the right-hand side. Its average length is indicated in millimeters just above the corresponding case, and, at rupture initiation ($t = 0$), amounts to 74 mm. 106

- 4.11 Stress time history during a rapid pressure ramp-up protocol. The shear (top row), fault-normal (center row) and fault-parallel (bottom row) stresses are shown over three time scales: minutes (left column), milliseconds (center column), and microseconds (right column), where the temporal origin coincides with the rupture initiation. Prior to the valve opening (left column) no fluid has been delivered to the interface yet, and strains and stresses accumulate as a consequence of the viscoelastic relaxation of the bulk polymer under load control mode. After the valve opening, in the few hundreds of milliseconds prior to the rupture initiation, the stress redistribution is related to the different slip behavior of patches with respect to the surrounding ones. After the rupture is triggered (right column), a laboratory-scale seismic event is recorded where left-lateral propagation arises. 108

- 4.12 Stress time history during a slow pressure ramp-up protocol. The shear (top row), fault-normal (center row), and fault-parallel (bottom row) stresses are shown over three time scales: minutes (left column), milliseconds (center column), and microseconds (right column), where the temporal origin coincides with the rupture initiation. The delivery of pressurized fluid begins approximately 27 minutes prior to the rupture initiation (left column), promoting slow slip. One must remember that strains and stresses partially accumulate as a consequence of the viscoelastic relaxation of the bulk polymer under load control mode. In the few hundreds of milliseconds prior to the rupture initiation, the stress redistribution is related to the different slip behavior of patches with respect to the surrounding ones. After the rupture is triggered (right column), a laboratory-scale seismic event is recorded where left-lateral propagation arises. 112

- 4.13 Stress time history during a slow pressure ramp-up protocol. The shear (top row), fault-normal (center row), and fault-parallel (bottom row) stresses are shown over three time scales: minutes (left column), milliseconds (center column), and microseconds (right column), where the temporal origin coincides with the rupture initiation. The delivery of pressurized fluid begins approximately 28 minutes prior to the rupture initiation (left column), promoting slow slip and few mini-foreshocks, one of which propagates slip all the way to the surface where the SG-0 station is located (inset in the top left panel). One must remember that strains and stresses partially accumulate as a consequence of the viscoelastic relaxation of the bulk polymer under load control mode. In the few hundreds of milliseconds prior to the rupture initiation, the stress redistribution is related to the different slip behavior of patches with respect to the surrounding ones. After the rupture is triggered (right column), a laboratory-scale seismic event is recorded where left-lateral propagation arises. 116

4.14 DIC full-field measurements after the foreshock event observed in Figure 4.13 (top left). The camera acquires pictures at a rate of one frame every 30 seconds. (left) Cumulative fault-parallel displacement u_1 . The upper half creeps leftwards (blue), while the bottom one creeps rightwards (red). At the center portion of the interface $5 - 6 \mu\text{m}$ of slip are cumulatively accumulated, decaying to less than $1 \mu\text{m}$ towards the side of the field of view. (right) Fault-parallel velocity \dot{u}_1 , at the net of rigid body motion, obtained by applying a first-order forward finite difference scheme on the frames just before and after the foreshock event. The velocity has been rescaled by a factor of $30/0.042$, based on the knowledge of the temporal duration of the event from the strain gage measurement (Figure 4.13, top left, inset). During the foreshock event, the motion is concentrated at the center of the interface and rapidly decays away from it. The color-saturated shapes concentrated just below the center portion of the interface are water droplets escaping from the interface and causing the DIC algorithm to decorrelate (Sutton, Orteu, and Schreier, 2009). 120

- 4.15 Slip (left) and slip-rate (right) temporal histories measured via DIC applied to the experiment presented in Figure 4.13. (left) The red and green lines indicate the slip close to the boundary of the field of view, respectively, along the interface, while the blue one corresponds to the center portion, for which the values underneath the interface have been taken below the water droplets (Fig. 4.14). In order to counteract the random noise and be able to measure such small signals, the values at each of the three locations have been averaged over 11 points (5 per side) along the x_1 -direction, both above and below the interface. Overall the interface accumulates less than a micron of slip during the fluid injection phase, with the exception of the center portion of it, which, at about -8.2 minutes, experiences the foreshock event accumulating $4.8 \mu\text{m}$ of slip over 42 ms. (right) The slip rate is computed from the slip using a first order forward finite difference scheme and averages to 10^{-9} m/s. Since the temporal resolution of the camera is of one frame every 30 s, it cannot resolve dynamic events such as the foreshock. The computed slip-rate peak value of 1.6×10^{-7} m/s therefore represents a lower bound. By rescaling this value by the factor of $30/0.042$, where 42 ms is the duration of the foreshock event measured by the SG-0 station (Fig. 4.13, top left, inset), the value of 1.1×10^{-4} m/s is obtained. 121

LIST OF TABLES

<i>Number</i>	<i>Page</i>
1.1 Estimated effects of alternating currents at 60 Hz (Electrocution, 1998).	22
1.2 Estimated effects of alternating currents at 60 Hz (Fish and Geddes, 2009).	23
1.3 Pathophysiology of alternating current flowing from left hand to feet as illustrated in Figure 1.8 (Wang, Wang, and Peng, 2013). . .	24

Introduction

This thesis is divided in two sub-categories. The first one involves a material investigation of shear rupture behavior within homogeneous viscoelastic solids; the second one focuses on the earthquake source physics in relation to fluid-injection practices.

The limiting speed of spontaneous crack propagation is a fundamental problem that has captivated the interest of the scientific community for several decades due to its implications across multiple scientific and engineering disciplines (Abraham and Gao, 2000; Abraham, Walkup, et al., 2002; Buehler, Abraham, and Gao, 2003; Fineberg and Bouchbinder, 2015; Freund, 1998; Marder, 2006; Needleman, 1999; Rice, 2001; Rosakis, Xia, et al., 2007; Rosakis, 2002; Xia, Rosakis, and Kanamori, 2004). In particular, the study of shear cracks propagating along frictional interfaces is relevant to earthquake physics (Bouchon and Vallée, 2003; Dunham, Favreau, and Carlson, 2003; Ellsworth et al., 2004). Fracture mechanics theories have obtained important insights into the problem by considering energy balance in linear-elastic media with either singular or

cohesive-zone crack tips that consume energy. Under those assumptions, the limiting speed for in-plane shear cracks is indeed the pressure wave speed c_p , while the limiting speeds for other crack modes are even lower – the Rayleigh-wave speed c_R for opening cracks and the shear-wave speed c_s for anti-plane shear cracks (Freund, 1998; Needleman, 1999; Rice, 2001; Rosakis, Xia, et al., 2007; Rosakis, 2002). In an interesting side story, these energy arguments identified a forbidden speed zone between c_R and c_s for in-plane shear cracks (Fineberg and Bouchbinder, 2015; Freund, 1998; Needleman, 1999; Rice, 2001; Rosakis, Xia, et al., 2007; Rosakis, 2002), prompting intensive research on whether such cracks can propagate intersonically; such spontaneous intersonic propagation has been confirmed both experimentally (Fineberg and Bouchbinder, 2015; Rosakis, Xia, et al., 2007; Rosakis, 2002; Xia, Rosakis, and Kanamori, 2004) and by interpretation of seismic and other observations from shallow crustal earthquakes (Bouchon and Vallée, 2003; Dunham, Favreau, and Carlson, 2003; Ellsworth et al., 2004).

More recent numerical studies have shown the possibility to “break” these barriers and attain super-Rayleigh opening-crack propagation or supersonic shear-crack propagation (Abraham and Gao, 2000; Abraham, Walkup, et al., 2002; Buehler, Abraham, and Gao, 2003), using hyperelastic constitutive models in atomistic simulations, where the energy flow into the crack tip is enhanced by the hyperelastic stiffening. Other theoretical and numerical predictions achieved supershear antiplane-crack propagation (Guo, Yang, and Huang, 2003; Guozden, Jagla, and Marder, 2010). In all these cases, the crack propagation speeds are compared to the “nominal” values of the wave speeds based on the linear-elastic properties of the materials for infinitesimal and slow deformation. Similarly, dislocations have also been predicted to exceed speed barriers previously though as energetically unsurpassable (Gumbsch and Gao, 1999; Rosakis, 2001; Weertman, 1967). To the best of our knowledge, the only experimental evidence

of *spontaneously* surpassing these barriers involve intersonic opening-cracks propagation in rubber (Petersan et al., 2004), a hyperelastic material, and intersonic edge dislocations in plasma crystals (Nosenko, Zhdanov, and Morfill, 2007).

In Chapter 2, our experiments on Poly(Methyl Meth-Acrylate) (PMMA) demonstrate the possibility for the crack tip to spontaneously exceed the pressure wave speed with consequent formation of a pressure shock front, in addition to the shear one. When a source (i.e. body) travels through a medium at a speed in excess of that of the wavelets transferring energy among the particles composing the medium, these wavelets coalesce into a sharp front, called shock. Shear cracks have been documented to spontaneously exceed the shear wave speed of the bulk material with consequent formation of a shear shock front (Mello, Bhat, and Rosakis, 2016; Mello et al., 2010; Rosakis, Xia, et al., 2007). These ruptures are commonly referred to as “supershear” or “intersonic”. In these problems, the shear shock fronts arise wherever the rupture speed exceeds that of the wavelets in the medium.

The discovery of shear ruptures exceeding the nominal pressure wave speed and the related formation of the pressure shock front (in front of the shear one) has been enabled by the viscoelastic nature of polymers (like a multitude of other materials), which is characterized by the dependence of the material properties – and thus wave speeds – on the local level of strain-rate. Since the crack tip is a source of high strain-rate (HSR) excitation, it induces and at the same time experiences higher material properties about itself, which determines its acceleration to higher speeds. The crack tip propagation regime is still bounded by the energy considerations, in agreement with the cohesive-zone theories on linear-elastic materials (Rosakis, 2002; Samudrala, Huang, and Rosakis, 2002a,b), and therefore never exceeds the local pressure wave speed, yet it approaches it.

Since the pressure wave speed about the crack tip is significantly higher than that away from it, pressure shock fronts form whenever the pressure wave speed is lower than the rupture speed, i.e., a few millimeters away from the crack tip. These discoveries have important implications for the physics and dynamics of shear cracks such as earthquakes.

In Chapter 3, we develop on this idea by noticing not only the presence of two pairs of shock fronts, the shear and the pressure one, but also the variation of their inclination angle. The persistent, gradual reduction of strain rates away from the rupture tip, determines a reduction in wave speeds, which leads to both shear and pressure shock fronts become shallower. The variation of the inclination angle of the shock fronts is kinematically related to the local wave speed, which, in steady-state rupture propagation conditions, assumes a simple analytical form. The measurement of the inclination angle together with the steady-state rupture propagation speed provides enough information for the direct computation of the wave speeds of PMMA at high strain rates.

The quasi-elastic solid approximation is a useful tool since it allows the derivation of any material property from the knowledge of other two known ones by employing the linear-elastic functional framework, where the two known material properties are a function of the strain-rate and its history (Knauss and Zhu, 2002; Schapery, 1965). Whenever the strain-rate history is uneventful, such as prior to the transition of sharp events like the pressure shock front, it can be neglected and the material properties become a function of the local level of strain-rate only. On the other hand, for the shear shock front, the presence of the pressure one ahead of it represents a strain-rate event, whose history may not be negligible. This adds a complexity in the computation of properties from the shear shock front, which not only depend on the local level of the strain-rate, but also on the past one, in relation to the relaxation time of the polymer, which will

not be explored in this thesis, but certainly represent an interesting development for future work.

In the quasi-elastic solid approximation, the Young's modulus is a non-linear function of the local value of pressure wave speed and Poisson's ratio, which, in general, are dependent on strain rate (Limbach, Rodrigues, and Wondraczek, 2014; Lu, Zhang, and Knauss, 1997; Sane and Knauss, 2001; Tschoegl, Knauss, and Emri, 2002; Yee and Takemori, 1982). However, if a constant Poisson's ratio is assumed (Davies and Hunter, 1963; Mulliken and Boyce, 2006; Richeton, Ahzi, Vecchio, Jiang, and Makradi, 2007), the Young's modulus can be estimated in the dynamic range of strain rates, which would be impossible via the Split-Hopkinson pressure bar (SHPB) experimental technique, which proved to be a very effective tool for the exploration of the behavior of materials under dynamic loading conditions (impacts), such as the peak stress or the ultimate one (Bauwens-Crowet, 1973; Chou, Robertson, and Rainey, 1973; Gama, Lopatnikov, and Gillespie, 2004; Jordan et al., 2014; Mulliken and Boyce, 2006; Richeton, Ahzi, Vecchio, Jiang, and Adharapurapu, 2006; Rittel and Brill, 2008; Siviour, Walley, et al., 2005; Siviour and Jordan, 2016; Walley and Field, 1994). Its relatively simple operating principle, which contributed to its vast diffusion in the experimental mechanics community, is based on compressional (or tensional) waves impacting a sample, which, through a small number of wave reverberations (typically between 3 and 4), achieve internal stress and strain-rate equilibrium (Gama, Lopatnikov, and Gillespie, 2004). However, the inability to achieve stress and strain-rate equilibrium during the initial ramping-up phase prevents this technique from being applied to estimate any material property from the stress-strain relationship. For this reason, our approach to measure the wave speeds from the shock fronts inclination angles represents an interesting alternative to overcome this limitation and expand the set of measurable quantities in the dynamic range of strain rates.

The second part of this thesis concentrates the earthquake initiation via fluid injection into the fault. A laboratory setup has been developed in order to allow the delivery of pressurized fluid on a specimen's fault. Chapter 1 contains a detailed description of all the components this setup is comprised, dividing it in two sections: one upstream of a pressure booster (or pump), the other downstream of it. A pressure booster is a device that is powered by the work of a pressurized input fluid (air) and delivers that pressure, multiplied by a characteristic factor, to an output fluid (water). Upstream of the pump, pressure variations are enabled by a regulator, which is used for coarse adjustments, since pressure changes upstream the pump will be multiplied by the characteristic factor. Downstream of the pump, water can be pressurized up to 16 MPa. A series of components allow the fine adjustment and measurements of pressure, rise time and flow rate. In particular, a manually activated high-pressure regulator allows the reduction of the pressure level from the initial value (16 MPa) to any desired one, where rise times of few MPa per hour to few MPa per second can be achieved. In order to obtain sharper rates of injection, a solenoid valve is placed downstream the pressure regulator. Its characteristic opening time is in the order of few tens of millisecond and enables rates of the order of few tens of MPa per second. Two pressure sensors are placed on either side of the solenoid valve, in order to allow water pressure readings, regardless of the open or closed state of the valve. A needle-valve controls the volumetric flow rate of the fluid.

In Chapter 4, two different fluid-injection nucleation protocols are investigated, one involving slow pressure rate, and the other one involving elevated ones. This study is motivated by the observation of the increased seismic hazard associated to fluid-injection into the ground practices (Ake et al., 2005; Cappa, Guglielmi, et al., 2005; Cappa and Rutqvist, 2012; Dahm, Hainzl, and Fischer, 2010; Ellsworth, 2013; Frohlich, 2012; Gan and Frohlich, 2013; Guglielmi et al., 2015; Keranen et al., 2014; McGarr et al., 2015; Segall, Rubin, et al., 2010; Wei

et al., 2015) or dehydration reactions within or below natural faults (particularly subduction zones) (De Paola et al., 2007; Di Toro et al., 2011; Dobson, Meredith, and Boon, 2002; Jung, Green Ii, and Dobrzhinetskaya, 2004; Miller et al., 2004; Okazaki and Hirth, 2016). Fluids are known to trigger a range of seismic events spanning from earthquakes to slow, creeping motion (Segall, Rubin, et al., 2010; Wei et al., 2015), which had been long thought to be spatially well separated. However, field evidence suggests that seismogenic and creeping fault zones can exhibit both slow-slip and dynamic behavior (Beroza and Ide, 2011; Chen and Lapusta, 2009; Dragert, Wang, and James, 2001; Noda and Lapusta, 2013; Peng and Gomberg, 2010). Yet, the mechanics underling these processes and the conditions that lead to different rupture behavior are not completely understood. The complexity of this problem is related to the interaction of fluid-associated effects and the rate-and-state frictional properties. In the Amontons-Coulomb frictional framework, the shear resistance is linearly related to the effective normal stress via a friction coefficient. By neglecting, for the moment, the effect of the presence of pressurized fluid on the friction coefficient, the pore pressure competes with the normal stress frictionally weakening the fault and ultimately promoting slip. The critical nucleation length for a crack to energetically self-sustain its propagating motion in steady-state slipping conditions (Rice and Ruina, 1983; Rice, Lapusta, and Ranjith, 2001) or quasi-static ones (Liu and Lapusta, 2008; Rubin and Ampuero, 2005; Uenishi and Rice, 2003) is inversely proportional to the effective normal stress. Thus, an increase in pore pressure acts in the direction of increasing the nucleation length, promoting stable slip, as opposed to dynamic one. According to this description, higher levels of pore pressure have a stabilizing effect. However, the dependence of fault response on the rate of pore pressure can play a major role and still remains unexplored. In Chapter 4, we show that in conditions of high rates of pore pressure both the validity of the steady-state and quasi-static assumptions fails, and unstable slip is

promoted for rupture lengths considerably smaller than the critical ones predicted by the theoretical estimates (Chen and Lapusta, 2009; Liu and Lapusta, 2008; Rice and Ruina, 1983; Rice, Lapusta, and Ranjith, 2001; Rubin and Ampuero, 2005; Uenishi and Rice, 2003) and experiments at low rates. A minimal volume of fluid is delivered to the interface prior to the initiation of the rupture, if compared to the slow-rate counterpart. An intermediate phase of accelerated slip prior to the nucleation of the dynamic rupture is also observed, which quickly redistributes the stress among different adjacent patches over interface, drastically accumulating shear stress at those frictionally stronger locations where slip is initially resisted. In cases of high pore pressure rates, this stress redistribution is a lot less dramatic, jeopardizing the ability of anticipating the subsequent dynamic event, which, once initiated, produces effects comparable to the ones arising by the adoption of the low pore pressure rate counterpart.

CHAPTER 1

Fluid-Injection Experimental Setup

In order to investigate the role of fluid in earthquake source processes, a setup capable of injecting pressurized water on the fault plane of the specimen was developed. We called this setup “DOLPHINS” (Dynamic Optimized Laboratory Pressurized Hydro-Injection Nucleation System). A highly-controllable design (shown in Figure 1.1) allows the selection of a wide range of pressure-time histories to be delivered to the frictional interface. Controllable quantities span from peak pressure, pressure rise time, and pressure plateau to fluid flow-rate. This flexibility enables the exploration of a number of nucleation conditions, leading to disparate rupture regimes ranging from slow-slip to earthquakes. To understand how this setup works, the main components will be described in the next sections. For the sake of clarity, these components are presented in the same order as the fluid *encounters* them flowing from upstream the circuit to downstream.

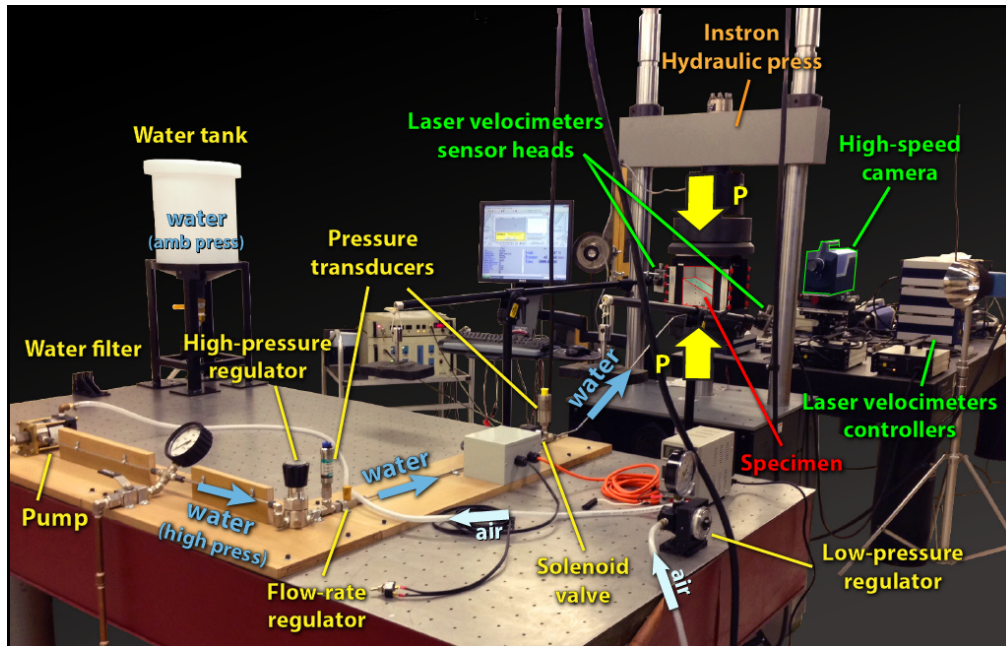


Figure 1.1: Newly-developed laboratory earthquake setup featuring a fluid-injection circuit capable of delivering pressurized fluid to the specimen's fault and trigger laboratory-scale earthquakes. The sample contains an interface that mimics a crustal fault pre-stressed in compression and shear. This setup can host both thin (2D) and thick (3D) specimen configuration and possesses an enhanced capability to control rate of injection and fluid pressure. The diagnostics consists of an ultra high-speed camera, laser velocimeters, and strain gages (not shown in the picture).

Haskel Pump

The principle of increasing pressure in a fluid must respect the first law of thermodynamics (i.e. energy conservation), which was stated in 1850 by Rudolf Clausius.

In a thermodynamic process involving a closed system, the increment in the internal energy is equal to the difference between the heat accumulated by the system and the work done by it.

More generally, an increase of the sum of internal energy U , kinetic energy K , and potential energy P is balanced by the heat and work added to the system

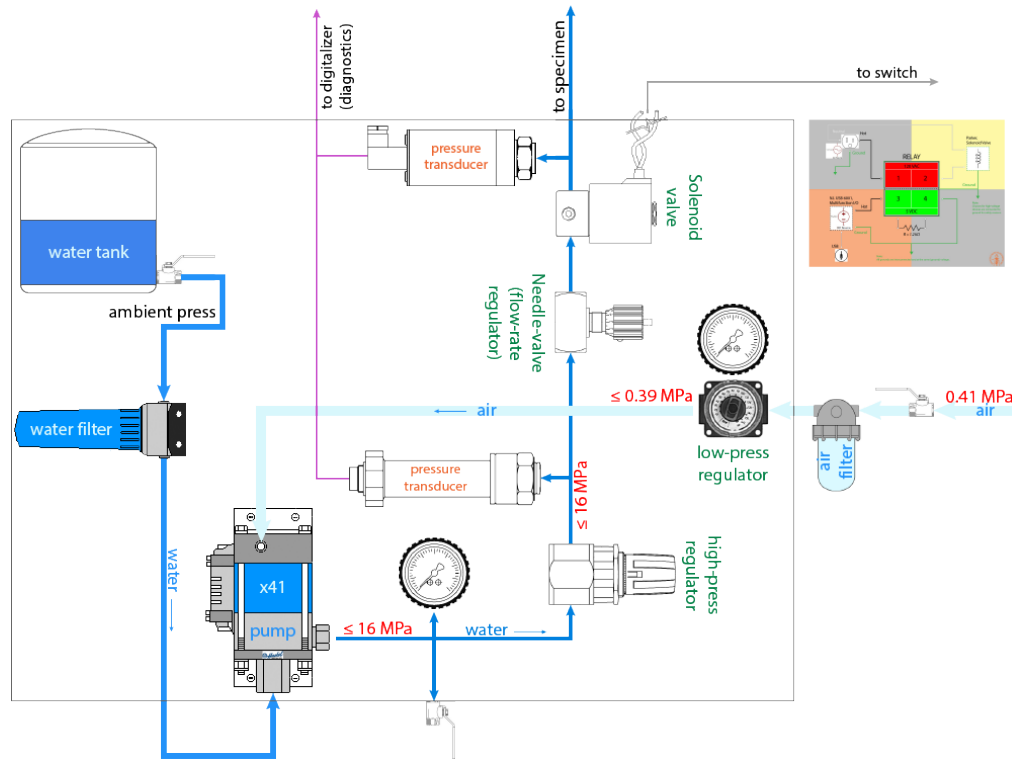
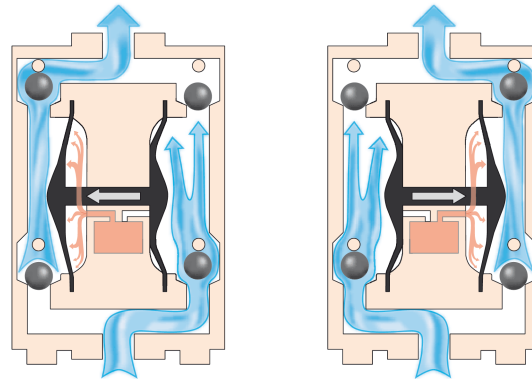


Figure 1.2: Schematic of the fluid-injection setup. The components have been arranged following their natural position on the optical table in Figure 1.1. The light blue arrows indicate the air flow, the darker blue arrows indicate the water flow, and the purple arrow indicates the electrical signal produced by the pressure transducers. The key components in this Figure will be presented in the following sections where the setup is introduced.

(in this case, fluid), $\Delta(U + K + P) = Q - W$, where Q and W are the heat and work exchanged with the system, respectively. Furthermore, the work can be decomposed into two components: the external work acting on the fluid, and the work changing the state of the fluid, i.e. $W = d(p/\rho) + W_{\text{ext}}$. In an adiabatic process, the heat exchange is null, i.e. $Q = 0$; for an incompressible fluid the internal energy is a function of the temperature only, and for small temperature changes (nearly isothermic) we can neglect its change. Following these assumptions, the increase in the sum of kinetic and potential energy is due to the work externally provided plus the amount of work spent modifying the state of the fluid, i.e. $W_{\text{ext}}/m = \Delta(p/\rho + u^2/2 + g z)$, where p is the fluid

pressure, ρ its density, u its velocity, g the acceleration of gravity, and z the height from a reference plane. In the simple case in which the velocity is null and so is the difference in heights from the input to the output of the system, the balance becomes $\dot{W}_{\text{ext}}/\dot{m} = 1/\rho \Delta p$, where an incompressible fluid was considered, i.e. $\Delta\rho = 0$, and the time derivative was taken on both the nominator and the denominator on the left-hand-side in order to express the equilibrium in terms of power, rather than work.

Following this principle, the external work (or external power) is provided by an MS-36 Haskel M-Pump (fig. 1.1 on the left and fig. 1.3), which intakes water at slightly higher-than-ambient pressure flowing-in from a higher-located reservoir ($p_{\text{amb}} + \rho g \Delta z$) and outputs it highly pressurized at the outlet. Figure 1.3 illustrates the pressurizing mechanism where a ‘driving fluid’ (in this case, air), in brown, actuates the diaphragm/piston which pressurizes the ‘driven fluid’ (in this case, water), in blue. This pump characterized by a maximum nominal water-to-air pressure ratio of 41 at the null flow rate by delivering a power of 1/3 hp and for this reason often times this typology of pumps is referred to as pressure multiplier. For instance, if the driving fluid (air) – sometimes called ‘working fluid’ – is at 0.39 MPa (55 psi), the driven fluid (water) at the outlet will be at 16 MPa. The pump performances are reported in fig. 1.4, where different air pressures correspond to the different colored lines, each of them representing the locus of points coupling a pressure and a volumetric flow rate the pump can output. For instance, given an input air pressure of 0.69 MPa (100 psi), a 20.7 MPa (3000 psi) pressure to the output will correspond to a volumetric flow rate of $1.17 \times 10^{-5} \text{ m}^{-3}/\text{s}$ (43 cubic inches per minute).



(a) Diaphragm fully de-
flected to the left

(b) Diaphragm fully de-
flected to the right



(c) MS-36 Haskel M-Pump

Figure 1.3: Representation of an intermittent hydraulic pump with air-driven elastic diaphragm (https://en.wikipedia.org/wiki/Diaphragm_pump). (a) The air, in brown, actuates the diaphragm, in black, and pressurizes the water on the left hand side, in blue. The water inlet at the bottom is separated from the the outlet at the top by four ball-valves, dark-gray spheres, which are synchronized with diaphragm's lateral motion in order to guarantee the correct sealing. (b) As the cycle continues, the air deflects the diaphragm toward the right where the water is pressurized and release, while simultaneously the left hand side is replenished with ambient pressure water. (c) A similar principle is adopted by the MS-36 Haskel M-Pump, which rather than a deformable diaphragm contains a rigid piston capable of significantly higher pressures (<http://www.haskel.com>).

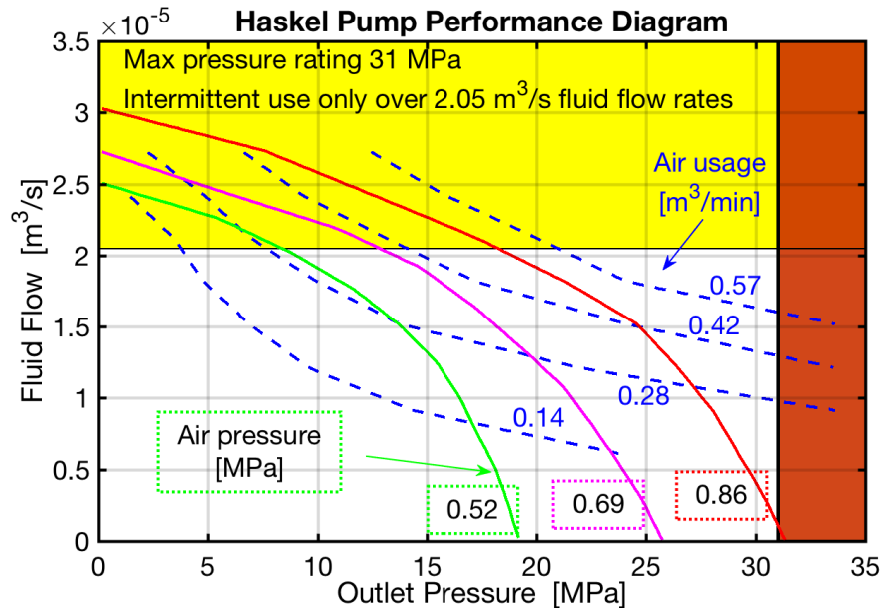


Figure 1.4: Diagram of the MS-36 Haskel M-Pump performance. The colored lines are loci of the combination of pressure and volumetric flow rate the pump will be able to deliver given a specific pressure by the working fluid, i.e., the green corresponds to 0.52 MPa (75 psi), the pink to 0.69 MPa (100 psi) and the red to 0.86 MPa (125 psi). The blue dash lines are level curves of the required air volumetric flow rate. This Figure was converted to IS units from the original vendor chart.

Driving Fluid (Air)

In GALCIT, the basement and sub-basement laboratories of the Firestone and Guggenheim buildings are equipped with externally pressurized air at about 0.41 MPa (60 psi), which can be used for hydraulic applications and, in particular, as a working fluid to drive a pneumatic pump. As shown in Figures 1.1 and 1.2, the air is filtered through an air filter removing all particles of size larger than 5 μm and allowing a airflow of $2.97 \times 10^{-2} \text{ m}^3/\text{s}$ at 0.69 MPa (100 psi). Its pressure is then modulated by a precision compressed-air pressure regulator, which allows continuous pressure regulation from the input value, all the way to zero. The nominal accuracy is of $\pm 3.45 \times 10^{-3} \text{ MPa}$ ($\pm 0.5 \text{ psi}$), yet practical experience reset that value to about $\pm 0.014 \text{ MPa}$ ($\pm 2 \text{ psi}$). At 0.69 MPa the maximum airflow is $5.52 \times 10^{-2} \text{ m}^3/\text{s}$. Due to internal losses, the maximum

pressure downstream the pressure regulator is 0.39 MPa (56 psi).

An analog pressure gauge with an error of $\pm 6.89 \times 10^{-3}$ MPa ($\pm 2\%$ midscale error) is connected to the regulator for precise pressure readings. The regulated air is then delivered to the Haskel pump where it can exchange work to compress the water (the energy/pressure balance has been described in section 1). Due to the low pressure of the air, clear and flexible PVC tubes can be adopted in this portion of the circuit.

It is important to notice that any variation in the air pressure deriving from the compressed-air pressure regulator will be delivered to the water multiplied by the pump water-to-air pressure ratio. Hence, given an accuracy of ± 0.014 MPa (± 2 psi) for the air pressure, the accuracy on the water pressure will be up to 41 times worse: ± 0.57 MPa (± 83 psi). For this reason, fine adjustments of the water pressure are better off performed on the driven fluid downstream the pump *after* it is pressurized, rather than upstream the pump on the driving fluid.

Driven Fluid (Water)

The supply of ambient-pressure water to the pump is guaranteed by the higher-than-the-pump placement of the water reservoir so that the liquid's flow is facilitated by the gravity. The fluid is then pressurized according to the input air pressure and flow rate setting, and on the required water flow rate at the output of the pump, according to the performance chart 1.4. Due to the high pressure of the fluid downstream the pump, 316 stainless steel tubes with an inner diameter of 3.18 mm (1/8") and an outer diameter of 6.35 mm (1/4") have been adopted. A ball valve allows rapid release of the high pressure by discharging water outside the circuit. An analog pressure gauge with an accuracy of ± 0.21 MPa (30 psi) guarantees high-pressure readings in correspondence to the valve as a safety measure. It is worth noticing that, if the pump is powered by pressurized air,

upon the opening of the ball valve, the pump will activate itself in the frenetic attempt to pressurize the open circuit. An intermittent regime for high flow rates will arise as predicted by the yellow-shaded area in the performance chart 1.4.

Figure 1.5 illustrates the next component in line, the high-pressure regulator, which permits precise pressure adjustments over a wide range of output pressures: 0 – 17.2 MPa (0 – 2500 psi). This precisely calibrated component allows not only the selection of the final level of the pressure to be delivered to the specimen's interface, but also the manual modulation of the pressure ramp-up profile. This feature is key in the investigation of several nucleation regimes as slow rump-ups will produce intrinsically different behaviors than fast ones. These details will be largely investigated in later chapters.

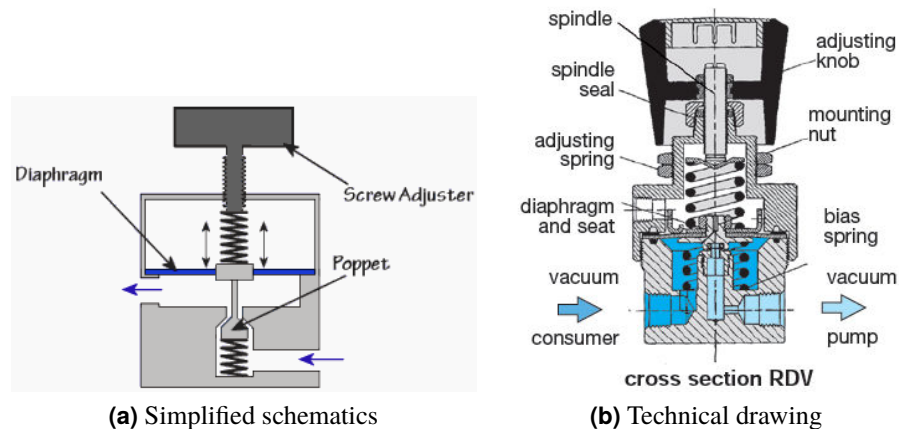


Figure 1.5: The pressure is regulated via a hand-screw adjuster by compressing a spring, which is connected to a valve (or poppet), inserts (a) and (b). As this gets gradually opened, a certain amount of pressurized fluid flows through from upstream, starting to increase the pressure downstream the valve. While the pressure builds up, a diaphragm is compressed against the spring in the opposite direction of the screw adjuster, eventually closing back the valve. At this time, an equilibrium is reached between the screw adjuster exerting a force downwards on the spring and the fluid pressure downstream the valve, exerting an opposite force onto the diaphragm connected to the spring. If a higher pressure is desired downstream, the spring needs to be further compressed via the screw adjuster in order to create a higher force downwards to be eventually balanced by the fluid pressure acting upwards on the diaphragm. Evidently, the downstream pressure cannot physically exceed the one upstream.

An easy-set precision flow-adjustment valve allows flow manual-control. It is characterized by a flow coefficient C_v of 0.53, relating the pressure drop across it with the flow rate at 15 °C (59 °F) according to the relationship $q = C_v \sqrt{\Delta p / SG}$, where q is the volumetric flow rate (in US gallons per minute), p the pressure, and $SG = \rho_{\text{substance}} / \rho_{\text{H}_2\text{O}}$ the specific gravity, which for water is equal to the unity.

An ESI digital pressure transducer is USB-connected to a computer for precise pressure reading downstream both the pressure regulator and flow-adjustment valve. The accuracy is of ± 0.2 MPa (± 29 psi), in similarity to the analog pressure gauge upstream the pressure regulator, and the sampling rate can reach up to 5 S/s, perfectly suitable for controlling the pressure rate during slow manual ramp-ups.

Faster ramp-up regimes can be captured by a Honeywell TJE pressure transducer with a bandwidth (BW) of 3 kHz, able to resolve rising times of 0.116 ms (using $t_{\text{rise}} = 0.35 / BW$). The connection to an analog-to-digital (A/D) converter (a Tektronix Digital Oscilloscope, model # DPO3034) in combination with the output signals from other devices allows a precise synchronization among them.

A compact, electrically-actuated solenoid valve is placed between the two pressure transducers (after the *slower-acquisition* transducer, before the *faster-acquisition* transducer). The valve is characterized by a flow coefficient (C_v) of 0.021 – indicating increasingly larger pressure-drops as the volumetric flow rate increases (as previously shown) – and can operate between 0 and 20.7 MPa (0 – 3000 psi). When unpowered, it's in shut position (normally closed); upon powering (10 W), it fully opens in few tens of milliseconds (circa 5 – 20 ms, see fig. 1.6). After a detailed conversation with the manufacturer, an alternating current (AC) model has been selected over a direct current (DC) one for the

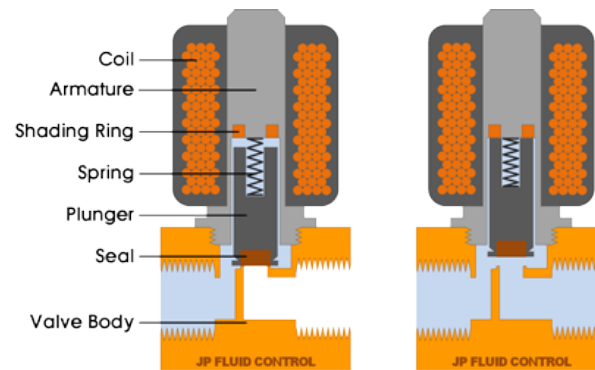


Figure 1.6: When unpowered, the solenoid valve is in close position (left). The sealing is guaranteed by a spring and the fluid pressure upstream both acting in closing the plunger. Upon the delivery of electricity to the coil, a magnetic field is generated which interacts with that of the plunger (a magnetic element) driving it upwards and opening the seal. The fluid can now flow downstream (right) as long as the power to the coil is maintained. The characteristic time of opening for this valve is in the order of few tens of milliseconds.

sake of minimizing the opening time (although precise data is unavailable), requiring a signal of 120 V/60 Hz for successful opening. The presence of a solenoid valve in this location enables the hydraulic exclusion of the specimen downstream the valve from the pressurized section of the circuit upstream it (see figs 1.1 and 1.2). If the valve is open, the pressure information from the high-pressure regulator will be directly transmitted to the specimen (through the reverberation of multiple shocks, expansion waves, and contact discontinuities in the fluid). However, if the valve is closed, the circuit can be pressurized to a desired value without the specimen *feeling* it; under these conditions, upon the valve opening, a rapid pressure ramp-up can be sent to the specimen. These two cases illustrate the enhanced flexibility the introduction of the solenoid valve adds to the fluid-injection circuit: the most-rapid-possible manual opening of the screw adjuster in the high-pressure regulator would take several seconds; the use of the valve reduces this time to few tens of milliseconds. The importance of having a second pressure transducer capable of data fast-acquisition stands in its ability of capturing rapidly-changing signals generated from the opening

of the solenoid valve. It is also worth noticing that regardless of the pressure ramp-up protocol adopted in the specific experiment, a pressure transducer placed downstream the solenoid valve always measures the pressure conditions as they are *felt* by the specimen (with some small delay due to waves propagation in water); while a pressure transducer placed upstream the solenoid valve enables the selection of a desire pressure level when the valve is closed, prior to its opening and delivery of such pressure to the specimen.

In order to **safely** operate at these level of voltage, specific measures must be accounted for. A general knowledge on the pathophysiology associated with the exposure of the human body to the electricity is needed. Details about this can be found in Appendix [1.A](#), while Appendix [1.B](#) illustrates the design of a simple electrical circuit to run the valve.

1.A An informative curiosity on patophysiology of alternating current

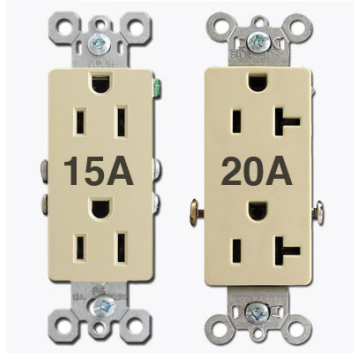


Figure 1.7: Out of a wall outlet in the US. The I-shaped slot (left) can carry up to 15 A and is usually employed for domestic appliances, while the T-shaped slot (right) can carry up to 20 A, usually for commercial or industrial use.

A number of studies have been carried out in the last century. Ferris et al., 1936 were the first ones to point out that current, rather than voltage, is the correct criterion for shock-intensity. They investigated the effect of electric shocks on the heart of mammals of size somewhat similar to humans and finding that “electric shock may derange heart action causing ventricular fibrillation without damage to heart tissue, but resulting in death within a few minutes” and related the fatal levels of current to the body and heart weight in animals.

Ventricular fibrillation is the uneven pumping of the heart due to the uncoordinated, asynchronous contraction of the ventricular muscle fibers of the heart that

leads quickly to death from lack of oxygen to the brain. Ventricular fibrillation is terminated by the use of a defibrillator, which provides a pulse shock to the chest to restore the heart rhythm. Cardiopulmonary resuscitation (CPR) is used as a temporary care measure to provide the circulation of some oxygenated blood to the brain until a defibrillator can be used (Electrocution, 1998).

Dalziel (Dalziel, 1946) adopted the previous methodology and tried to extrapolate data from lower unarmful currents applied on 164 test individuals

and higher harmful ones applied on animals in order to predict more broadly the threshold for human heart ventricular fibrillation. He introduced the relationship $I = K/t^{1/2}$ mA, where K is the current of heart fibrillation in mA during a 3 s exposure to that current found to be $K = 155$ mA (extrapolated from testing animals of similar weight to humans: sheep, dogs, et cetera). Kouwenhoven (Kouwenhoven, 1949) analyses the resistance of the human body, dividing it in two categories: the skin (distinguishing between dry and wet) and the internal portion and sets a safety voltage threshold for humans to 24 V at 60 Hz (the lowest voltage fatality occurred at 48 V at 60 Hz); he then describes the post-shock effects and introduces a resuscitation practice – called *defibrillation* – during ventricular fibrillation by passing a 1 to 2 A current at 60 Hz through the heart in order to *bring the muscles of the heart to rest and hold the organ in diastole. Then when the circuit is broken the heart usually will resume its normal operating rhythm.* Geddes and Baker (Geddes and Baker, 1971) introduce the relation of ventricular fibrillation and frequency. In particular they show that the dog heart starts fibrillating for currents 22 to 28 times higher at 3 kHz rather than 60 Hz, which directly translates into the concept that the direct current is more dangerous. Dalziel (Dalziel, 1972) reports more accurate data on humans with attention to muscular contraction during current passage finding 18 mA as the limit value to discontinue breathing due to chest muscular contraction. However, normal breathing (and muscular function) was restored upon current removal. A safety threshold for unlikeliness of heart fibrillation at 60 Hz of $I = 116/t^{1/2}$ mA was determined (although, this does not guarantee safety from other types of injuries like workers falling from ladders, et cetera). Currents sensibly in excess of those causing ventricular fibrillation may cause cardiac arrest, respiratory inhibition, irreversible damage to the nervous system, serious burns, and unconsciousness. Hammam and Baishiki (Hammam and Baishiki, 1983) review many published findings regarding the human body's impedance

depending on the electric magnitude, frequency, path and duration. The more recent analysis on electric-shock accidents that befell workers by the National Institute for Occupational Safety and Health (Electrocution, 1998) reports that between 1980 and 1992 electrocutions were the 5th leading cause of death among workers, with 411 deaths per year accounting to 7% of the total. The pathophysiology is summarized in table 1.1.

Table 1.1: Estimated effects of alternating currents at 60 Hz (Electrocution, 1998).

AC level	Pathophysiological effects
1 mA	Barely perceptible
16 mA	Maximum current an average man can grasp and “let go”
20 mA	Paralysis of respiratory muscles
100 mA	Ventricular fibrillation threshold
2 A	Cardiac standstill and internal organ damage
15 – 20 A	Common fuse or breaker opens circuit (see fig. 1.7)

Fish and Geddes (Fish and Geddes, 2009) review more recent papers with higher detail on the physiology, the dangers from electrical exposure and best practices to prevent it. For instance they summarize the reasons why immersion in water can be fatal even at low voltages:

- Immersion wets the skin very effectively and greatly lowers skin resistance per unit area.
- Contact area is a large percentage of the entire body surface area.
- Electric current may also enter the body through mucous membranes, such as the mouth and throat.
- The human body is very sensitive to electricity. Very small amounts of current can cause loss of ability to swim, respiratory arrest, and cardiac arrest.

Table 1.2 concentrate on the fatal level of current and voltages associated with the human body.

Table 1.2: Estimated effects of alternating currents at 60 Hz (Fish and Geddes, 2009).

Current [mA]	Voltage [V]	Mechanism
10	3	Loss of muscle control of the extremities: as little as 10 mA for the most sensitive female
16	4.8	Loss of muscle control of the extremities: 16 mA for an average man
20	6	Tetanic contraction (effectively paralysis) of the muscles of respiration
100	30	Electrical stimulation of the heart causing ventricular fibrillation

Wang and coworkers (Wang, Wang, and Peng, 2013) summarize the pathophysiological behavior in an indicative plot (fig. 1.8), with the AC current levels explained in the following table 1.3.

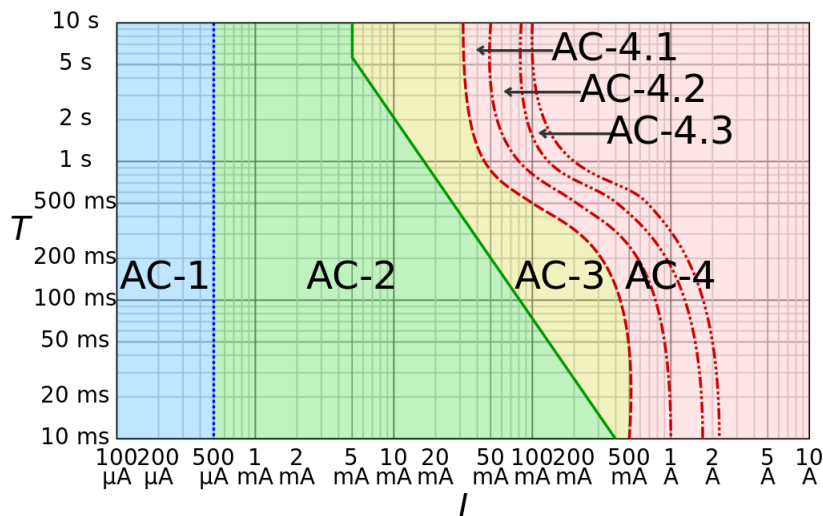


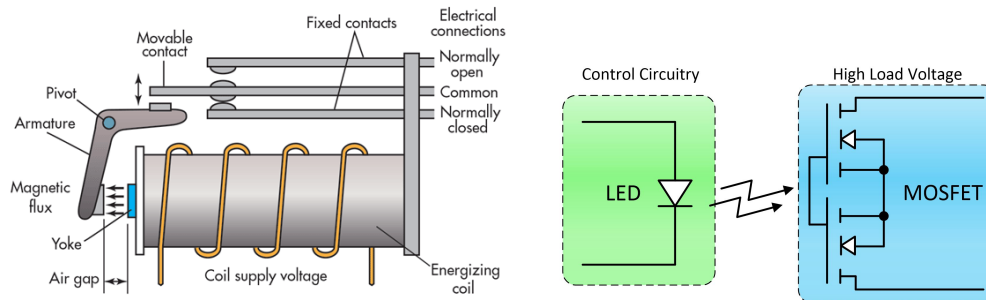
Figure 1.8: Log-log graph of the effect of alternating current (AC) I flowing from left hand to feet – through the heart – as a function of time-duration T (Wang, Wang, and Peng, 2013).

Table 1.3: Pathophysiology of alternating current flowing from left hand to feet as illustrated in Figure 1.8 (Wang, Wang, and Peng, 2013).

Current level	Pathophysiological effects
AC-1	Impercetible
AC-2	Perceptible, but no muscle reaction
AC-3	Muscle contraction with reversible effects
AC-4	Possible irreversible effects
AC-4.1	Up to 5% probability of ventricular fibrillation
AC-4.2	5 – 50% probability of fibrillation
AC-4.3	Over 50% probability of fibrillation

1.B Relay-based electric circuit to operate the solenoid valve

TYPICAL SIMPLIFIED ELECTROMECHANICAL RELAY SCHEMATIC



(a) Schematic of an electromechanical relay. When the coil is unpowered, the armature is away from the yoke and the movable contact keeps the switch open (see gap from the top fixed contact). When energized, the coil produces an electromagnetic field that attracts the armature and closes the air gap. The armature then pushes the movable contact upwards and closes the connection with the top fixed contact. The so-closed switch allows high-voltage electricity to flow.

(b) Modern solid-state relays internally use the transistors. The conceptual principle is to use a Light Emission Diode (LED) that, when powered, sends emitted photons of a certain wavelength to the receiver, a Metal-Oxide-Semiconductor Field-Effect Transistor (MOSFET). This last one will act as a switch and close the high-voltage circuit when “illuminated” by the photons from the LED.

Figure 1.9: The transistor technology has several advantages that made it successful in the relay industry (as much as in many other ones): it consumes less current in the “on” state than the electromechanical counterpart, it doesn’t have wearable-by-usage parts such as the contacts or the moving parts, and it is much faster – electromechanical relays typically require 50 ms to switch, while transistors can be as fast as picoseconds ($1 \text{ ps} = 10^{-12} \text{ s}$).

When unpowered, the solenoid valve is in close position, often referred to as *normally close*. The hydraulic sealing is guaranteed by the presence of a spring and the pressure of the fluid upstream pushing the plunger shut (as shown in fig. 1.6). When a 120 VAC / 60 Hz current is delivered to the valve, the plunger (a magnetic element) opens, driven by the magnetic force the coil induces on it. As long as the voltage is maintained, the valve remains open. In order to avoid direct exposure to 120 VAC / 60 Hz current, a relay-based circuit has been designed. A relay is an electrically operated switch connected to both the valve high-voltage circuit (upper portion in fig. 1.10) and a low-voltage circuit (lower portion in fig. 1.10) manually controlled by the operator. When the low voltage

circuit is closed (bottom right square in Figure 1.10), the relay closes the high voltage one as well and the valve opens (upper right square in Figure 1.10). The advantage of such a configuration is that the operator is never in contact with the high voltage circuit as she/he rather operates a switch on the lower voltage side. Figure 1.9 (a) shows the operating principle of an electromagnetic relays. However, modern solid-state relays (fig. 1.9 (b)) use a different principle with the advantage of a much faster response (in the picoseconds time scale), lower electrical consumption and higher robustness. A modern solid-state relay has been adopted as the center of this circuit (fig. 1.10 center). For safety reasons, the relay has been enclosed in a metal chassis (visible in Figure 1.1 just before the solenoid valve) and connected to ground.

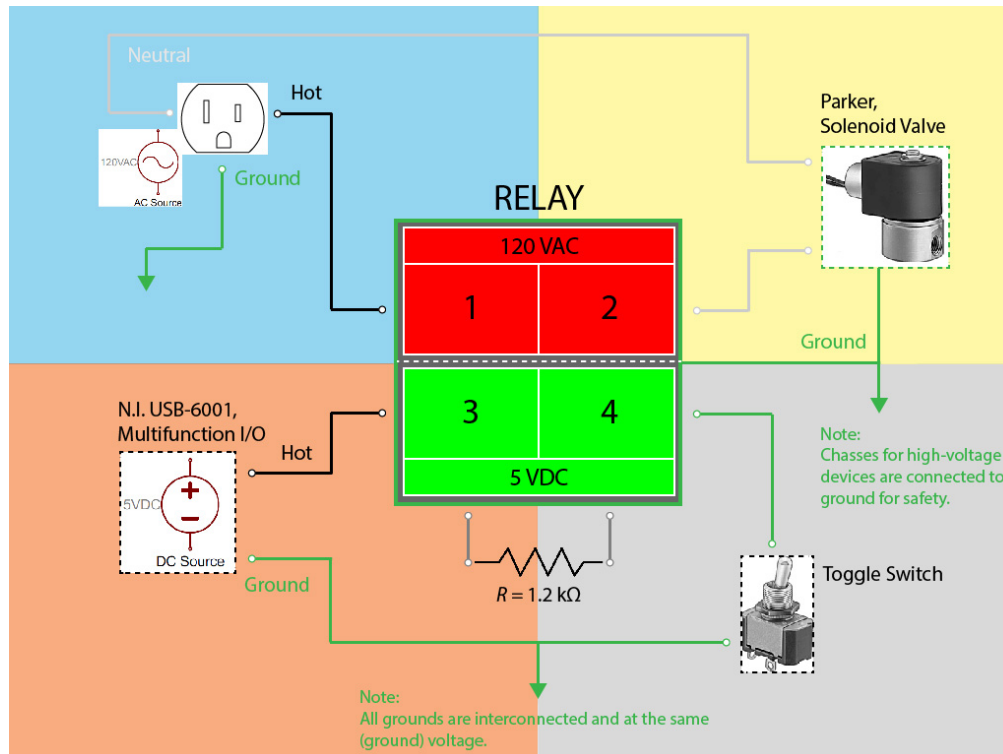


Figure 1.10: Schematic of the electric circuit to power the solenoid valve (upper-right portion). At the center of the Figure is represented the relay: the green portion represents the safe-for-humans 5 V direct current (DC) powered by a DC generator (lower-left portion); the red side represents the dangerous-for-humans 120 V alternating current (AC) powered by the wall outlet (upper-left portion). When the toggle switch (lower-right portion) is closed, the 5 VDC current is driven to the relay, which will close the 120 VAC circuit and power the valve to switch open.

Part I

Pressure and shear shock fronts

CHAPTER 2

Pressure shock fronts formed by ultra-fast shear cracks in viscoelastic materials

“If the result of an experiment is in agreement with the expectations, a measurement has been performed. If, on the other hand, the result is *not* in agreement with the expectations, a discovery has been made.”

–E. Fermi

2.1 Introduction

Shock fronts are sharp discontinuities that arise whenever a perturbing feature, such as a crack traveling through a medium, exceeds the characteristic speed of the waves by which the energy is transferred in the medium. In such a situation, the waves coalesce into a sharp shock front, as observed in atmospheric

supersonic flight, hypersonic re-entry from space, meteoroid transit through the atmosphere, and motion of planets with respect to the solar wind (Anderson Jr, 2010; Decker et al., 2005; Dougherty et al., 2005; Fisk, 2005; Gurnett and Kurth, 2005; Lallement et al., 2005; Liepmann and Roshko, 1957).

In fracture mechanics and geophysics, shear shock fronts have been observed to arise by the coalescence of shear waves emitted by tips of spontaneously propagating shear ruptures exceeding the shear wave speed of the surrounding material (Mello, Bhat, and Rosakis, 2016; Mello et al., 2010; Rosakis, Xia, et al., 2007; Xia, Rosakis, and Kanamori, 2004). These ruptures are commonly referred to as “supershear” or “intersonic”. The speed of the spontaneously propagating cracks is a fundamental problem that has captivated the interest of the scientific community for several decades due to its implications across multiple scientific and engineering disciplines (Abraham and Gao, 2000; Abraham, Walkup, et al., 2002; Buehler, Abraham, and Gao, 2003; Fineberg and Bouchbinder, 2015; Freund, 1998; Marder, 2006; Needleman, 1999; Rice, 2001; Rosakis, Xia, et al., 2007; Rosakis, 2002; Xia, Rosakis, and Kanamori, 2004). In particular, the study of shear cracks propagating along frictional interfaces and the associated shock fronts is relevant to earthquake dynamics (Bouchon and Vallée, 2003; Dunham, Favreau, and Carlson, 2003; Ellsworth et al., 2004; Mello et al., 2014). The formation of the shock fronts is an important problem in its own right, due to implications of this phenomenon for strong ground motion much farther from earthquake-producing faults than currently accounted for in seismic hazard (Bouchon and Vallée, 2003; Dunham, Favreau, and Carlson, 2003; Ellsworth et al., 2004; Mello, Bhat, and Rosakis, 2016; Mello et al., 2010; Rosakis, Xia, et al., 2007; Xia, Rosakis, and Kanamori, 2004).

Spontaneously propagating cracks are driven by elastodynamic waves, where the energy released by the crack motion is transferred through the medium to

the crack tip region with the (higher) pressure wave speed and (lower) shear wave speed. It is intuitively evident that a crack cannot exceed the fastest way to transfer energy: the pressure wave speed (Freund, 1998; Needleman, 1999; Rice, 2001; Rosakis, Xia, et al., 2007; Rosakis, 2002). Hence the formation of a shock front may appear impossible for the pressure waves.

2.2 Experimental Setup

In this study, we provide the first experimental evidence of spontaneously propagating shear ruptures forming a pressure shock front and explain the formation by the strain-rate-dependent – and hence spatially variable – stiffening of the material in the vicinity of the rupture tip. The presence of the pressure shock fronts enables us to refer to our cracks as supersonic. The presented dynamic shear ruptures are produced in an experimental set-up developed to mimic earthquakes in the laboratory (Mello, Bhat, and Rosakis, 2016; Rosakis, Xia, et al., 2007; Xia, Rosakis, and Kanamori, 2004). (Fig. 2.1a; see section 2.4). The set-up features a quadrilateral specimen made of a polymeric material - either Poly(Methyl Meth-Acrylate) (PMMA) or Homalite-100 – with an interface inclined at an angle α (Fig. 2.1a). The uniform external load P vertically applied to the specimen results in a normal and a shear static pre-stress acting along the interface. The tests exhibited in Figs. 2.1 and 2.2 have been conducted under the following experimental conditions: $P = 21$ MPa and $\alpha = 30^\circ$ for PMMA and $P = 25$ MPa and $\alpha = 29^\circ$ for Homalite-100. The ruptures are triggered by the local brief pressure release due to the sudden disintegration of a Ni-Cr wire filament placed across the specimen's interface. This laboratory earthquake set-up has been successfully employed in the past to study several key rupture phenomena including supershear transition to intersonic speeds (Xia, Rosakis, and Kanamori, 2004), rupture directionality and limiting speeds due to

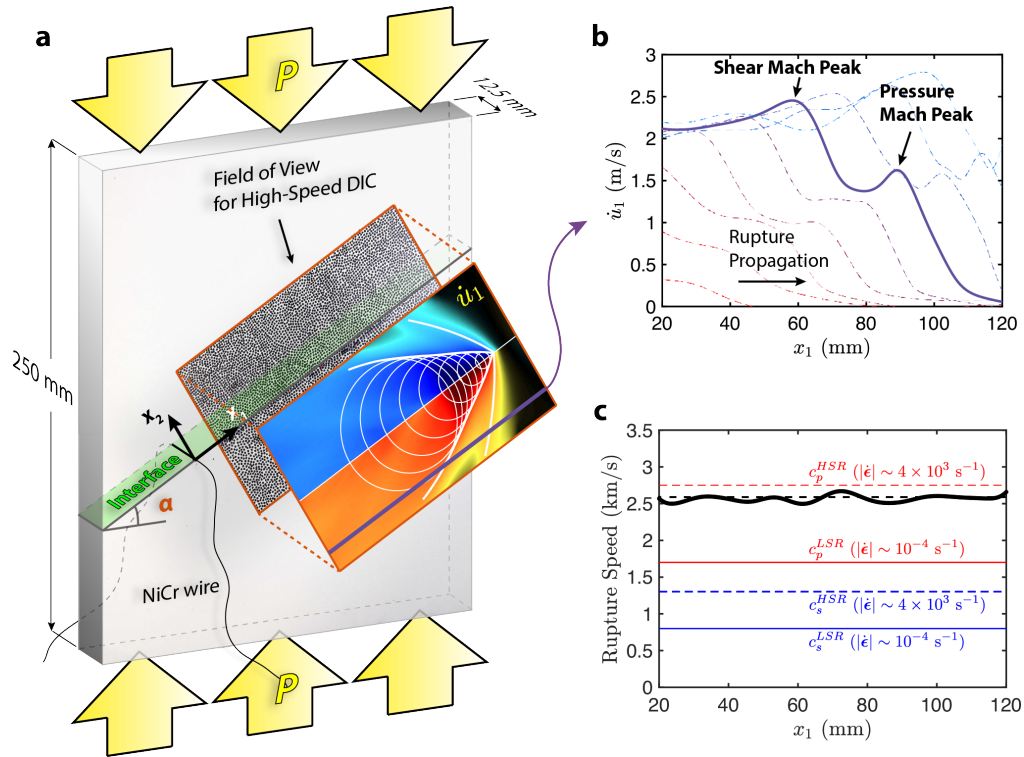


Figure 2.1: Laboratory setup and the captured supersonic shear ruptures. (a) The dynamic rupture is produced on a sample interface (green-shaded area) loaded in compression and shear by a compressive vertical load (yellow arrows). The rupture is triggered by the sudden disintegration of a Ni-Cr wire filament and subsequently propagates spontaneously over the interface. Its dynamics is captured using a speckle pattern applied over a portion of the specimen’s surface, ultra-high-speed photography, and DIC algorithms. The inset exhibits the distribution of interface-parallel particle velocity, \dot{u}_1 , 58 μs after nucleation. The white lines highlight the peaks associated to the pressure and shear shock fronts, and the white circles are representative of how the shear shock front is generated by the coalescence of the shear wavelets. An analogous construction – not shown here – applies to the pressure cone. (b) The profile of the particle velocity, \dot{u}_1 , along the violet line (at a distance $x_2 = -27.5$ mm from the interface), plotted at time intervals of 5 μs , exhibits two recognizable peaks associated to the pressure and shear Mach fronts. (c) The rupture speed versus position along the interface, x_1 , is computed by tracking the rupture tip in the temporal sequence of velocity maps. The comparison with the pressure wave speed in the bulk material, where low strain rates are attained (Figs. 2.3 and 2.6), confirms the supersonic nature of the rupture, $V_r > c_p^{LSR}$ (see text). At the crack tip, where considerably higher strain rates develop (Fig. 2.3, lower inset), the rupture is locally intersonic, $c_s^{HSR} < V_r < c_p^{HSR}$.

bimaterial effects (Xia, Rosakis, Kanamori, and Rice, 2005), off-fault damage generation (Rosakis, 2002), pulse-like to crack like transitions (Lu, Lapusta, and Rosakis, 2007), opening of thrust faults (Gabuchian et al., 2017), and friction evolution (Rubino, Rosakis, and Lapusta, 2017).

2.3 Results and Discussion

It is quite challenging to capture the highly dynamic evolution of these shear ruptures in the laboratory, since they take mere tens of microseconds to span the experimental samples. The full-field visualization of supersonic cracks employed here is enabled by our recently developed dynamic imaging technique (*ibid.*) based on a combination of high-speed photography and digital image correlation (see section 2.4). A sequence of 128 high-speed digital images – with temporal sampling of up to 2-million frames per second – is converted into a temporal series of displacement fields by the digital image correlation (DIC) method, with algorithms tailored to treat displacement discontinuities along an interface (*ibid.*). The particle-velocity and strain fields are computed by temporal and spatial differentiation of the displacement fields, respectively. The strain-rate maps are obtained by time differentiation of the strain fields. In a set of repeated experiments, an array of four strain-gage stations have been placed along the interface to capture the rupture's arrival time as it swipes through them and confirm its supersonic nature (Fig. 2.4).

The full-field images of the particle-velocity, strain, and strain-rate fields during dynamic ruptures in our experiments exhibit two pairs of sharp fronts diverging from the rupture tip, associated with the formation of the pressure and shear shock fronts (Fig. 2.1a, inset; Figs. 2.2 and 2.5). The shear shock fronts, occurring when the rupture exceeds the shear wave speed, have been observed using photoelasticity (Gabuchian et al., 2017; Mello, Bhat, and Rosakis,

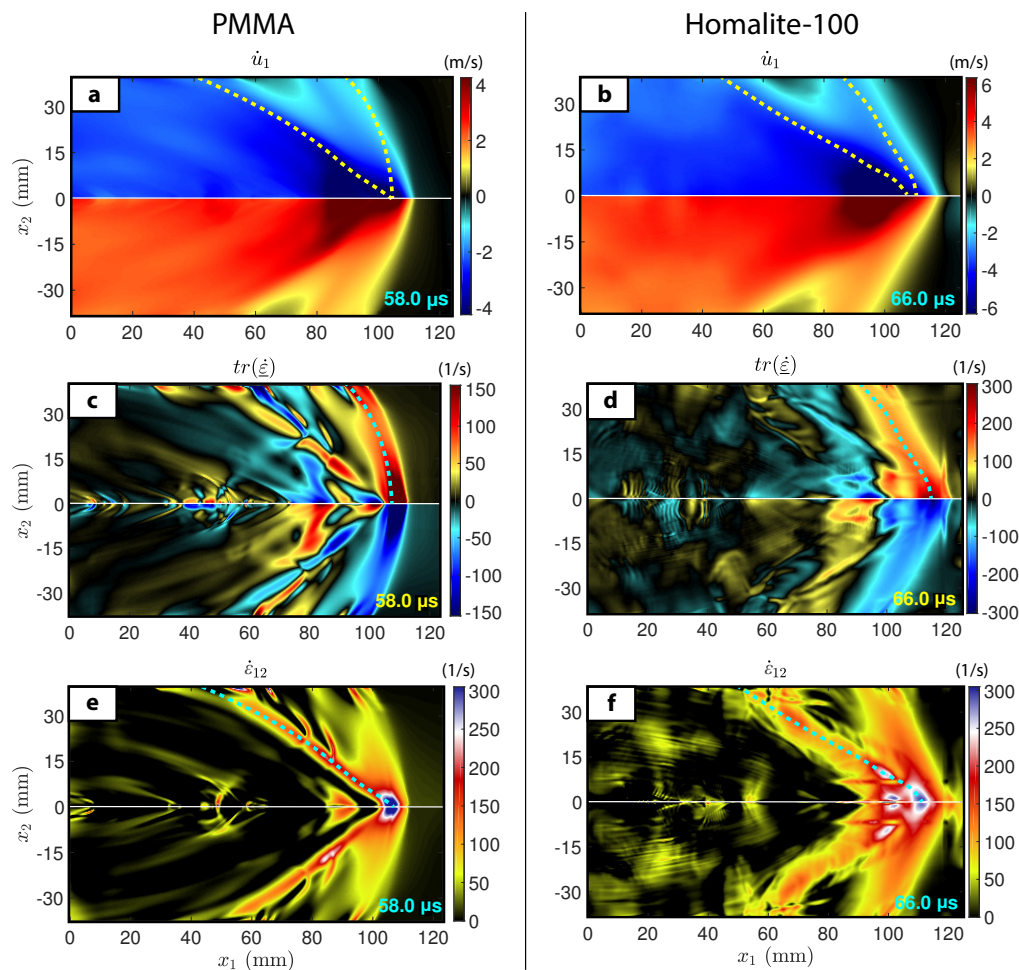


Figure 2.2: Full-field particle velocities and strain measures for supersonic ruptures. Both PMMA (left) and Homalite-100 (right) exhibit two pairs of shock fronts, the pressure and the shear one (colored dashed lines). The PMMA snapshots correspond to 58 μs after the triggering and the Homalite-100 ones to 66 μs . (a) and (b), Interface-parallel particle velocity, \dot{u}_1 . (c) and (d), Volumetric strain rate, $tr(\dot{\epsilon})$. (e) and (f), Shear strain rate, $\dot{\epsilon}_{12}$. The volumetric strain-rate field (c and d) enhances the presence of the pressure shock front, while “hides” that of the shear Mach cone. The shear strain-rate field (e and f) does the opposite, by showing a healthy shear shock front and a less developed pressure one. Therefore, the pressure and shear shock fronts, highlighted in colored dashed lines, are traced as the loci of maxima of the volumetric strain rate (c, d) and shear strain rate (e, f), respectively. The fronts thus determined are then reported in the velocity fields above (a, b).

2016; Mello et al., 2014; Rosakis, Xia, et al., 2007; Rosakis, 2002; Xia, Rosakis, and Kanamori, 2004), a technique sensitive to shear deformations. Our newly developed high-speed DIC technique reveals the additional formation of a pressure shock front. The pressure shock fronts are most visible in the distribution of the volumetric strain rate, $\text{tr}(\dot{\epsilon})$ (Fig. 2.2c and d), while the shear shock front are most noticeable in the distribution of the shear strain rate, $\dot{\epsilon}_{12}$ (Fig. 2.2e and f), consistent with the properties of the corresponding waves.

How can we confirm that these features are indeed pressure shock fronts, and not some other expression of a pressure wave field that would be present around any crack tip (Mello, Bhat, and Rosakis, 2016) Since the shock front is the envelope of coalescing waves, the defining feature of a shock front is the kinematic relationship that holds among the inclination angle β of the shock front, the wave speed (either c_s or c_p depending on the front), and rupture speed V_r (Anderson Jr, 2010; Liepmann and Roshko, 1957; Mello, Bhat, and Rosakis, 2016; Mello et al., 2010; Xia, Rosakis, and Kanamori, 2004):

$$\beta_{s,p} = \arcsin(c_{s,p} / V_r) \quad (2.1)$$

The inclination angle of the shock front is the angle that the front forms with the path of the propagating feature, in our case the rupture interface.

To verify this relation for the pressure shock fronts, we need to find the rupture speed, inclination angle, and wave speed of the material. We compute the rupture speed V_r from the temporal series of velocity maps by tracking the rupture tip location along the interface at each frame (Fig. 2.1a and section 2.4). This leads to the steady rupture speed of $V_r = 2.57$ km/s within the window of observation for the experiment with PMMA shown in Figs. 2.1, 2.2 (left column), 2.3 (top inset), and 2.4. The inclination angle varies along the pressure shock front (Fig. 2.2); for the steady rupture speed, the kinematic relation 2.1 would imply that the wave

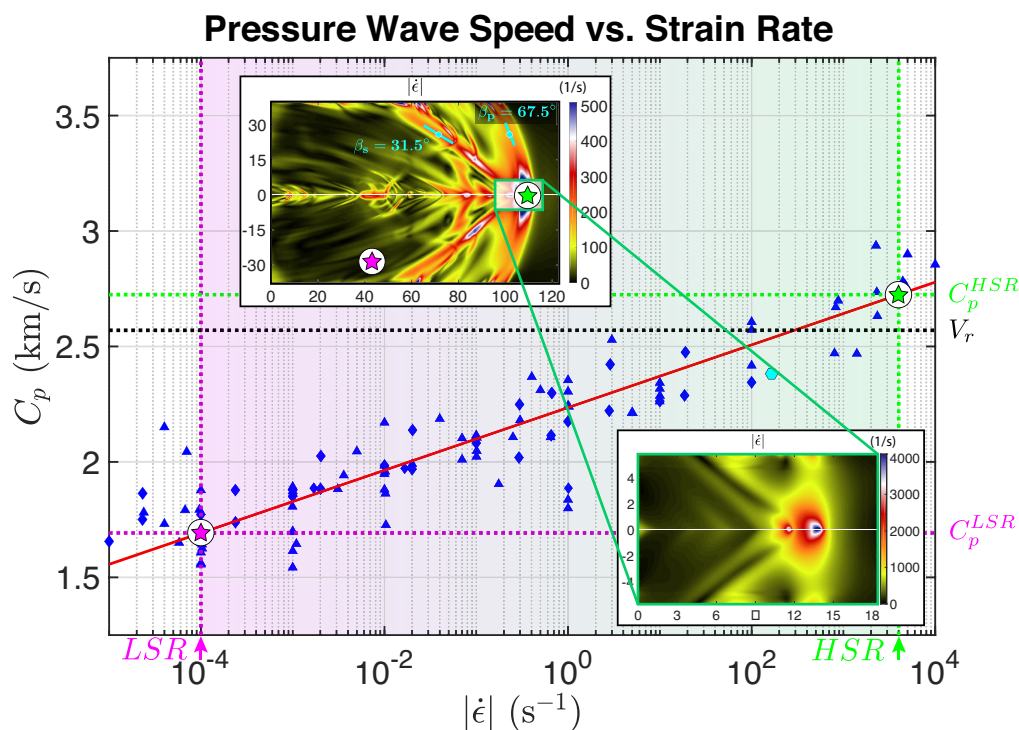


Figure 2.3: Strain-rate dependence of the pressure wave speed in PMMA. The values of the pressure wave speeds have been computed by converting the elastic moduli versus strain-rate data acquired from the literature (Fig. 2.6). Linear-elastic wave relations have been adopted, assuming a density $\rho = 1180 \text{ kg/m}^3$ (measured) and a constant Poisson's ratio $\nu = 0.35$ (Mulliken and Boyce, 2006; Richeton, Ahzi, Vecchio, Jiang, and Makradi, 2007). The blue triangles indicate compressive tests with the exception of the diamonds, which indicate tensile tests. The cyan hexagon represents the value of c_p measured from the inclination angle, as shown in the inset. The horizontal black dashed line represents the rupture speed $V_r = 2.57 \text{ km/s}$, computed by tracking the rupture tip in the temporal sequence of full-field images (Fig. 2.1, see section 2.4). The upper inset exhibits a snapshot of the equivalent strain-rate field, $|\dot{\epsilon}|$, at $58 \mu s$ after triggering. The strain-rate measurements obtained from the full-field images (insets) are reported on the c_p vs. $|\dot{\epsilon}|$ plot for two locations: at the crack tip (green star in upper inset), and behind the shock fronts ($x_1 = 42 \text{ mm}$, $x_2 = -29 \text{ mm}$) (purple star in the upper inset). The green and purple vertical dashed lines refer to the equivalent strain-rate levels for these near-field and far-field measurements, and the corresponding values of the pressure wave speeds are indicated by the horizontal green and purple dashed lines. The strain-rate level at the crack tip is obtained from a similar test performed on a sample at an angle $\alpha = 29^\circ$ (rather than 30°) under the same loading conditions, by focusing on a smaller field of view, which enables a higher strain-rate resolution (lower inset).

speeds are decreasing in the interface-normal direction. Such an observation is consistent with the viscoelastic response at spatially variable strain rates, with the higher strain rates closer to the crack tip leading to more viscoelastic stiffening and hence higher wave speeds. Indeed, several experimental studies in polymers, including Homalite (Mello, Bhat, and Rosakis, 2016; Mello et al., 2010; Rosakis, Samudrala, et al., 1998) and PMMA (Bayart, Svetlizky, and Fineberg, 2016; Ben-David, Cohen, and Fineberg, 2010; Fineberg and Bouchbinder, 2015; Rosakis, Samudrala, et al., 1998; Svetlizky, Bayart, et al., 2017; Svetlizky and Fineberg, 2014), have accounted for their viscoelastic nature by considering the specimens as still uniformly linear elastic but with uniformly altered (stiffer) values of elastic constants during their dynamic response. Some of those studies (Ben-David, Cohen, and Fineberg, 2010; Fineberg and Bouchbinder, 2015; Mello, Bhat, and Rosakis, 2016; Mello et al., 2010; Rosakis, Xia, et al., 2007; Rosakis, Samudrala, et al., 1998; Svetlizky, Bayart, et al., 2017) observed crack tip speeds similar to the ones reported in this work but did not recognize their significance since, in the “uniformly stiffer” interpretation, it only makes sense to compare the crack tip speeds to the uniformly higher wave speeds, and that comparison would suggest that the cracks are intersonic, a well-known phenomenon (Ben-David, Cohen, and Fineberg, 2010; Fineberg and Bouchbinder, 2015; Mello, Bhat, and Rosakis, 2016; Mello et al., 2010; Svetlizky, Bayart, et al., 2017). Our findings emphasize the qualitative importance of the viscoelastic effects in creating the spatially heterogeneous stiffening due to spatially inhomogeneous strain rates that has not yet been taken into account.

We find that the non-uniform stiffening due to viscoelastic effects, and hence spatially variable wave speeds, can indeed explain our experimental observations, including the inclination angles of the pressure shock front observed in our experiments. Here, by “wave speeds” we understand the group velocities, e.g., the speed with which the energy is conveyed along a wave (Lighthill, 2001).

We use the published data on how strain rates affect the Young's and shear moduli (Lee and Swallowe, 2006; Mulliken and Boyce, 2006; Richeton, Ahzi, Vecchio, Jiang, and Adharapurapu, 2006; Richeton, Ahzi, Vecchio, Jiang, and Makradi, 2007; Singh and Parameswaran, 2003; Wu, Ma, and Xia, 2004) (Figs. 2.6 and 2.7), focusing on the PMMA due to more available data, and employ the approximation of quasi-elastic solid (Knauss and Zhu, 2002; Schapery, 1965) (see section 2.4), in which the functional form for the material properties is that of a linear elastic solid, but where each effective material constant is assumed to be dependent on the local, instantaneous level of the strain rate. As a consequence of this approximation, the effective wave speeds (or group velocities) of the polymers investigated here are functions of the strain rate (Lee and Swallowe, 2006; Mulliken and Boyce, 2006; Richeton, Ahzi, Vecchio, Jiang, and Adharapurapu, 2006; Richeton, Ahzi, Vecchio, Jiang, and Makradi, 2007; Singh and Parameswaran, 2003; Wu, Ma, and Xia, 2004) (Figs. 2.3, 2.6 and 2.7). In the low-strain-rate (LSR) regime of $|\dot{\epsilon}| = 10^{-4} \text{ s}^{-1}$, the corresponding nominal pressure and shear wave speeds are $c_p^{\text{LSR}} = 1.79 \text{ km/s}$ and $c_s^{\text{LSR}} = 0.86 \text{ km/s}$, respectively (Fig. 2.3; Fig. 2.1c, red and blue solid lines). Since $V_r > c_p^{\text{LSR}}$ (Fig. 2.1c), the rupture propagates supersonically with respect to the effective pressure wave speed of the far field, which experiences the LSR conditions. At the crack tip, much higher strain rates of the order of $|\dot{\epsilon}| = 4 \times 10^3 \text{ s}^{-1}$ develop (Fig. 2.3, bottom inset), constituting the high-strain-rate (HSR) regime; the corresponding effective pressure and shear wave speeds are $c_p^{\text{HSR}} = 2.85 \text{ km/s}$ and $c_s^{\text{HSR}} = 1.37 \text{ km/s}$, respectively (Fig. 2.3; Fig. 2.1c, red and blue dashed lines). Therefore, the rupture propagates intersonically with respect to the HSR wave speeds ($c_s^{\text{HSR}} < V_r = 2.57 \text{ km/s} < c_p^{\text{HSR}}$), in local agreement with basic physics and energy-release-rate analytical models (Freund, 1998; Needleman, 1999; Rice, 2001; Rosakis, Xia, et al., 2007; Rosakis, 2002) of rupture growth in linear-elastic solids. At a representative position along the pressure shock

front, the inclination angle is $\beta_p = 67.5^\circ$ (Fig. 2.3, upper inset). Based on the relation 2.1, this angle corresponds to an intermediate pressure wave speed of $c_p^{\text{ISR}} = V_r \sin(\beta_p) = 2.37$ km/s, consistent with the viscoelastic response at the corresponding strain rate of $|\dot{\epsilon}|^{\text{cp}} = 177$ s⁻¹ (Fig. 2.3, cyan hexagon, and Fig. 2.6, cyan hexagon). This intermediate pressure wave speed is also well below the rupture speed of $V_r = 2.57$ km/s, confirming that the rupture tip travels faster than not only the nominal wave speed but also the pressure wave speed at the examined location of the pressure shock front.

Note that the effectively supersonic rupture propagation observed in our experiments, in the sense of forming the pressure shock front, cannot be explained by a hyperelastic behavior at the crack tip. Hyperelasticity, in which the stiffening occurs with larger strains (in contrast to the strain-rate effects of viscoelasticity) has been suggested by several numerical studies as a potential mechanism for supersonic crack propagation (Abraham and Gao, 2000; Abraham, Walkup, et al., 2002; Buehler, Abraham, and Gao, 2003). However, the constitutive response of PMMA does not manifest hyperelastic stiffening in tension (Mulliken and Boyce, 2006; Wu, Ma, and Xia, 2004), compression (Lee and Swallowe, 2006; Mulliken and Boyce, 2006; Richeton, Ahzi, Vecchio, Jiang, and Makradi, 2007; Richeton, Schlatter, et al., 2005) (Fig. 2.8a and 2.8b), or shear (Fleck, Stronge, and Liu, 1990) experiments for the levels of strains produced by the dynamic cracks in our experiments, which are smaller than 3.2×10^{-3} (Fig. 2.8c).

To summarize, our experimental results capture spontaneously propagating ultra-fast in-plane shear ruptures forming pressure shock fronts in viscoelastic polymers and demonstrate the importance of taking into account the non-uniform viscoelastic stiffening in the vicinity of the rupture front. The presented experimentally obtained ruptures are a striking example of how spatially non-uniform local material stiffening and the associated change in energy transfer can

completely modify the larger-scale processes, leading to the formation of pressure shock fronts and hence apparent spontaneous supersonic crack propagation. Effectively, the dynamics of the process induces a transient heterogeneity in the elastic properties. The non-uniform strain-rate fields associated with the rupture tip and the resulting non-uniform viscoelastic stiffening are essential for the formation of a pressure shock front, in addition to the shear one. These findings are important for a number of engineering and geological applications, as they demonstrate how high and non-uniform strain rates at the crack tip can induce a non-uniform viscoelastic response in the materials that may be treated as uniformly linear elastic under many other conditions. Note that most materials, including rocks (Qiao et al., 2016; Zhang and Zhao, 2014), exhibit viscoelasticity at the high strain-rate regimes characteristic of rapidly propagating dynamic cracks. In studies of dynamic earthquake ruptures, the main emphasis so far has been on how high stresses at the rupture tip can induce damage and hence decrease the effective elastic properties and wave speeds (Ben-Zion, 2008; Cochran et al., 2009; Heap et al., 2010). Our study illustrates the potential of a significant counter-acting phenomenon in which the local elastic properties are transiently increased due to viscoelastic effects, promoting faster rupture propagation, potentially all the way to apparently supersonic ruptures with respect to the wave speeds in most of the bulk.

2.4 Methods

Laboratory setup

The laboratory set-up employed in this study is the described in details in previous works (Gabuchian et al., 2017; Lu, Lapusta, and Rosakis, 2007; Mello, Bhat, and Rosakis, 2016; Mello et al., 2010; Mello et al., 2014; Rosakis, Xia, et al., 2007; Rubino, Rosakis, and Lapusta, 2017; Xia, Rosakis, and Kanamori, 2004). Our specimen configuration features either a $200 \times 250 \times 12.5 \text{ mm}^3$ Poly(Methyl Meth-Acrylate) (PMMA) or a $200 \times 200 \times 10 \text{ mm}^3$ Homalite-100 plate. The sample is separated into two identical halves by an oblique cut at an angle α (Figs. 2.1a and 2.4). The juxtaposition of these two halves creates an interface (green-shaded area). In order to obtain repeatable and desired tribological conditions, these surfaces are polished to near optical-grade finish, and bead-blasted by employing glass particles in the range of 104 – 211 μm diameter (Mello et al., 2010; Rubino, Rosakis, and Lapusta, 2017). A uniform load P is vertically applied to the specimen, resulting in a resolved normal $\sigma_0 = P \cos^2(\alpha)$ and shear ($\tau_0 = P \sin(\alpha) \cos(\alpha)$) stress on the interface. Rupture nucleation is obtained by means of the rapid discharge of an electric potential through a 0.08 mm Ni-Cr wire filament, placed across the interface (Figs. 2.1a and 2.4a). Prior to initiation, electrical charges are accumulated in a capacitor bank in order to achieve a potential of 1.5 (for tests with Homalite-100) to 2 kV (for tests with PMMA). The wire's rapid sublimation produces a short pressure pulse, inducing the rupture initiation by locally frictionally weakening the interface. In this study, we present three tests conducted on PMMA and one test on Homalite-100. All experiments performed with PMMA have an applied far-field load of $P = 21 \text{ MPa}$; one configuration features an inclination angle of $\alpha = 30^\circ$ (Figs. 2.1 and 2.2; Fig. 2.3, top inset; Fig. 2.5; Fig. 2.6, top inset; Fig. 2.8c; and Supplementary Video 1) and the other two are at $\alpha = 29^\circ$

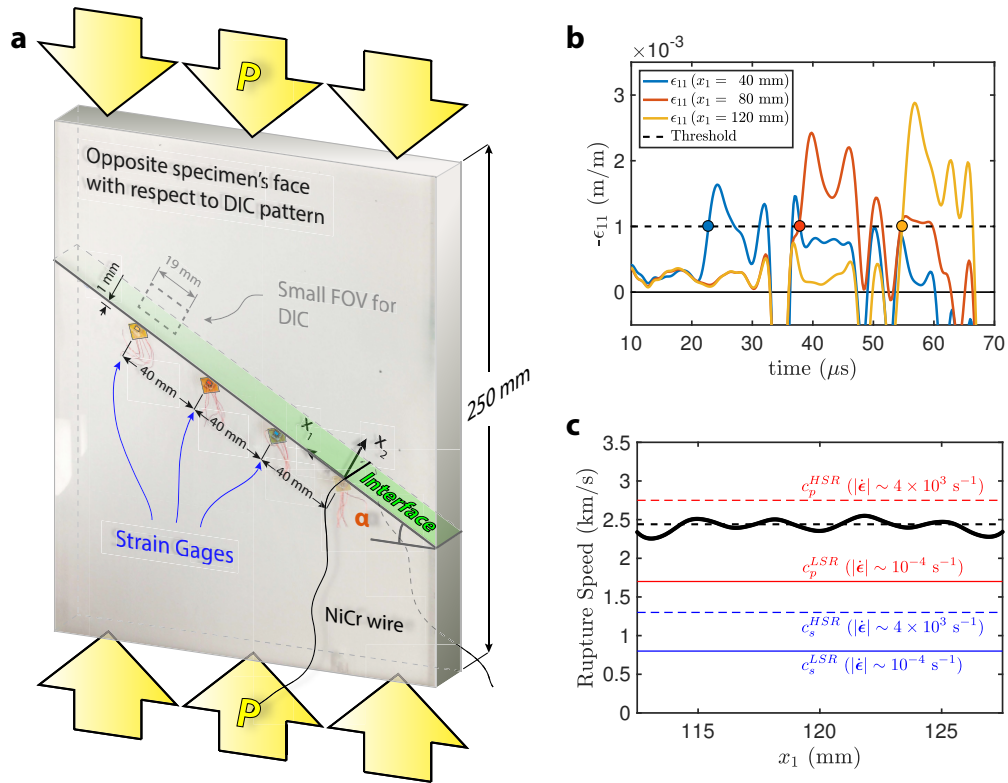


Figure 2.4: Rupture speed computation via DIC and strain gage measurement techniques. Two nominally identical tests are conducted using either the DIC technique or the strain gages. (a) Back-side view of the PMMA sample, where an array of three strain gages has been applied along the interface. These strain stations are positioned approximately 40 mm away from each other, with the first one 40 mm away from the wire’s location. The field-of-view window of the speckled pattern is applied on the front side of the specimen and is indicated by a dashed rectangle ($19 \times 12 \text{ mm}^2$). (b) Time history of the direct strain in the direction parallel to the interface $-\epsilon_{11}$, measured at the three locations shown in Fig. 2.4a. The color of each strain signal matches that of the corresponding locations in Fig. 2.4a. The transit of the rupture is associated with the initial peaks, where positive sign of $-\epsilon_{11}$ indicates compression, in accordance with the right-lateral motion of the rupture. The rupture arrival time has been computed considering a threshold of $|\epsilon_{11, \text{th}}| = 10^{-3}$ (horizontal dashed line). (c) Rupture speed computed using the full-field velocity maps obtained with DIC over the small field of view indicated in Fig. 2.4a. The pressure (red lines) and shear (blue lines) wave speeds are reported, where the LSR and HSR conditions correspond to the solid and dashed lines, respectively. This plot confirms that the rupture is propagating supersonically with respect to the low-strain-rate pressure-wave speed of PMMA. The black horizontal dashed line represents the rupture speed averaged between the three strain-measurement stations.

(Fig. 2.3, bottom inset; Fig. 2.4; and Fig. 2.6, bottom inset). The two tests with $\alpha = 29^\circ$ are used to verify the rupture propagation speed (Fig. 2.4), of which one configuration employs a smaller imaging window in order to achieve higher accuracy with the full-field technique (Fig. 2.3, bottom inset; Fig. 2.4a and c; and Fig. 2.6, bottom inset), and the other one features an array of three strain gauges (Fig. 2.4). The experiment with Homalite-100 is characterized by a far-field load of $P = 25$ MPa and an inclination angle of $\alpha = 29^\circ$ (Fig. 2.2, right column). The full-field images of velocity, strain, and strain rates are obtained by the employment of our dynamic imaging technique based on the combination of ultra-high speed photography, digital image correlation algorithms (Sutton, Orteu, and Schreier, 2009) and post-processing analysis (Rubino, Rosakis, and Lapusta, 2017). The strain-rate magnitude field is computed from the strain-rate components as the Frobenius norm of the tensor: $|\dot{\boldsymbol{\epsilon}}| = \|\dot{\boldsymbol{\epsilon}}\|_F = \sqrt{\dot{\boldsymbol{\epsilon}} : \dot{\boldsymbol{\epsilon}}} = \sqrt{\dot{\epsilon}_{ij} \dot{\epsilon}_{ij}}$, assuming plane-stress conditions.

Wave speed computation

Effective wave speeds are assumed to be a function of the strain rate, by locally adopting linear-elastic relations with the values of elastic moduli dependent on the level of strain rate. In particular, the elastic modulus of PMMA is tracked as a function of the strain rate using measurements derived from the literature (Blumenthal et al., 2002; Chen, Lu, and Cheng, 2002; Foster et al., 2015; Lee and Swallowe, 2006; Li and Lambros, 2001; Moy et al., 2003; Mulliken and Boyce, 2006; Richeton, Ahzi, Vecchio, Jiang, and Adharapurapu, 2006; Richeton, Ahzi, Vecchio, Jiang, and Makradi, 2007; Richeton, Schlatter, et al., 2005; Song and Chen, 2004; Wu, Ma, and Xia, 2004) (Figs. 2.6 and 2.7), ranging from quasi-static compression tests (10^{-5} s^{-1}) to highly dynamic conditions (10^4 s^{-1}). Since these measurements are from uniaxial tests and they need to be related to the three-dimensional strain-rate fields of our tests, we compute

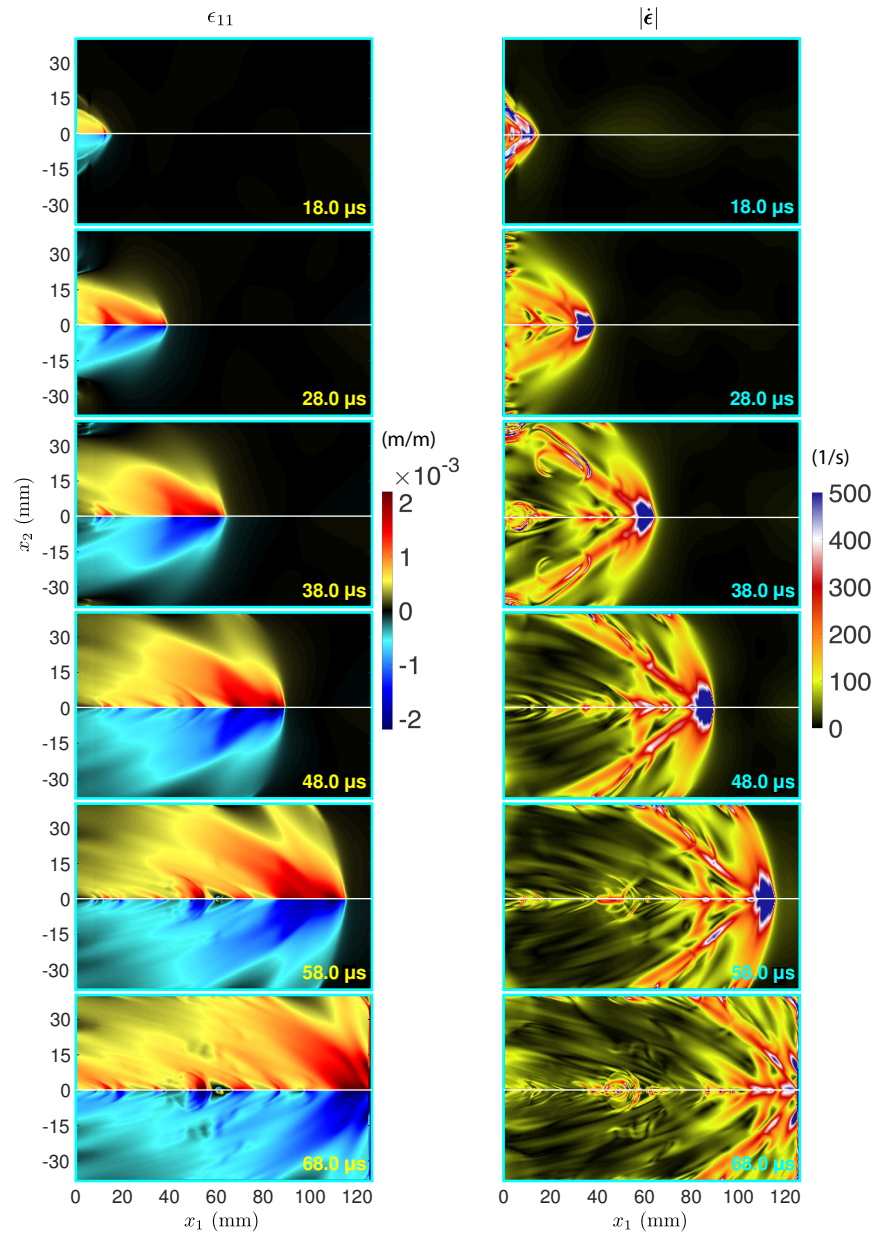


Figure 2.5: Snapshots of full-field images showing the progression of the supersonic rupture. Left column: strain component in the direction parallel to the interface, ϵ_{11} . Right column: strain rate magnitude $|\dot{\epsilon}|$. The collection of images is from the large field of view ($128 \times 80 \text{ mm}^2$) and, as the rupture propagates from left to right in the positive x_1 -direction, each image corresponds to a snapshot from 18 to 68 μs , every 10 μs . In analogy with Fig. 2.2, a double pair of shock fronts is clearly discernible, as they become well developed in the later frames.

the strain-rate magnitude from the corresponding tensor as $|\dot{\epsilon}| = \sqrt{\dot{\epsilon}_{ij} \dot{\epsilon}_{ij}}$. The pressure and shear wave speeds are then calculated as a function of the strain-rate magnitude using the linear-elastic relations for plane strain with the elastic moduli depending on the specific level of strain rate (Figs. 2.3, 2.6, and 2.7): $c_p = \sqrt{E(1-\nu)/[\rho(1+\nu)(1-2\nu)]}$ and $c_s = \sqrt{E/[2\rho(1+\nu)]}$, assuming density $\rho = 1180 \text{ kg/m}^3$ (measured) and a constant Poisson's ratio of $\nu = 0.35$ (Mulliken and Boyce, 2006; Richeton, Ahzi, Vecchio, Jiang, and Makradi, 2007). Least square fits of wave speeds versus strain-rate magnitude are then used to determine the LSR and HSR wave-speed values discussed in the main text and presented in Figures 2.1c and 2.4c. The functional form of the fitted curve is $a + b \log(|\dot{\epsilon}|)$, where $a = 2.24$ and $b = 5.9 \times 10^{-2}$ for the pressure wave speed, and $a = 1.07$ and $b = 2.8 \times 10^{-2}$ for the shear one.

Rupture speed computation

The rupture speed is computed by tracking the rupture tip along the interface using the temporal sequence of the full-field images. In analogy with numerical simulations of shear ruptures (Liu and Lapusta, 2008; Needleman, 1999), we identify the rupture tip as the location where the slip velocity exceeds a preset threshold. The slip velocity $\dot{\delta}$ is obtained from the difference of the \dot{u}_1 particle-velocity component parallel to the interface, immediately above and below it. In our calculations, we use $\dot{\delta}_{\text{th}} = 2.5 \text{ m/s}$ as a threshold for the slip velocity, as it is sufficiently above the noise level to avoid spurious oscillations and still well below the peaks of the slip velocity, which are in the range of 10 to 20 m/s. Setting the threshold within $\pm 1 \text{ m/s}$ does not produce substantial difference in the measurement of the arrival times. Adopting this procedure, the rupture arrival time is identified at each location along the interface and the rupture speed is computed with a second-order accurate central-difference scheme, using the sequence of locations and rupture arrival times (Figs. 2.1c and 2.4c). To validate

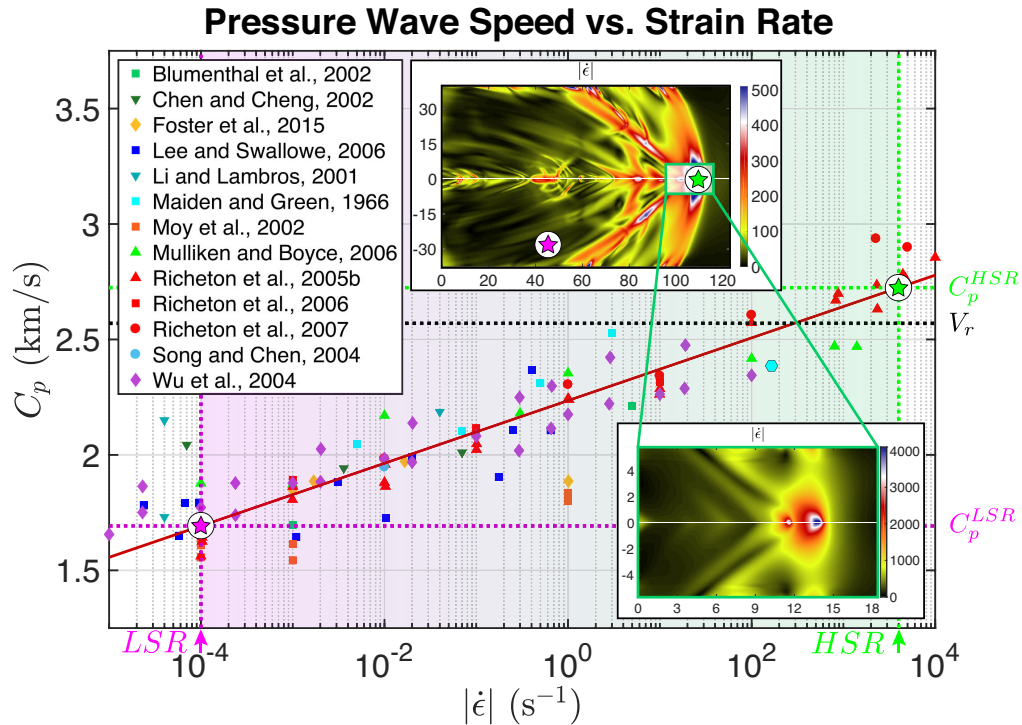


Figure 2.6: Strain-rate dependence of the pressure wave speed in PMMA. The values of the pressure wave speeds have been computed by converting the elastic moduli versus strain-rate data acquired from the literature reported in the legend. Linear-elastic wave relations have been adopted, assuming a density $\rho = 1180$ kg/m³ (measured) and a constant Poisson's ratio $\nu = 0.35$ (Mulliken and Boyce, 2006; Richeton, Ahzi, Vecchio, Jiang, and Makradi, 2007). All symbols indicate compressive tests with the exception of the diamonds, which indicate tensile tests. The cyan hexagon represents the value of c_p measured from the inclination angle (Fig. 2.3, inset). The horizontal black dashed line represents the rupture speed $V_r = 2.57$ km/s, computed from the arrival times (Fig. 2.1, see section 2.4). The upper inset exhibits a snapshot of the equivalent strain-rate field, $|\dot{\epsilon}|$, 58 μ s after triggering. The strain-rate measurements obtained from the full-field images (insets) are reported on the c_p vs. $|\dot{\epsilon}|$ plot for two locations: at the crack tip (green star in upper inset), and after the shock fronts have transitioned ($x_1 = 42$ mm, $x_2 = -29$ mm) (purple star in the upper inset). The green and purple vertical dashed lines refer to the equivalent strain-rate levels for these near-field and far-field measurements, and the corresponding values of the pressure wave speeds are indicated by the horizontal green and purple dashed lines. The strain-rate level at the crack tip is obtained from a similar test performed on a sample at an angle $\alpha = 29^\circ$ (rather than 30°) under the same nominal conditions, yet by focusing on a smaller field of view, which enables a higher strain-rate resolution (lower inset).

the rupture speeds obtained from this procedure, we also compute it from the arrival times at a set of three strain-gage measurement locations, each measuring the direct strain in the direction parallel to the interface, ε_{11} (Fig. 2.4). In this calculation, we select the threshold of the strain signal to be $|\varepsilon_{11,th}| = 10^{-3}$ (Fig. 2.4b, horizontal dashed line).

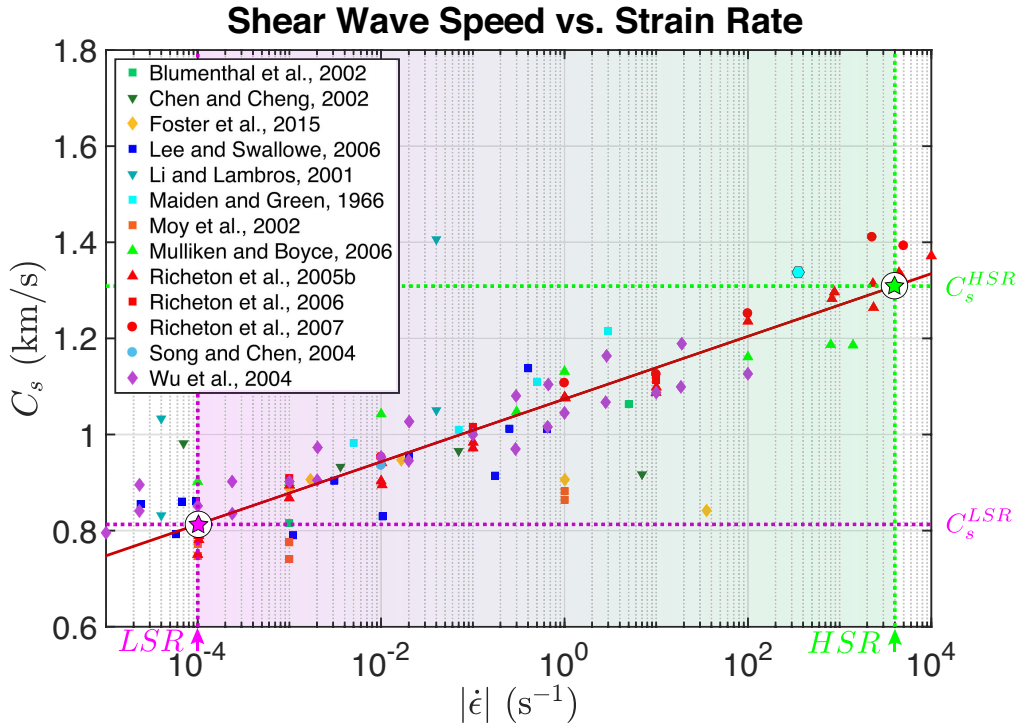


Figure 2.7: Strain-rate dependence of shear wave speed in PMMA. The shear wave speed values have been computed by converting the elastic moduli versus strain-rate experimental data from the literature reported in the legend, using the plane-strain linear-elastic wave relations and assuming a density $\rho = 1180 \text{ kg/m}^3$ (measured) and a constant Poisson’s ratio $\nu = 0.35$ (Mulliken and Boyce, 2006; Richeton, Ahzi, Vecchio, Jiang, and Makradi, 2007). All symbols indicate compressive tests with the exception of the diamonds, which indicate tensile tests. The cyan hexagon represents the value of c_p measured from the inclination angle (Fig. 2.3, inset). The green and purple vertical dashed-lines refer to the equivalent strain-rate levels from the corresponding the green and purple stars presented in Figs. 2.3 and 2.6. The resulting values of the shear wave speeds are indicated by the horizontal green and purple dashed lines.

Two nominally identical experiments have been conducted on PMMA, under a far-field load of $P = 21 \text{ MPa}$ and an inclination angle of $\alpha = 29^\circ$. The rupture

speed has been measured using either the DIC technique (employing a small field of view) or the strain gages (Fig. 2.6). Strain measurements by DIC and strain gages cannot be performed simultaneously in our experiments, since the high-power flash illumination, required for the high-speed image acquisition (Rubino, Rosakis, and Lapusta, 2017; Xing et al., 2017), releases a strong electro-magnetic pulse that interferes with the strain gages, compromising their ability to measure physical strains. The electric discharge, delivered to the Ni-Cr wire for triggering, also induces an electro-magnetic pulse which last several tens of microseconds. This disturbance produces spurious oscillations that overlap with the strain signals, in particular in the proximity of the wire's notch (Fig. 2.4a and b). However, the main features associated with the transit of the rupture are still clearly identifiable and allow precise rupture arrival time calculations, whose results are in excellent agreement with the DIC ones (Fig. 2.4c).

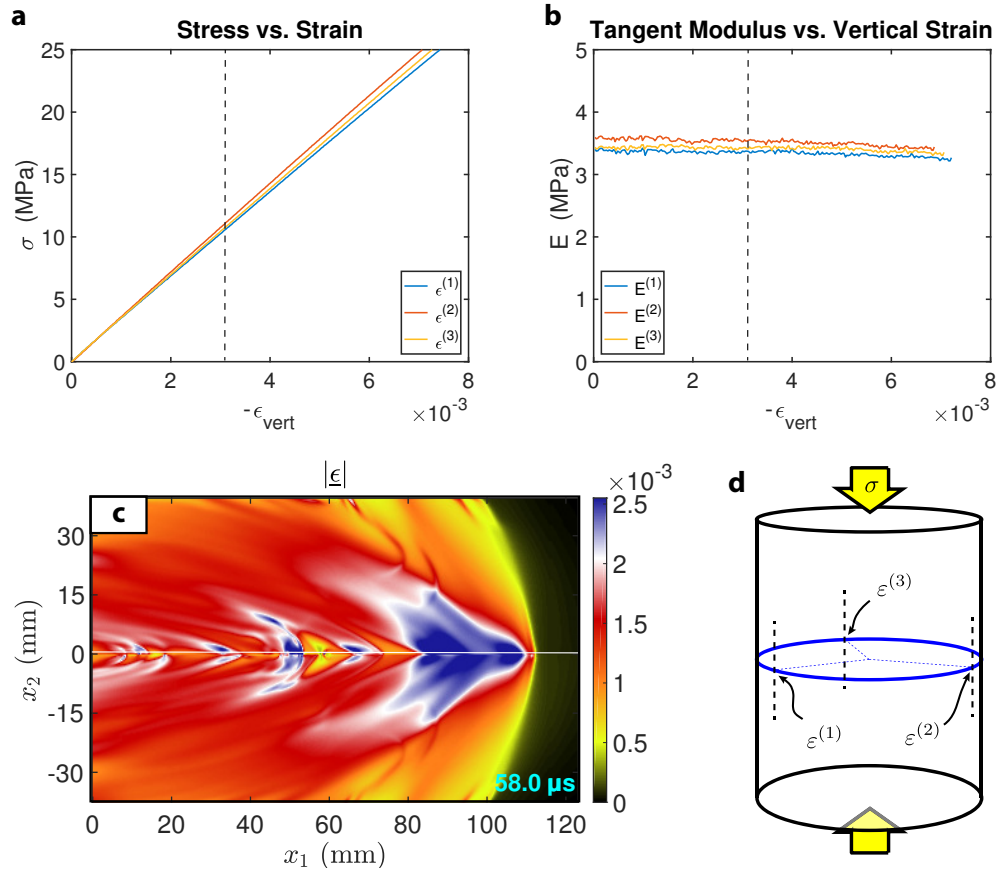


Figure 2.8: Strain dependence of elastic modulus in PMMA. **(a)** In a quasi-static test on PMMA, $|\dot{\epsilon}| \sim 10^{-4} \text{ s}^{-1}$, the stress shows a linear dependence with strain, up to stresses of 25 MPa and strains of 7×10^{-3} . **(b)** The elastic modulus, computed as the local tangent of the stress-strain curve, does not show the presence of stiffening. **(c)** The full-field equivalent strain $|\epsilon|$ shows that our propagating dynamic cracks does not produce elevated levels of strain (smaller than 3.2×10^{-3}) while inducing elevated levels of strain rate at the crack tip (well above 10^3 s^{-1} , Fig. 2.3 inset below), which would fail to activate hyperelastic effects, in favor of viscoelastic ones. **(d)** Setup employed to produce the results presented in **a** and **b**. Three strain gages equally spaced around the circumference (blue line) of a PMMA cylinder (from the same manufacturer of our samples) measure the vertical component of strain as the load is applied vertically (yellow arrows).

CHAPTER 3

Inferring dynamic material properties from curved shock fronts of supersonic shear cracks in viscoelastic solids

3.1 Introduction

Due to the relatively recent diffusion of polymers in structural and impact-absorption applications, both in composite materials and on their own, the investigation of their mechanical properties has earned great interest. A large volume of publications exists investigating these properties at different temperatures, strains, strain rates, and loading conditions; however, this abundance of literature drastically decreases in the high strain-rate regime, due to the additional difficulties this problem poses (Siviour, Walley, et al., 2005; Siviour and Jordan, 2016). The Split-Hopkinson pressure bar (SHPB) is an experimental

apparatus widely diffused due to its intrinsic ability to induce elevated levels of strain rate. Its relatively simple operating principle is based on compressional (or tensional) waves impacting a sample, in which, through a small number of wave reverberations (typically between 3 and 4) internal stress equilibrium is achieved (Gama, Lopatnikov, and Gillespie, 2004). During this transient time, not only the stress, but also the strain and strain-rate levels ramp up. The inability of attaining strain-rate equilibrium during the initial loading phase jeopardizes the ability of quantifying the material properties from the stress-strain curve, as is commonly done in linear elasticity (*ibid.*). For this reason, usual outputs of SHPB experiments on polymers include: true stress versus true strain (during ramping-up strain rates) or strain-rate; yield stress versus strain rate or temperature; and peak stress versus strain rate or temperature (Chou, Robertson, and Rainey, 1973; Gama, Lopatnikov, and Gillespie, 2004; Mulliken and Boyce, 2006; Richeton, Ahzi, Vecchio, Jiang, and Adharapurapu, 2006; Siviour, Walley, et al., 2005; Siviour and Jordan, 2016; Walley and Field, 1994). However, wave speeds or elastic material constants cannot be estimated using this technique. In polymers, the time-temperature superposition principle is a well-known procedure to expand the time or frequency domain at a given temperature at which the material behavior is studied (Bauwens-Crowet, 1973; Capodagli and Lakes, 2008; Lakes, 2004; Li, 2000; Lu, Zhang, and Knauss, 1997; Plazek, 1996; Siviour and Jordan, 2016; Van Gorp and Palmen, 1998). Polymers following this behavior are called “thermo-rheologically simple” (Schwarzl and Staverman, 1952). However, due to their molecular dynamics, polymers are characterized by complex behaviors at varying temperatures (some of which excitable at high strain rates). Although the time-temperature superposition principle is widely-accepted and demonstrated in the rubbery domain for a broad class of materials, its accuracy (or even applicability) needs to be investigated on a case-by-case basis, which often represents the exception, rather than the

rule (Capodagli and Lakes, 2008; Lakes, 2004; Li, 2000; Plazek, 1996; Sane and Knauss, 2001; Van Gurp and Palmen, 1998).

In this study, we present an alternative method to quantify the wave speeds of viscoelastic solids in the dynamic range of strain rates and, by invoking the quasi-elastic solid approximation, the elastic modulus can be derived under the assumption of constant Poisson's ratio (Davies and Hunter, 1963; Mulliken and Boyce, 2006; Richeton, Ahzi, Vecchio, Jiang, and Makradi, 2007). Our tests are performed at room temperature, yet we do not foresee any physical reason limiting this method from being applied at higher ones. It has been demonstrated that viscoelasticity can enable the rupture tip to outrun the speed of the pressure wavelets of the undisturbed, bulk material (see chapter 2), with the consequent formation of two sets of shock fronts, the pressure and the shear one. In the quasi-elastic solid assumption, the *local* inclination angle of these fronts in relationship to the corresponding level of strain rate is connected to the spatially-varying material properties of PMMA, which have been derived by the employment of our dynamic imaging acquisition system (chapter 2; Rubino, Rosakis, and Lapusta, 2017), ad hoc optimized for this problem.

3.2 Experimental Design

In order to investigate the shock fronts inclination angle as a result of the spatially inhomogeneous viscoelastic response of the material, a $200 \times 250 \times 12.5 \text{ mm}^3$ PMMA sample was prepared by cutting it into two identical halves along a plane inclined by an angle α with respect to the horizontal direction (Fig. 3.1). These oblique surfaces are polished and bead blasted in order to obtain desired and repeatable tribological conditions and then juxtaposed to give rise to a frictional interface. An external compressive load P (yellow arrows) is vertically applied by a hydraulic press and held constant. Since the measurement

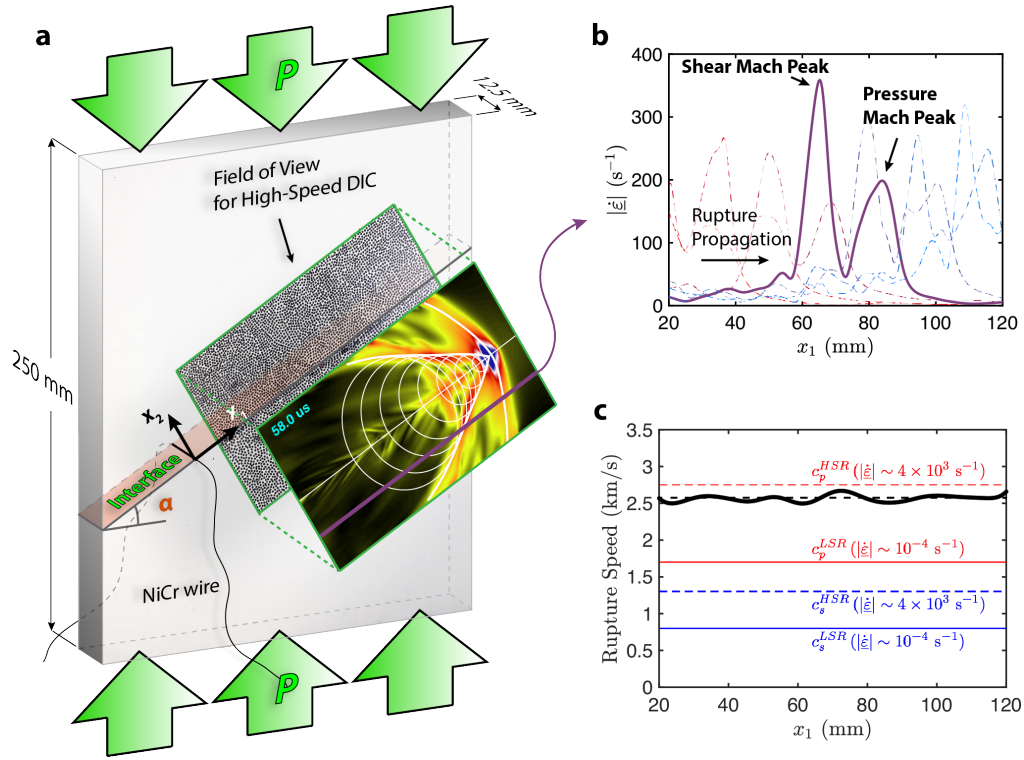


Figure 3.1: Laboratory setup and the captured supersonic shear ruptures. (a) The dynamic rupture is produced on a sample interface (red-shaded area) loaded in compression and shear by a compressive vertical load (green arrows). The rupture is triggered by the sudden disintegration of a Ni-Cr wire filament and subsequently propagates spontaneously over the interface. Its dynamics is captured using a speckle pattern applied over a portion of the specimen's surface, ultrahigh speed photography, and DIC algorithms. The inset exhibits the full-field strain-rate magnitude, $|\dot{\epsilon}|$, 58 μs after nucleation. The white lines highlight the peaks associated to the pressure and shear Mach cones, and the white circles are representative of how the shear shock front is generated by the coalescence of the shear wavelets. An analogous construction – not shown here – applies to the pressure cone. (b) The profile of the strain-rate magnitude, $|\dot{\epsilon}|$, along the violet line (at a distance $x_2 = -16.5$ mm from the interface), plotted at time intervals of 6 μs , exhibits two recognizable peaks associated to the pressure and shear shock fronts. (c) The rupture speed versus position along the interface, x_1 , is computed by tracking the rupture tip in the temporal sequence of velocity maps. The comparison with the pressure wave speed in the bulk material, where low strain rates are attained (see chapter 2), confirms the supersonic nature of the rupture, $V_r > c_p^{LSR}$. At the crack tip, where considerably higher strain rates develop, the rupture is locally intersonic, $c_s^{HSR} < V_r < c_p^{HSR}$.

window of the dynamic rupture is confined to instances before the reflection of the waves and crack tip from the boundaries of the specimen, constant-load conditions are preserved throughout the entire duration of the experiment. The oblique interface experiences a resolved shear and normal stress $-P \cos(\alpha)$ and $P \sin(\alpha) \cos(\alpha)$ respectively – and consequently develops a frictional resistance proportional to the resolved normal stress, $\tau_{\text{res}} = f(\sigma_n - p)$, in competition with the resolved shear one. A 0.1-mm notch, excavated across the interface, hosts a 0.08-mm NiCr wire filament. Upon the discharge of a 2-kV potential through it, the wire’s rapid sublimation locally increases the pressure, which competes with the resolved normal stress and ultimately nucleates the rupture by frictionally weakening the interface. On one side of the specimen, a thin coat of white paint is deposited on the lateral face to create a background where a random black pattern of optimally-sized dots is added 3.1. A ultra-high-speed camera, capable of acquiring 128 images at up to 5-million frames per second (5 Mfps), records the deformation of the pattern across different frames as the dynamic rupture transits through the field of view (FOV). This pattern-deformation is converted into in-plane displacement fields via digital image correlation (DIC) algorithms (Sutton, Orteu, and Schreier, 2009). Images are then filtered by means of non-local (NL) de-noising algorithms (Buades, Coll, and Morel, 2008; Rubino, Rosakis, and Lapusta, 2017) and numerically differentiated with respect to time, space, or both time and space, in order to obtain velocity, strain, and strain-rate fields, respectively (see Chapter 2). All the full-field results are presented in the reference frame relative to the oblique interface, where the x_1 -direction is along the fault plane and the x_2 -direction is normal to it (Fig. 3.1). The rupture propagates along the $x_2 = 0$ -plane and crosses the FOV from left to right in the positive x_1 -direction (Figs. 3.1, 3.2 and 3.3). In this manuscript, two configurations are presented: **(a)** $P = 21$ MPa, $\alpha = 30^\circ$, “large” FOV (128×80 mm²) at 1-million frames-per-second; and **(b)** $P = 21$ MPa, $\alpha = 29^\circ$,

“small” FOV ($19 \times 12 \text{ mm}^2$) at 2-million frames-per-second. The relatively low shear modulus of PMMA ($\approx 1.2 \text{ GPa}$) guarantees well-developed ruptures (Fialko, 2007; Lu, Lapusta, and Rosakis, 2009; Rice, 2001), which reach steady-state conditions early after being nucleated, before entering the portion of the sample covered by the ultra-high-speed photography (Fig. 3.1c).

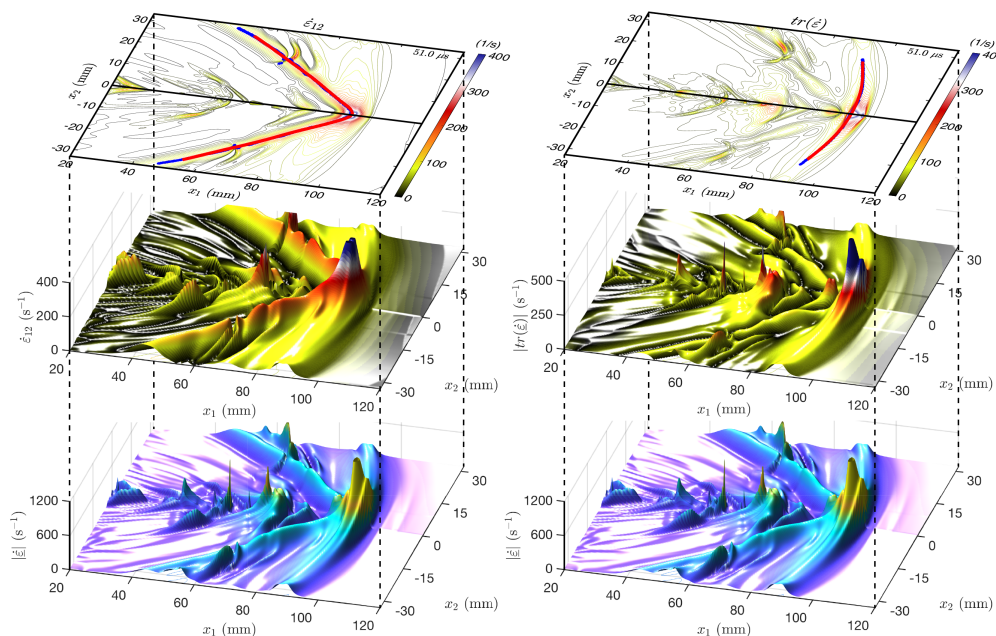


Figure 3.2: Snapshot of the shear strain-rate field (top and center left), $\dot{\epsilon}_{12}$, and volumetric strain-rate one (top and center right), $\text{tr}(\dot{\epsilon})$, $51 \mu\text{s}$ after the rupture initiation. The curved shear Mach cone (**a**) and bow pressure shock front (**b**) are traced as the locus of maxima (blue line) of the shear strain-rate field (**a** and **c**) and volumetric strain-rate field (**b** and **d**), respectively. (**d**) The volumetric strain-rate field enhances the presence of the pressure shock front, while ‘hiding’ that of the shear Mach cone. (**c**) The shear strain-rate field does the opposite, by showing a healthy shear shock front and a less developed pressure one. In (**a**) and (**b**), the red line superimposed to the blue one is the result of a moving average smoothing procedure, which is employed in order to eliminate spurious effects. (**e** and **f**) 3D snapshots of strain-rate magnitude allow the correlation of each location of the shock fronts (red lines) with a corresponding value of strain rate (Fig. 3.3 and 3.5a).

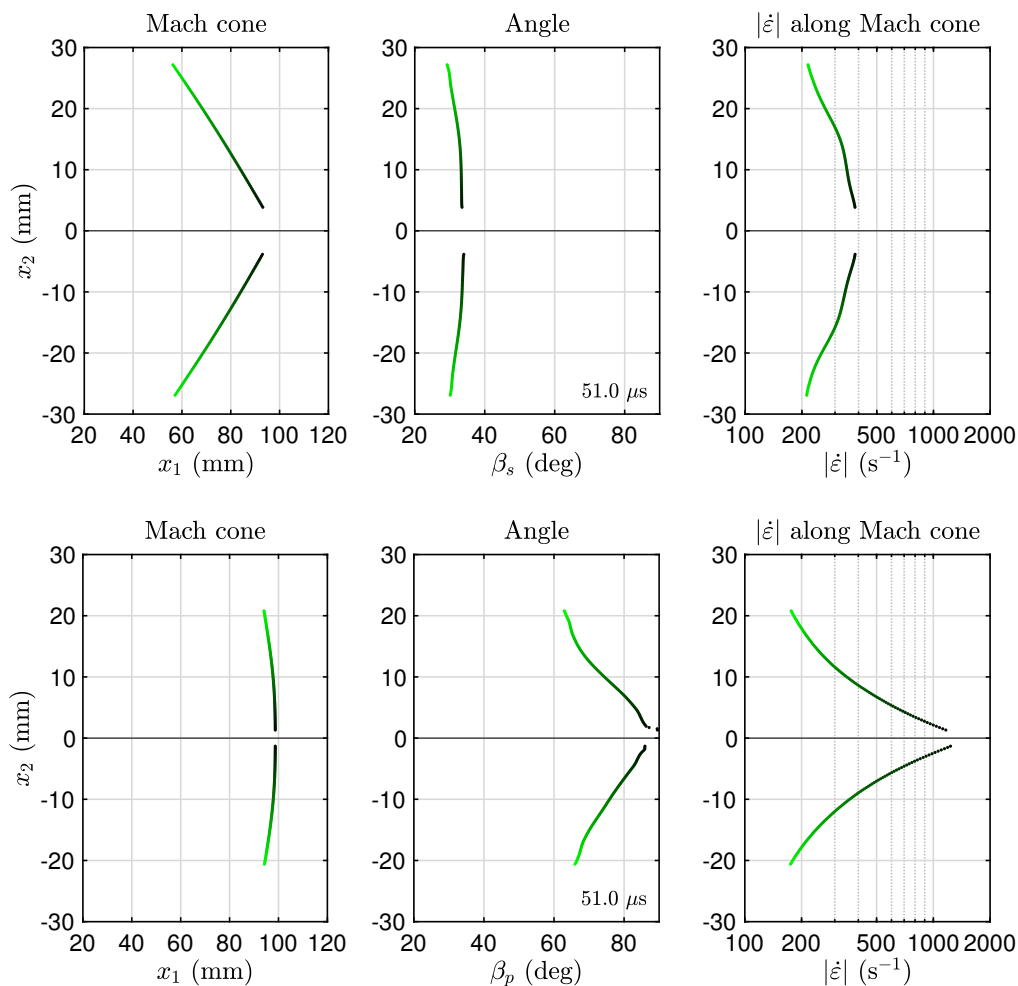


Figure 3.3: Mach cone angle and strain-rate magnitude variation along the shear **(a)** and pressure **(d)** Mach cones obtained from Fig.3.2a and b, $51 \mu\text{s}$ after the rupture initiation. The black portion corresponds to locations along the Mach cone in proximity to the rupture tip, which gradually turns green while moving away from it. **(b)** The shear Mach cone angle, computed by differentiating the shear Mach cone with respect to x_2 , is higher in proximity to the crack tip ($\approx 34^\circ$), and gradually reduces moving away from it ($\approx 30^\circ$). Similarly, **(e)** the pressure shock front angle approaches 90° close to the rupture tip and decreases to about 65° away from it. **(c)** The strain-rate magnitude along the shear Mach cone varies between 2×10^2 and $4 \times 10^2 \text{ s}^{-1}$, while **(f)** the one along the pressure shock front varies between 1.5×10^2 and $1 \times 10^3 \text{ s}^{-1}$.

3.3 Results and Discussion

The Strain-Rate Dependence of the Wave-Speeds

Polymeric materials are known to undergo viscoelastic stiffening at higher strain rates (Capodagli and Lakes, 2008; Lakes, 2004; Lu, Zhang, and Knauss, 1997; Mulliken and Boyce, 2006; Richeton, Ahzi, Vecchio, Jiang, and Adharapurapu, 2006; Sane and Knauss, 2001; Siviour and Jordan, 2016; Tschoegl, Knauss, and Emri, 2002), which is reflected by the development of higher wave speeds. Indeed, a number of studies on polymers show that many of them – including PMMA – exhibit an increase of the yield stress or peak stress dependence with strain rate (at room temperature) above 10^2 s^{-1} (Bauwens-Crowet, 1973; Chou, Robertson, and Rainey, 1973; Jordan et al., 2014; Mulliken and Boyce, 2006; Richeton, Ahzi, Vecchio, Jiang, and Adharapurapu, 2006; Rittel and Brill, 2008; Siviour, Walley, et al., 2005; Siviour and Jordan, 2016; Walley and Field, 1994). In a quasi-elastic solid approximation (Knauss and Zhu, 2002; Schapery, 1965), the relationship between the material properties preserves the same functional form as in the linear elastic counterpart; however, each property depends on the strain-rate history the material undergoes during deformation. In particular, the pressure wave speed is a function of the local material properties, which, in turn, depend on the strain-rate history:

$$c_p(|\dot{\boldsymbol{\epsilon}}(\mathbf{x}(t), t)|, t) = \sqrt{\frac{E(|\dot{\boldsymbol{\epsilon}}(\mathbf{x}(t), t)|, t)[1 - \nu(|\dot{\boldsymbol{\epsilon}}(\mathbf{x}(t), t)|, t)]}{\rho[1 + \nu(|\dot{\boldsymbol{\epsilon}}(\mathbf{x}(t), t)|, t)][1 - 2\nu(|\dot{\boldsymbol{\epsilon}}(\mathbf{x}(t), t)|, t)]}} \quad (3.1)$$

where \mathbf{x} is the spatial coordinate, t is the time, E is the Young's modulus, ν is the Poisson's ratio, ρ is the density, which is assumed to be constant $\rho = 1180 \text{ kg/m}^3$ (measured), and $|\dot{\boldsymbol{\epsilon}}|$ is the strain-rate magnitude field computed from the strain-rate components as the Frobenius norm of the tensor: $|\dot{\boldsymbol{\epsilon}}| = \|\dot{\boldsymbol{\epsilon}}\|_F = \sqrt{\dot{\boldsymbol{\epsilon}} : \dot{\boldsymbol{\epsilon}}} = \sqrt{\dot{\epsilon}_{ij} \dot{\epsilon}_{ij}}$.

In steady-state rupture propagation conditions, the explicit dependence on time drops. In addition, if the strain-rate temporal history is uneventful prior to the arrival of the main signal, such as in sharp events like the transition of a shock front, it can be neglected. Under this assumption, the time dependence of the strain rate disappears and the material properties – as well as the pressure wave speed – only depend on the *local*, current value of strain rate. Finally, by neglecting the dependence of the Poisson’s ratio on the strain rate (Davies and Hunter, 1963; Mulliken and Boyce, 2006; Richeton, Ahzi, Vecchio, Jiang, and Makradi, 2007), one obtains:

$$c_p(|\dot{\boldsymbol{\epsilon}}(\mathbf{x}(t))|) = \sqrt{\frac{E(|\dot{\boldsymbol{\epsilon}}(\mathbf{x}(t))|)(1 - \nu)}{\rho(1 + \nu)(1 - 2\nu)}} \quad (3.2)$$

Although this assumption can be directly applied to the pressure shock front due to the absence of strain-rate signals ahead of it (Figs. 3.1a, inset, 3.1b, 3.2, and 3.4), for the shear Mach cone this hypothesis carries some degree of approximation because of the strain-rate history associated to the pressure shock front ahead of it (Figs. 3.1a, inset, 3.1b, 3.2, and 3.4). Due to the added complexity of this scenario, we leave the viscoelastic investigation of the shear Mach cone to a future study and we concentrate here only on the pressure shock front. This will limit the number of material parameters that can be derived, including the viscoelastic dependence of the Poisson’s ratio with strain rate (Limbach, Rodrigues, and Wondraczek, 2014; Lu, Zhang, and Knauss, 1997; Yee and Takemori, 1982); however, there are a number of fundamental conclusions that can be drawn without the inclusion of the shear Mach cone viscoelastic response.

Finally, in order to reduce the number of parameters under investigation and due to the difficulty of accurately measuring the Poisson’s ratio (Lu, Zhang, and Knauss, 1997; Sane and Knauss, 2001; Tschoegl, Knauss, and Emri, 2002; Yee and Takemori, 1982), its dependence on the strain rate has been neglected (Davies and

Hunter, 1963; Mulliken and Boyce, 2006; Richeton, Ahzi, Vecchio, Jiang, and Makradi, 2007), although other studies have shown that this assumption comes with some degree of approximation (Limbach, Rodrigues, and Wondraczek, 2014; Lu, Zhang, and Knauss, 1997; Yee and Takemori, 1982).

The rupture tip, in its propagation along the frictional interface, induces a dynamically-varying, spatially-inhomogeneous state of strain rates (Figs. 3.1, 3.2 and 3.3) (chapter 2). In particular, high strain rates (HSR) – of the order of 10^3 s^{-1} – arise about the crack tip, while low strain rates (LSR) – of the order of 10^{-4} s^{-1} – are present in the undisturbed, bulk material away from it. The rupture tip is locally intersonic with respect to the HSR conditions ($c_s^{\text{HSR}} < V_r < c_p^{\text{HSR}}$), in agreement with basic physics and energy considerations of linear-elastic theories (Broberg, 1999; Freund, 1998; Needleman, 1999; Rice, 2001; Rosakis, Xia, et al., 2007; Rosakis, 2002; Slepyan, 2002), and therefore a shear Mach cone is formed behind it (Fig.3.1a, inset, and 3.2) (Mello, Bhat, and Rosakis, 2016; Mello et al., 2010; Rosakis, Xia, et al., 2007; Xia, Rosakis, and Kanamori, 2004). In addition, the strain rates rapidly decrease away from the rupture tip, with consequent decrease of the wave speeds; see equation 3.2. When the local speed of the pressure wavelets is exceeded by the rupture speed, an additional shock front, the pressure one, forms in front of the shear one (Figs. 3.1a, inset, 3.1b, 3.2, 3.3, and 3.4) (see Chapter 2). Under these conditions, we refer to the rupture tip as “supersonic” with respect of the low wave speeds ($V_r > c_p^{\text{LSR}}$), where we define “low strain rates” (LSR) the strain rates developing in the undisturbed, bulk material ahead of the pressure shock front, where both the pressure and shear wave speeds are locally lower than the rupture speed. The spatially inhomogeneous strain-rate field, due to the viscoelastic nature of our sample material, induces another interesting feature: the variable inclination of the shock fronts (Figs. 3.2 and 3.3) (see Chapter 2).

The Curvature of the Shock Fronts due to Viscoelastic Effects

In linear elastic materials, the ratio between the shear wave speed and the rupture speed is equal to the sine of the inclination angle of the shear Mach cone:

$$\sin(\beta_s) = \frac{c_s}{V_r} \quad (3.3)$$

We will prove that this kinematic relation still holds for viscoelastic solids, provided that two conditions are satisfied: **(a)** the value of the shear quantities, c_s and β_s , must be selected on a local basis, since they are functions of the local state of strain rate; and **(b)** the rupture propagates in steady-state conditions, so that $V_r = \text{const}$. The second condition is easily witnessed in our ruptures, since, by tracking the rupture tip location in the temporal sequence of full-field images (Fig. 3.1c), its small variation inside our observation window suggests that steady-state conditions are in fact attained. For this reason, we simply consider the rupture speed average value along the x_1 -coordinate, $V_r = 2.56 \text{ km/s}$ (Fig. 3.1c, black dashed line) 2.

In order to relate the shock front inclination angle to the local value of the corresponding wave speed, let us consider two consecutive locations along the interface ($x_2 = 0$), $x_1^{(1)}$ and $x_1^{(2)}$, which are separated by a time interval $\delta t = t^{(2)} - t^{(1)}$ required by the rupture tip to cover the distance $\delta x_1 = x_1^{(2)} - x_1^{(1)} = V_r \delta t$ (Fig. 3.4), where the superscript indicates either one of the two locations. At each one of them, the rupture tip emits a shear and a pressure wavelet (see chapter 2) (Mello, Bhat, and Rosakis, 2016; Mello et al., 2010). For the sake of simplicity, we shall concentrate on the shear case for the moment. The distance $l^{(i)}$ covered by the i -th wavelet connecting the location of its emission $x_1^{(i)}$ to the shear Mach cone (Fig. 3.4, curved dashed lines) is equal to:

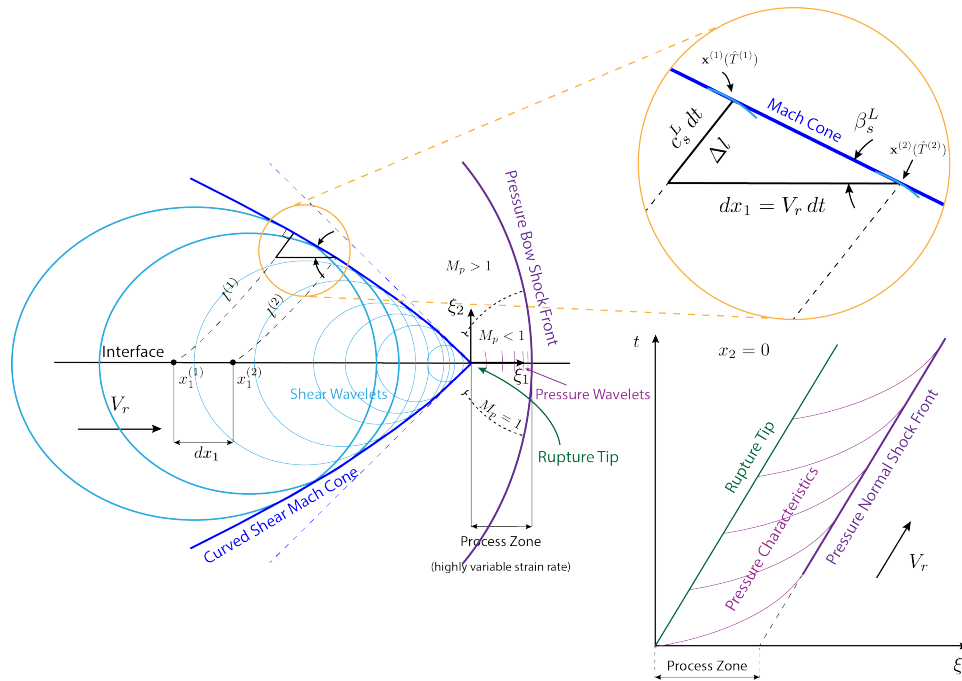


Figure 3.4: Shock fronts profiles and local inclination angles. A shock front (thick darker blue and purple lines) is formed as the coalescence of multiple wavelets (thin lighter blue and purple lines) emanated by the rupture tip at several time instances, as it propagates along the interface. As a shear wavelet (thin lighter blue lines) travels through the viscoelastic solid, it encounters regions at different levels of strain-rates, loses circularity and, consequently, the locus of points of tangency with the Mach cone assumes a curvature (black dashed lines). Two consecutive wavelets are emanated at a distance $dx_1 = V_r(t) dt$. Due to their proximity with each other, they follow the same strain-rate history during their propagation. The additional distance traveled by the first of the two is $c_s(t) dt$ (inset), while $V_r(t) dt$ is the distance traveled by the rupture tip before emitting the second wavelet into existence. The shear Mach cone local inclination angle β_s is computed by using the general formula $\beta_s = \sin^{-1}(c_s/V_r)$, provided that the local values of c_s and V_r are considered. In addition, the pressure shock front forms ahead of the shear one, as a testimony that the rupture tip exceeds the pressure wave speed of the undisturbed, bulk material ($V_r > c_p^{LSR}$) (see chapter 2). The small field of view (Fig. 3.5, insets) highlights the presence of an offset – or “process zone” – between the two shock fronts at the interface ($x_2 = 0$), which is related to the presence of a high strain-rate region ahead of the rupture tip. The normality ($\beta_p \rightarrow 90^\circ$) of pressure shock front at the interface ($x_2 = 0$) is an indication of the high levels of strain rates and the generation of a subsonic region ($M_p < 1$) between the front and the rupture tips. Moving away from the interface ($x_2 \neq 0$), the shock front curves and loses strength until, at some point, the strain-rate level behind it is not high enough for the pressure wavelets to outrun the rupture tip, which is thus supersonic ($M_p > 1$) with respect of that region. The x_1 - t -diagram – at $x_2 = 0$ – qualitatively shows the coalescence of pressure characteristics (which represent the local position and time of the wavelets) into the shock front ahead of the rupture tip, traveling at the same speed as the rupture tip (bottom right).

$$l^{(i)} = \int_{t^{(i)}}^T c_s \left(\mathbf{x}^{(i)}(\tau), \tau \right) d\tau \quad (3.4)$$

where T is the (present) time when each wavelet reaches the Mach cone, $t^{(i)}$ is the (past) time of emission of the i -th wavelet into existence, $\mathbf{x}^{(i)}(t)$ is the path followed by the i -th wavelet, and c_s is the shear wave speed, which, in general, depends on both the spatial location and the time. In steady-state conditions, the explicit dependence on time can be neglected:

$$l^{(i)} = \int_{t^{(i)}}^T c_s \left(\mathbf{x}^{(i)}(\tau) \right) d\tau \quad (3.5)$$

and the difference between the distances covered by the two consecutive shear wavelets is equal to:

$$\Delta l = l^{(1)} - l^{(2)} = \int_{t^{(1)}}^T c_s \left(\mathbf{x}^{(1)}(\tau) \right) d\tau - \int_{t^{(1)} + \delta t}^T c_s \left(\mathbf{x}^{(2)}(\tau) \right) d\tau \quad (3.6)$$

At this point, time can be shifted for each wavelet $\hat{t}_i = t - t^{(i)}$ so that $\hat{t}_i = 0$ corresponds to the instant the wavelet has been emitted into existence. Equation 3.6 then becomes:

$$\Delta l = \underbrace{\int_0^{\hat{T}^{(1)}} c_s \left(\mathbf{x}^{(1)}(\hat{t}_1) \right) d\hat{t}_1}_{\int_0^{\hat{T}^{(2)}} c_s \left(\mathbf{x}^{(1)}(\hat{t}_1) \right) d\hat{t}_1 + \int_{\hat{T}^{(2)}}^{\hat{T}^{(2)} + \delta \hat{t}} c_s \left(\mathbf{x}^{(1)}(\hat{t}_1) \right) d\hat{t}_1} - \int_0^{\hat{T}^{(2)}} c_s \left(\mathbf{x}^{(2)}(\hat{t}_2) \right) d\hat{t}_2 \quad (3.7)$$

We notice that $\delta \hat{t} = \hat{T}^{(1)} - \hat{T}^{(2)} = (T - t^{(1)}) - (T - t^{(2)}) = t^{(2)} - t^{(1)} = \delta t$. In the limit of $\delta t \rightarrow 0$, $\delta t \equiv dt$ and $\mathbf{x}^{(2)}(\hat{t}_2)$ approaches $\mathbf{x}^{(1)}(\hat{t}_1)$ over the time interval $\hat{t}_i \in [0, \hat{T}^{(2)}]$ (Fig. 3.4). This limit corresponds to the very-close emission of two consecutive wavelets, reflecting the physical principle that wavelets are

continuously emitted by the rupture tip during its motion. By simplifying the equal-and-opposite terms in equation 3.7, one obtains:

$$\Delta l = \int_{\hat{T}^{(2)}}^{\hat{T}^{(2)}+dt} c_s \left(\mathbf{x}^{(1)}(\hat{t}) \right) d\hat{t} \quad (3.8)$$

The Taylor expansion of $c_s \left(\mathbf{x}^{(1)}(\hat{t}_1) \right)$ about $\hat{t}_1 = \hat{T}^{(2)}$ is:

$$c_s \left(\mathbf{x}^{(1)}(\hat{T}^{(2)} + \delta t) \right) = c_s \left(\mathbf{x}^{(1)}(\hat{T}^{(2)}) \right) + \frac{dc_s}{d\mathbf{x}^{(1)}} \frac{d\mathbf{x}^{(1)}(\hat{T}^{(2)} + \delta t)}{dt} (dt) + O(dt^2) \quad (3.9)$$

By substituting this expression into equation 3.8 and neglecting all higher-order terms, one obtains:

$$\Delta l = \int_{\hat{T}^{(2)}}^{\hat{T}^{(2)}+dt} c_s \left(\mathbf{x}^{(1)}(\hat{T}^{(2)}) \right) d\hat{t} = c_s \left(\mathbf{x}^{(1)}(\hat{T}^{(2)}) \right) \int_{\hat{T}^{(2)}}^{\hat{T}^{(2)}+dt} d\hat{t} = c_s \left(\mathbf{x}^{(1)}(\hat{T}^{(2)}) \right) dt \quad (3.10)$$

where $c_s(x^{(1)}\hat{T}^{(2)})$ represents the *local* shear wave speed at the shear Mach cone. In a compact notation, here it is indicated as c_s^L , where the superscript L stands for “local”. By applying the same trigonometric considerations adopted in linear-elastic solids to derive the equation 3.3 (Fig. 3.4, inset), we can now derive the corresponding expression for the viscoelastic case:

$$\sin(\beta_s^L) = \frac{c_s^L dt}{V_r dt} = \frac{c_s^L}{V_r} \quad (3.11)$$

which closely mimics the linear elastic counterpart, with the caveat that the shear quantities must be considered locally. Following analogous considerations, an equivalent expression holds for the pressure shock front:

$$\sin(\beta_p^L) = \frac{c_p^L dt}{V_r dt} = \frac{c_p^L}{V_r} \quad (3.12)$$

Shock Fronts: a Comparison Between Viscoelastic Solids and Fluids

Pressure shock fronts are commonly observed in fluids and plasma, where a large number of studies have been carried out to understand their nature (Anderson Jr, 2010; Decker et al., 2005; Gurnett and Kurth, 2005; Liepmann and Roshko, 1957; Roe, 1981), however, prior to the work presented in chapter 2, they had never been observed in homogeneous solids in relation to crack evolution problems. Significantly, the pressure shock front at the interface not only is detached from the rupture tip, but also assumes a characteristic curvature moving away from the interface, which confers it the name of “bow (or detached) shock front” (Fig. 3.1, inset, Fig. 3.2; Fig. 3.3d and e; and Fig. 3.4). This phenomenon is well known in the gasdynamics community (Anderson Jr, 2010; Liepmann and Roshko, 1957) and arises when a body supersonically travels in a flow, or, in a reference frame anchored to the body, $\xi_1 = x_1 - V_r \Delta t$ and $\xi_2 = x_2$ (Fig. 3.4), when a body is invested by a supersonic flow, and two conditions are satisfied: (a) the body has a finite thickness in the ξ_2 -direction normal to the flow; and (b) the flow does exceed the pressure wave speed (known in fluids as “speed of sound”), yet not by a “large” amount. In fact, the larger the ratio of the speed of the flow versus the pressure wave speed – called Mach number, M_p –, the closer the shock front approaches the body. For blunt bodies, this gap will never be completely closed; on the other hand, for slender profiles, there exists a high enough value of the Mach number for which the shock front “reaches” the tip of the body and forms a Mach cone (Fig. 3.4) (Anderson Jr, 2010; Liepmann and Roshko, 1957). Normal (and close-to-normal) shock fronts are stronger discontinuities and compress the flow to subsonic conditions ($M_p < 1$); the flow then experiences further compression in the subsonic regime in its journey towards the body ($\xi_1 \rightarrow 0^+$). Moving away from the interface ($\xi_2 \neq 0$), the shock front curves, becomes oblique and progressively loses strength. Eventually,

as $x_2 = 0$ increases, the (oblique) shock reaches the critical point where it is not anymore able to compress the flow to subsonic conditions, and the flow downstream is faster than the local pressure wave speed ($M_p > 1$) (Fig. 3.4). In the limit of $\xi_2 \rightarrow \pm\infty$, the shock loses all its strength and the flow downstream it has the same, undisturbed conditions of that in front of it. In order to fully understand this construction, one must understand the theory of characteristics from solving the hyperbolic differential equations arising in supersonic flows from the Navier-Stokes equations of conservation (Anderson Jr, 2010; Liepmann and Roshko, 1957), whose description falls outside of the scope of the present manuscript. However, there are interesting similarities that can be drawn between gasdynamics and solid-mechanics. In a general medium, the speed of sound or pressure wave speed is equal to:

$$c_p = \sqrt{\frac{K_p}{\rho}} \quad (3.13)$$

where K_p is the coefficient of stiffness and ρ the density, which, in the assumption of incompressibility, is assumed to be constant. For an ideal gas undergoing isentropic transformations, $K_p = \gamma p$, where γ is the adiabatic index and p the pressure (Anderson Jr, 2010; Liepmann and Roshko, 1957); for a homogeneous solid in isentropic conditions, K_p corresponds to the P-wave (or longitudinal) modulus (Broberg, 1999; Freund, 1998; Needleman, 1999; Slepian, 2002), as shown in equation 3.1. Therefore, while in fluids the governing variable is the pressure, in viscoelastic solids it is the strain rate, upon which the elastic constants depend (see equation 3.1). From a general perspective, the two media qualitatively behave in a similar way. In fact, by considering a portion close to the $\xi_2 = 0$ plane, in the fluid case the pressure sharply increases through the shock front, and then gradually increases in the subsonic portion of the flow ($M_p < 1$) towards the body as ξ_1 approaches 0^+ (Anderson Jr, 2010; Liepmann

and Roshko, 1957); along the same path, the strain-rate magnitude sharply increase through the shock front and then it further, yet more gently, increases in the subsonic portion of the material ($M_p < 1$) towards the rupture tip, for $\xi_1 \rightarrow 0^+$ (Figs. 3.2, 3.3, 3.4 and 3.5). In the former case, the pressure variations are generated by the supersonic propagation of the body through the fluid; in the latter case, the strain-rate variations are induced by the rupture tip motion along the interface, which is also supersonic with respect of the LSR conditions of the undisturbed, bulk material ahead of it. Finally, as the pressure shock front curves (for $\xi_2 \neq 0$), its ability to compress the fluid flow rapidly decays to the point that the flow remains supersonic downstream it ($M_p > 1$) and the pressure level there is sensibly lower than that in the subsonic portion for $\xi_2 \approx 0$; analogously, in viscoelastic solids the strain rates rapidly diminish away from the rupture tip, to the point that the rupture tip is supersonic with respect to the pressure wave speeds arising downstream the curved portion of the shock front (Fig. 3.4). We speculate that the gap between the rupture tip and the pressure shock front is closely related to the cohesive zone. In fact, the cohesive zone is the area of influence of the rupture tip in its vicinity, in the process of weakening the molecular bonds by increasing the distance between atoms, which is intrinsically related to the generation of strains about the rupture tip over the microseconds time scale, ultimately leading to high strain rates. Simultaneously, the higher strain-rate region is what causes the shock front to detach from the tip of the rupture. In Figure 3.2, the magenta and black lines respectively represent the shear $\dot{\epsilon}_{12}$ and volumetric $\text{tr}(\dot{\epsilon})$ strain-rates profiles along the interface, normalized with respect to their peak value, while the green line represents the particle velocity in the x_1 -direction, \dot{u}_1 . By focusing on a small field of view (Fig. 3.5, insets) a higher spatial resolution about the central portion of the shock fronts is enabled, which allows a more precise observation of this distance, referred to as “process zone”, between them (Figs. 3.4 and 3.5, insets). The detachment

of the pressure shock front is related to the interaction of the pressure wavelets, propagating at the corresponding wave speed, with the variable strain-rate field in front of the rupture tip. In particular, in the HSR region, these wavelets outrun the rupture tip; however, the HSR region is characterized by decreasing strain rates in the positive ξ_1 -direction and therefore lower wave speeds. As a consequence, the pressure wavelets emitted by the rupture tip and propagating ahead of it decelerate due to the increasingly lower wave speeds that they encounter. The stable equilibrium condition is reached when their pressure wave speed matches that of the rupture: a perturbation further accelerating a wavelet would push it inside a lower strain-rate region and, due to that, the wavelets would slow down to speeds below that of the rupture, which would quickly reclose the gap. Conversely, a perturbation causing a wavelet to decelerate would result in the wavelet to be closer to the rupture tip and thus to encounter higher strain rates and accelerate away from it, back to the stable equilibrium condition where $c_p|_{\text{Mach Cone}} = V_r$. We must clarify that in the fracture dynamic community the term “inter-sonic” – or “supershear” – refers to cracks or ruptures propagating at speeds between that of the shear and pressure wavelets (Broberg, 1999; Freund, 1998; Needleman, 1999; Slepyan, 2002); in the fluid dynamic community, where no shear waves exist, the term “inter-sonic” refers to flows in the vicinity of the “sonic” conditions in the transition between the subsonic and supersonic regimes (Anderson Jr, 2010; Liepmann and Roshko, 1957). In this manuscript, we adopt the former nomenclature, in accordance to the fracture dynamic nature of its content. However, a subtler, yet fundamental distinction is that, while in the fracture dynamic community, speed regimes are related to the *local* value of the wave speeds at the crack tip, due to the interplay between the rupture tip energy release rate considerations and the admissible speed regimes (Broberg, 1999; Fineberg and Bouchbinder, 2015; Freund, 1998; Mello, Bhat, and Rosakis, 2016; Mello et al., 2010; Needleman, 1999; Rosakis, Xia, et al., 2007; Rubino,

Rosakis, and Lapusta, 2017; Slepyan, 2002), in the fluid mechanics community speed regimes are related to the *global* speed of the undisturbed, far-field flow. In order to understand the intersonic speed regimes *locally* arising at the rupture tip, it is natural to consider the former definition; however, in order to understand the formation of both sets of shock fronts, and in particular the pressure one, one needs to bear in mind the latter.

Shock Fronts Tracking Method

The angular variation along the shock fronts is evaluated through an algorithm that tracks the shock fronts in each frame of our measurement window. For this purpose, we define the shear and pressure shock fronts as the collection of peaks in the corresponding strain-rate fields: the maximum of the shear strain-rate field $\dot{\epsilon}_{12}$ (Fig. 3.2a and c; and Fig. 3.3a-c) is associated to the shear Mach cone, and the maximum of the volumetric strain-rate field $\text{tr}(\dot{\epsilon})$ (Fig. 3.2b and d; and Fig. 3.3d-f) is associated to the pressure shock front.

- The first step is to find the tip of the shock front along the interface, which is achieved by the following: (a) locating the coordinate corresponding to the maximum strain-rate value in the layer of pixels just above the interface; (b) repeating the same process to the layer just below the interface; and (c) averaging these two values.
- The second step involves the definition of the area of search around the tip of the shock front, which is represented by a circular sector centered at the shock-front tip and limited by two user-specified angles $\vartheta \in [\vartheta_1, \vartheta_2]$.
- Within this area of search, for each radius $r \in [r_1, r_2]$, the coordinate of the maximum value of the strain-rate is located. The combination of these

maxima recovers the shock front profiles, which are shown in Fig. 3.2 (blue line) and Fig. 3.3, $t = 51 \mu\text{s}$ after the rupture nucleation.

Once the shear (Fig. 3.2a) and the pressure (Fig. 3.2b) shock fronts have been tracked over multiple time frames, they are smoothed by using the moving average method (Fig. 3.2a and b, red lines; and Fig. 3.3 a and d). Due to the interaction of the pressure and shear signal nearby the rupture tip, it is more difficult to track the shock fronts, and in particular the pressure one, close to the interface ($x_2 = 0$). In addition, since the maximum inclination angle a shock front can assume is 90° (no shock front can exist otherwise), and the pressure shock front approaches this value at the interface ($x_2 = 0$), by applying the moving average smoothing method to a set of data bounded from above, tends to produce mildly lower outputs. For these reasons, the results for the pressure shock front shown in the following section are characterized by an inherently larger variability and bias when approaching the interface (Fig. 3.5a).

Deriving the Viscoelastic Material Properties from the Shock Fronts

In order to derive the inclination angles (Fig. 3.3b and e), each of the two shock front profiles in Figure 3.2a and b is differentiated with respect to the x_2 -direction. Simultaneously, the values of the strain-rate magnitude are obtained from the corresponding $|\dot{\epsilon}|$ fields (Fig. 3.2e and f; and Fig. 3.3c and f), so that each location along the shock fronts is associated with an angular value and a strain-rate one (Fig. 3.5a). For the sake of clarity, the color scheme has been selected to assign a black color to points proximal to front tip, gradually turning into green for points away from it. Both the pressure and the shear inclination angles increase with strain rates towards the tip of the respective front. The bow pressure shock front exhibits an angular evolution from 90° at the interface ($x_2 = 0$) to about 65° away from it (Fig. 3.3e and Fig. 3.5a), where the normal

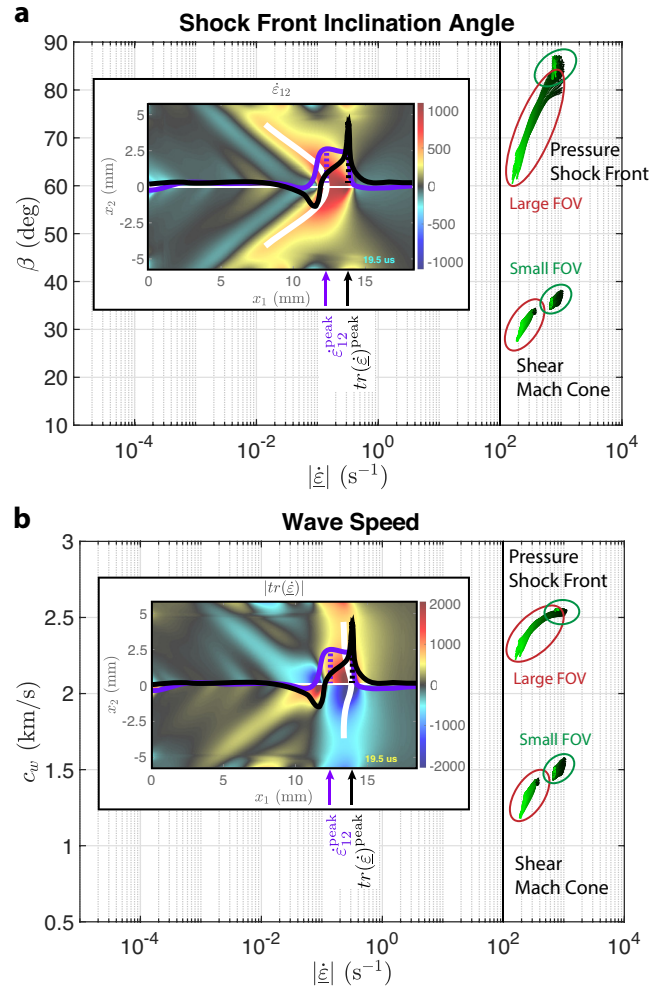


Figure 3.5: Strain-rate dependence of the shock fronts inclination angles **(a)** and the local pressure and shear wave speeds **(b)**. **(a)** The shock inclination angles are calculated by differentiating the shock fronts (Fig. 3.2, red lines) with respect to the x_2 -direction (Fig. 3.3b and e) and at each coordinate along the shock front the corresponding strain-rate values are obtained (Fig. 3.3c and f). From the values of the angles, **(b)** the shear and pressure wave speeds are computed using equations 3.11 and 3.12. Both profiles increase with strain rate and the pressure one appears to saturate for higher strain rate, corresponding to the shock front approaching the normal condition ($\beta_p \rightarrow 90^\circ$). The black dots, corresponding to points along the Mach cone in proximity to the rupture tip, gradually turn to green moving away from it, analogously to Figure 3.3. The two insets show the shear (top) and pressure (bottom) fields acquired via the DIC technique applied to a small field-of-view ($19 \times 12 \text{ mm}^2$). A thick white line is superimposed to the respective shock fronts to help with their visualization. The three traces represent the volumetric (black) and the shear strain rate (violet) along the interface. The location of their maxima has been included in order to highlight the gap between them, corresponding to the process zone (Fig. 3.4).

portion of the pressure shock front is associated with higher strain-rates, while the oblique portion is associated with milder ones (Fig. 3.3f and Fig. 3.5a). The shear Mach cone features smaller angles and smaller angular variations (Figs. 3.3b and 3.5a), in combination with lower strain rates (Figs. 3.3c and 3.5a). Small FOV measurements (Fig. 3.5a and b, insets) enable a higher spatial resolution about the tip of the shock fronts, which allow more precise estimates of the strain-rate levels and the associated angles in the HSR region (Fig. 3.5a). The combination of the rupture-speed measurement with equations 3.11 and 3.12 allows the conversion of the shock fronts inclination angles into the corresponding values of wave speeds under steady-state rupture propagation conditions (Fig. 3.5b). Interestingly, these results have been obtained with no assumption on the constitutive behavior of the material. In fact, only trigonometric considerations derived from the kinematic aspects of wavelets propagation (see section 3.3) under the assumption of isentropic solid (with the exception of the shock fronts) have been considered up to this point.

In the quasi-elastic solid approximation (Knauss and Zhu, 2002; Schapery, 1965) and steady-state rupture propagation conditions, the wave speeds are a function of the local material properties, which depend on the strain rates (see section on the Strain-Rate Dependence of the Wave Speeds), provided that the previous strain-rate history is uneventful. These assumptions carry some degree of approximation for the shear Mach cone due to the strain-rate history associated to the pressure shock front ahead of it (Fig. 3.2). Conversely, they can directly be applied to the pressure shock front due to the absence of strain-rate signals ahead of it (Fig. 3.2), and, from the knowledge of the wave speeds and the Poisson's ratio (assumed to be constant (Davies and Hunter, 1963; Mulliken and Boyce, 2006; Richeton, Ahzi, Vecchio, Jiang, and Makradi, 2007)), the Young's modulus can be computed as a function of the strain-rate magnitude, which in the plane strain approximation takes the form:

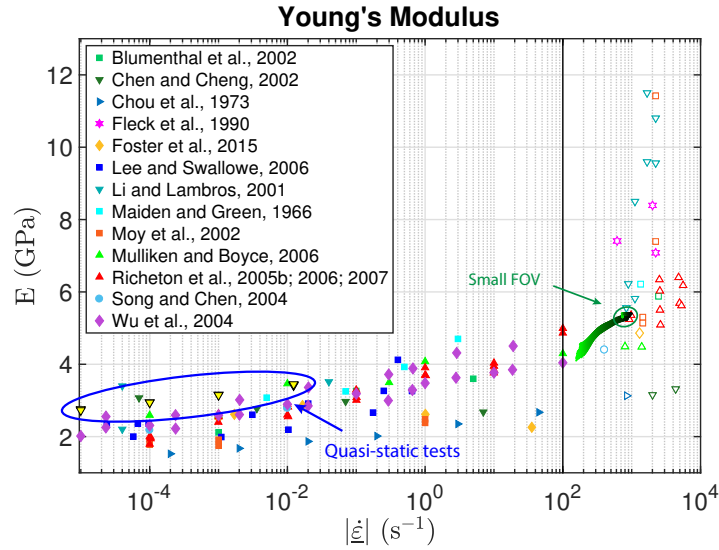


Figure 3.6: Young's modulus strain-rate dependence in PMMA. The Young's modulus in the dynamic region of strain rates has been obtained from the knowledge of the pressure wave speed (Fig. 3.5b) by using the linear-elastic wave relations in plane-strain conditions (see equation 3.14), assuming a density $\rho = 1180 \text{ kg/m}^3$ (measured) and a constant Poisson's ratio of 0.35 (Davies and Hunter, 1963; Mulliken and Boyce, 2006; Richeton, Ahzi, Vecchio, Jiang, and Makradi, 2007). The values in the low strain-rate range (yellow triangles), between 10^{-5} and 10^{-2} s^{-1} , have been obtained by performing a compression test on a PMMA cylinder and simultaneously measuring the vertical and hoop strains (see chapter 2, Fig. 2.8). These results are compared to those derived from the literature on PMMA, where the diamonds indicate tensile tests, the hexagons indicate shear tests, and all other symbols indicate compressive tests. The vertical solid black line separates the region of dynamic strain rates, where measurements are performed via SHPB experiments, from the one where servo-hydraulic compressive tests are capable of reaching the required strain-rate levels of interest.

$$E(|\dot{\epsilon}(\mathbf{x}(t))|) = c_p^2(|\dot{\epsilon}(\mathbf{x}(t))|)\rho \frac{(1 + \nu)(1 - 2\nu)}{(1 - \nu)} \quad (3.14)$$

Figure 3.6 shows that these results are in the range predicted by those obtained from the literature. The vertical black line at $|\dot{\epsilon}(\mathbf{x}(t))| = 10^2 \text{ s}^{-1}$ separates the low and intermediate strain-rate region from the dynamic regime where conventional testing frames are incapable to induce high-enough levels of strain rates and SHPB experiments become necessary (Chen, Lu, and Cheng, 2002; Chou, Robertson, and Rainey, 1973; Fleck, Stronge, and Liu, 1990; Foster et al., 2015; Li and

Lambros, 2001; Moy et al., 2003; Mulliken and Boyce, 2006; Richeton, Ahzi, Vecchio, Jiang, and Adharapurapu, 2006; Richeton, Ahzi, Vecchio, Jiang, and Makradi, 2007; Richeton, Schlatter, et al., 2005; Song and Chen, 2004) (Fig. 3.6). Another approach is to formulate models incorporating viscoelastic features and calibrating them by using quantities measurable via SHPB tests, such as the peak stress and then derive the material elastic constants (Chen, Lu, and Cheng, 2002; Chou, Robertson, and Rainey, 1973; Fleck, Stronge, and Liu, 1990; Foster et al., 2015; Li and Lambros, 2001; Moy et al., 2003; Mulliken and Boyce, 2006; Richeton, Ahzi, Vecchio, Jiang, and Adharapurapu, 2006; Richeton, Ahzi, Vecchio, Jiang, and Makradi, 2007; Richeton, Schlatter, et al., 2005; Song and Chen, 2004) (Fig. 3.6). Due to the intrinsic uncertainties of both these methods, the values for the Young's modulus in the dynamic region is characterized by a much larger jitter, if compared to the lower strain-rate counterpart (Fig. 3.6). For this reason, estimates of the Young's modulus in this region are indicated by empty symbols. Our measurements fall in the range drawn by those from the literature, exhibiting good agreement. Despite the value of the Young's modulus seem to saturate for strain rates beyond $7 \times 10^2 \text{ s}^{-1}$, this apparent behavior is likely related to the approximation of constant Poisson's ratio (Davies and Hunter, 1963; Mulliken and Boyce, 2006; Richeton, Ahzi, Vecchio, Jiang, and Makradi, 2007). In fact, if the Poisson's ratio is characterized by a decaying behavior with strain-rate magnitude (Lu, Zhang, and Knauss, 1997; Sane and Knauss, 2001; Tschoegl, Knauss, and Emri, 2002), the Young's modulus would exhibit an increasing tendency over the entire range of measurement of strain rates (see equation 3.14). For the sake of completeness, the quasi-static measurements we acquired using a servo-hydraulic testing frames between 10^{-5} and 10^{-2} s^{-1} are also included, which highlight the difference of the PMMA mesh we used in this study when compared to those from the literature.

The Young's modulus deviation from the linear behavior (in the logarithmic

scale of strain rates), concentrated at elevated strain rates (and room temperature), suggests the insurgence of an additional stiffening of PMMA in that range. A number of studies on polymers, including PMMA, have highlighted a substantial increase of other quantities (measurable via SHPB tests) in the dynamic range of strain rates, such as the yield stress or peak stress (Bauwens-Crowet, 1973; Chou, Robertson, and Rainey, 1973; Jordan et al., 2014; Mulliken and Boyce, 2006; Richeton, Ahzi, Vecchio, Jiang, and Adharapurapu, 2006; Rittel and Brill, 2008; Siviour, Walley, et al., 2005; Siviour and Jordan, 2016; Walley and Field, 1994). However, the methodology described in this manuscript enriches the SHPB results by allowing the quantification of other material properties, such as the pressure and shear wave speeds (under only kinematic assumption), and the Young's modulus (assuming a quasi-elastic material behavior and constant Poisson's ratio). The knowledge of these material constants in the dynamic range of strain rates can foster progress in the design of lightweight structures required to withstand dynamic loads. Although we performed our tests on PMMA, we do not foresee any limitations in applying this technique to other materials. In addition, although our results have taken advantage of spontaneously propagating ruptures, externally driven ones can be equally effective, provided that the driving signal propagate at speeds beyond the pressure wave speed of the undisturbed, bulk material so that both sets of shock fronts are present. Finally, we do not anticipate any limitation, aside of those related to an increased complexity of the experimental setup, in applying this technique to higher-temperature tests.

3.4 Conclusions

Dynamic shear rupture experiments have been performed on PMMA samples and the ultra-high-speed digital image correlation was employed to produce velocity and strain-rate fields. The shock fronts have been tracked and the direct

dependence of their inclination angle on the strain-rate magnitude explored. In order to convert the inclination angles into wave speeds, the validity of the trigonometric relationship between the inclination angle and wave speed has been proven for curved shock fronts scenarios in non-homogeneous media, provided that **(a)** both the values of angle and wave speed refer to the same local coordinate along the shock front, and **(b)** the rupture tip is propagating in steady-state conditions. It is worth of notice that, in the presence of shock fronts, only kinematic assumptions are needed to calculate the wave speeds of the material in the dynamic range of strain rates. In the assumption of quasi-elastic solid, the Young's modulus has been computed as a function of strain-rate magnitude from the knowledge of the pressure wave speed, where a constant Poisson's ratio of 0.35 has been considered (Davies and Hunter, 1963; Mulliken and Boyce, 2006; Richeton, Ahzi, Vecchio, Jiang, and Makradi, 2007). Due to the difficulty of measuring the material properties at high strain rates (Siviour and Jordan, 2016), the time-temperature superposition principle is commonly invoked for polymers to indirectly extrapolate the properties to strain-rate values beyond the measured ones, with the limitation that the accuracy (or even validity) of this method has not been confirmed in the presence of β -transition in the glassy domain and even in the rubbery domain, its applicability needs to be assessed on a case-by-case investigation (Capodagli and Lakes, 2008; Lakes, 2004; Li, 2000; Plazek, 1996; Sane and Knauss, 2001; Tschoegl, Knauss, and Emri, 2002; Van Gorp and Palmen, 1998). Split-Hopkinson Pressure Bar tests can be employed to explore strain rates comparable to our regime, yet they cannot accurately quantify the material properties (Gama, Lopatnikov, and Gillespie, 2004), due to the inability to attain strain-rate equilibrium conditions during the transient loading. For these reasons, the experimental technique we present here, represents an alternative method to quantify the wave speeds as well as the Young's modulus in viscoelastic solids in the dynamic regime of strain rates, provided that the rupture tip exceeds

the LSR pressure wave speed of the undisturbed, bulk material ($V_r > c_p^{\text{LSR}}$), so that both the shear and the pressure shock fronts are present. En passant, we notice that, although our ruptures are spontaneous, in general, this is not a requirement and they can be driven by an external dynamic load. Future work shall be concentrated on the exploration of the applicability of the quasi-elastic solid approximation to the shear Mach cone, despite the non-zero strain-rate history associated to the presence of the pressure shock front ahead of it. Should the applicability be confirmed, under reasonable assumptions, then, from the knowledge of both the shear and pressure wave speeds, all the material properties of the polymer under investigation can be derived, starting from the Poisson's ratio, which is a function of the pressure-to-shear wave-speed ratio only. We conclude by noting that it may be helpful to perform this investigation to shear Mach cones arising from intersonic ruptures, where $c_s^{\text{LSR}} < V_r < c_p^{\text{LSR}}$, in order to avoid the presence of pressure shock fronts and have smoother and smaller dilatational and compressional signals and consequent strain-rate histories instead, which could potentially reduce the inaccuracy associated with its neglect in the quasi-elastic solid approximation.

3.A Rupture propagation regimes through materials characterized by different wave speeds

Figure 3.7 shows four configurations of material properties for the rupture to propagate into. (a) represents a supersonic rupture propagation in a viscoelastic solid, highlighted by the presence of both shock fronts. In particular, at $x_2 = 0$ the pressure wavelets outrun the rupture tip in the HSR region ahead of it. In this region, the strain rates are monotonically decreasing and the pressure wavelets decelerate, as shown in the x_1-t -diagram, until they coalesce when their speed equals that of the rupture tip behind. (b) is an equivalent case in which the ratio between the rupture speed and that of the shear wavelets is kept the same, yet the pressure wave speed of the material is higher so that the rupture tip is now subsonic with respect to the LSR pressure wave speed. As a result, at $x_2 = 0$ the pressure wavelets outrun the rupture tip in the HSR region and slow-down in the LSR region further ahead, reducing the spatial distance among each other. However, since the rupture speed is slower than the LSR pressure wavelets, they never reach the conditions of coalescence and keep “escaping” the rupture tip. (c) is an equivalent case in an isotropic linear elastic solid, characterized by material properties equal to the HSR ones of the previous case (b). In this case, only one shear and one pressure wave speed exist and the wavelets propagate at a constant speed, preserving the circular symmetry. As a consequence, the shear Mach cone is characterized by a constant inclination angle. A pressure shock front cannot exist, since spontaneously propagating ruptures cannot exceed the pressure wave speed in linear-elastic solids. Analogously, (d) is an equivalent case to (c), yet where the material properties correspond to the LSR ones. The rupture tip cannot reach or exceed the pressure wave speed of the material; however, it propagates at speeds closer to it and therefore the pressure wavelets ahead of the tip are more clustered, yet never forming a pressure shock front. As a consequence of the

higher ratio between the rupture speed and that of the shear wavelets, the shear Mach cone exhibits a steeper inclination angle than the previous case (c).

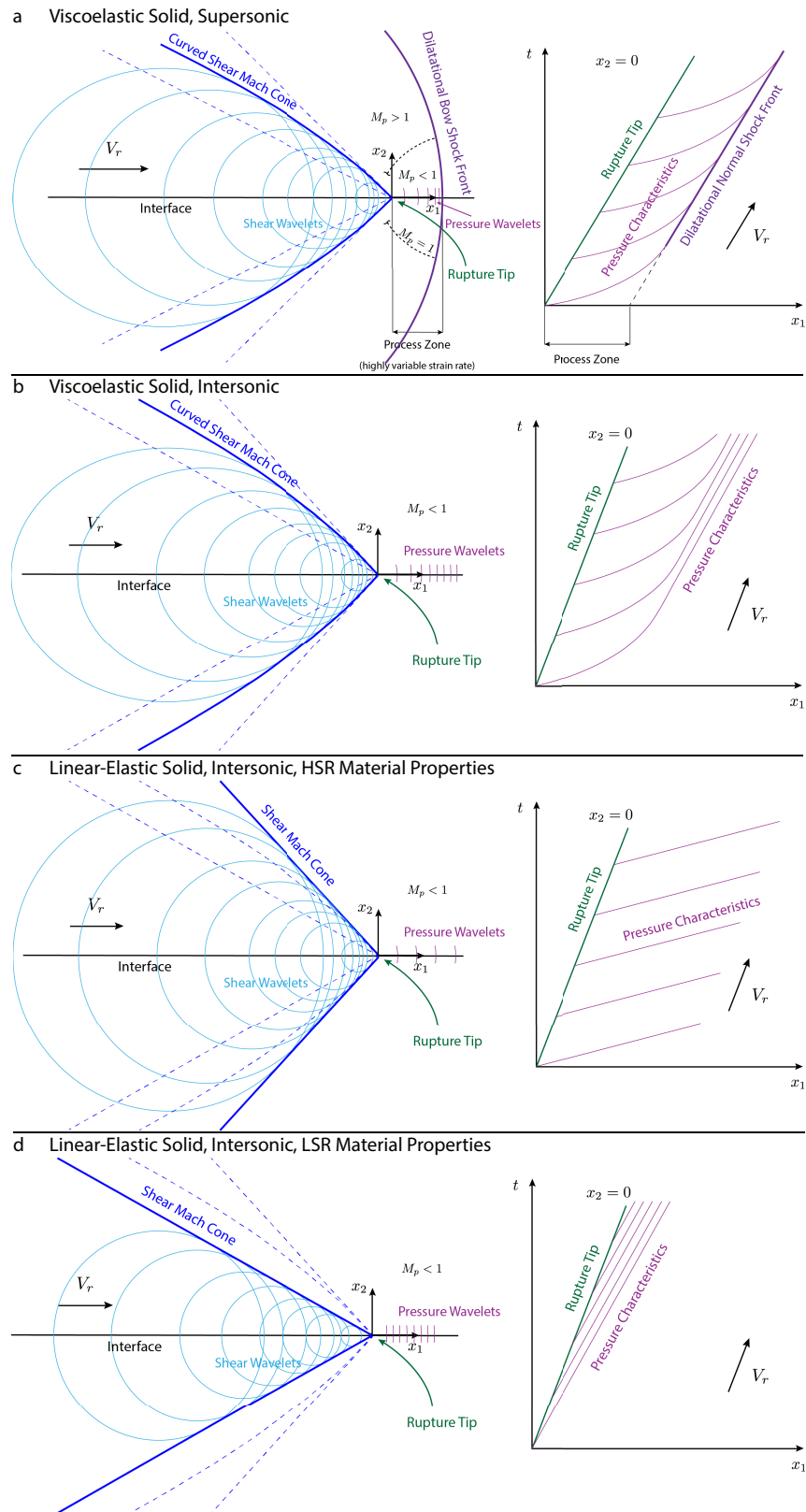


Figure 3.7: Schematics of the shear and pressure shock fronts in different materials and rupture regimes.

Part II

Shear ruptures due to fluid injection

CHAPTER 4

Triggering fault slip by fluid injection: effect on slip stability and dynamic rupture properties

4.1 Introduction

Fluid overpressure is recognized to play a fundamental role in promoting fault motion. The close connection between fluids and faulting has been revealed by a large number of observations, both in natural events and in earthquakes induced by human activities, such as wastewater disposal associated with oil and gas extraction (Ake et al., 2005; Cappa, Guglielmi, et al., 2005; Cappa and Rutqvist, 2012; Dahm, Hainzl, and Fischer, 2010; Ellsworth, 2013; Frohlich, 2012; Gan and Frohlich, 2013; Guglielmi et al., 2015; Keranen et al., 2014; McGarr et al., 2015; Segall, Rubin, et al., 2010; Wei et al., 2015). Fluid-induced slip behavior can range from earthquakes to slow, creeping motion. It has been long thought that creeping and seismogenic fault zones have little to no

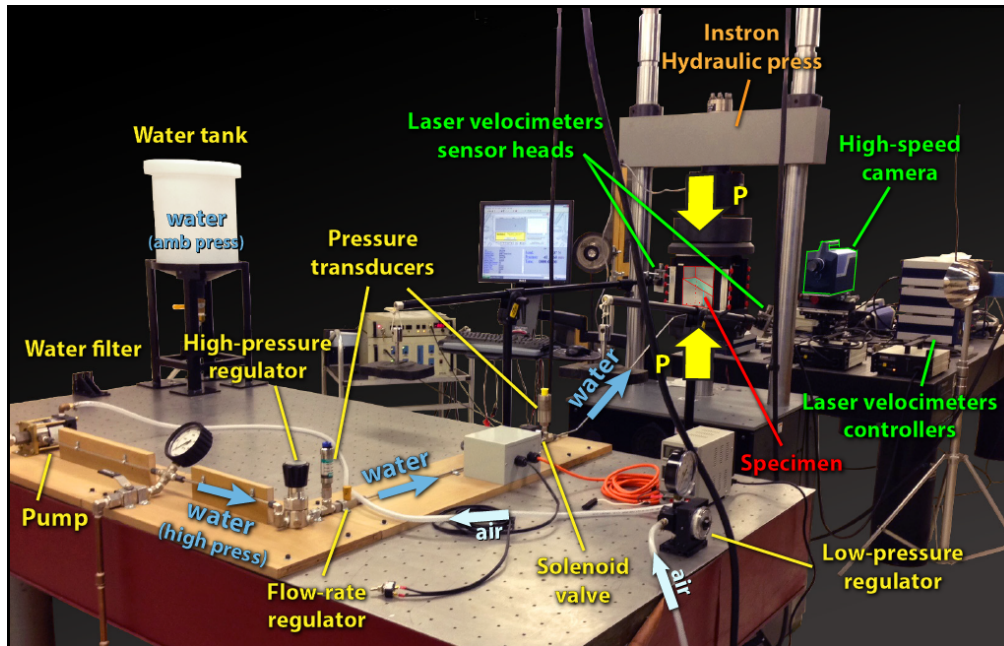


Figure 4.1: Laboratory setup featuring a fluid-injection circuit capable of delivering pressurized fluid to the specimen’s fault and trigger laboratory-scale earthquakes. The sample has been cut into two identical halves joined together to form an interface that mimics a crustal fault pre-stressed in compression and shear. This setup possesses the capability to control the rate of injection, the fluid pressure and its temporal rate of increase. The diagnostics consists of a high-speed camera, laser velocimeters (only one is used in this study), strain gages (not shown in the Figure), and two cameras, one for measurements of creep (not shown in the Figure), and one for tracking the fluid front as it propagates over the interface prior the dynamic rupture nucleation (not shown in the Figure).

spatial overlap. Nonetheless, growing evidence suggests that the same fault areas can exhibit both slow and dynamic slip (Beroza and Ide, 2011; Chen and Lapusta, 2009; Dragert, Wang, and James, 2001; Noda and Lapusta, 2013; Peng and Gomberg, 2010). In seismogenic zones, the existence of large-scale slow slip has been proposed by a number of studies investigating the physics of foreshocks (Bouchon, Durand, et al., 2013; Brodsky and Lay, 2014; Kato, 2012) and the presence of transient slow slip occurrences in subduction zones (Beroza and Ide, 2011; Dragert, Wang, and James, 2001). Incorporating in physics-based models the simultaneous ability of fault zones to slip both slowly and seismically

has fostered a deeper understanding of key features of large-scale events, such as the propagation of large earthquakes in creeping segments, the observation of high-frequency content in slow slip sections, and the cumulative stress drop released by the synergy of slow and dynamic events (Chen and Lapusta, 2009; Cubas et al., 2015; Noda and Lapusta, 2013). The interaction of fluid-related effects with the rate-and-state frictional properties is responsible for such complex fault behavior. Dehydration reactions within or below natural faults (particularly subduction zones) (De Paola et al., 2007; Di Toro et al., 2011; Dobson, Meredith, and Boon, 2002; Jung, Green Ii, and Dobrzhinetskaya, 2004; Miller et al., 2004; Okazaki and Hirth, 2016) and fluid injection into the subsurface (Ake et al., 2005; Cappa, Guglielmi, et al., 2005; Cappa and Rutqvist, 2012; Dahm, Hainzl, and Fischer, 2010; Ellsworth, 2013; Frohlich, 2012; Gan and Frohlich, 2013; Guglielmi et al., 2015; Keranen et al., 2014; McGarr et al., 2015; Segall, Rubin, et al., 2010; Wei et al., 2015) are two mechanisms responsible for increasing the pore pressure p .

The shear resistance τ_{res} is typically described by the Amontons-Coulomb friction model which linearly relates it via a friction coefficient f with the effective normal stress $\hat{\sigma}_n$ acting on a fault:

$$\tau_{\text{res}} = f\hat{\sigma}_n \quad (4.1)$$

where $\hat{\sigma}_n = \sigma_n - p$. The pore pressure p competes with the fault normal stress σ_n and reduces the fault frictional resistance, promoting the insurgence of slip. However, such slip may be stable (slow) or unstable (seismic). Simultaneously, the critical length scale h^* for a crack to energetically (dynamically) self-sustain its growth in steady-state slipping conditions (Rice and Ruina, 1983; Rice, Lapusta, and Ranjith, 2001) or quasi-static ones (Liu and Lapusta, 2008; Rubin and Ampuero, 2005; Uenishi and Rice, 2003) is inversely proportional to the effective

normal stress. The general form for the 2D theoretical estimate of the critical crack size, h^* , on a rate-and-state fault with steady-state velocity-weakening friction is given by $h^* = (\mu^* L)/[F(a, b)(\sigma_n - p)]$, where $\mu^* = \mu/(1 - \nu)$ for modes I and II, and $\mu^* = \mu$ for mode III (Uenishi and Rice, 2003), L is the characteristic slip distance, and $F(a, b)$ is a function of the rate-and-state friction parameters a and b , which assumes the form of $F_{RR}(a, b) = 4(b - a)/\pi$ (Rice and Ruina, 1983, eqn. (40)), or $F_{RA}(a, b) = [\pi(b - a)^2]/2b$, with $a/b > 1/2$ and quasi-static crack propagation (Rubin and Ampuero, 2005, eqn. (42)). This function, for a fault in a 3D elastic medium in quasi-static slip conditions, needs to include an extra factor: $F_{CL}(a, b) = (\pi^2/4)F_{RA}(a, b)$ (Chen and Lapusta, 2009). As a consequence, an increase in pore pressure induces a reduction in the effective normal stress, which, in turn, increases the critical length scale h^* , promoting a stable slow (aseismic) slip. Indeed, recent field observations have proposed that fluid injection can actually trigger slow slip (Cappa and Rutqvist, 2012; Guglielmi et al., 2015; Wei et al., 2015).

However, the understanding of the dependence of the fault response on the rate of pore pressure increase still remains elusive. Efficient shear-heating-induced thermal pressurization (TP) of pore fluids has been shown to become important late in the nucleation phase, well before detectable seismic waves are radiated away from the fault, and to ultimately reduce the nucleation size (Segall and Rice, 2006). However, despite the smaller nucleation size in patches with more efficient TP, earthquakes tend to be nucleated in patches with less efficient TP due to their higher interseismic shear stress (Noda and Lapusta, 2010). More efficient TP patches experience larger stress drop and coseismic slip, yet they do not rupture at every event due to the lower interseismic stress. The slip deficit on the less efficient TP patch is compensated by more frequent smaller events.

To summarize, the complex interplay between fluids and the initiation of

seismic or aseismic slip is an open research topic with paramount implications for hazard mitigation, given the abundance of faults permeated with fluid due to natural or human-induced activities in proximity of populated areas.

In this study, two nucleation techniques are investigated: **(a)** a gentle fluid-pressure ramp-up; and **(b)** a sharp one. We show that, in cases of rapid increase in pore pressure, both the steady-state and quasi-static assumptions fail, and unstable slip is promoted for rupture lengths considerably smaller than the critical ones predicted by the theoretical estimates (Chen and Lapusta, 2009; Liu and Lapusta, 2008; Rice and Ruina, 1983; Rice, Lapusta, and Ranjith, 2001; Rubin and Ampuero, 2005; Uenishi and Rice, 2003). Considerably less fluid is delivered into the fault prior to the nucleation of seismic events, if compared to the gradual pore pressure increase scenarios, and dynamic slip is triggered at much lower levels of pressure. We also experimentally observe an intermediate phase of accelerated slip prior to the initiation of the dynamic rupture, which redistributes the stress over the interface. In cases of rapid pore pressure increase, the stress redistribution is much more dramatic close to the injection location, yet does not propagate all the way to the surface where the measurement stations are located, jeopardizing the ability of anticipating the subsequent dynamic event, which, once initiated, produces effects comparable to the ones arising by the adoption of the slow nucleation protocol.

4.2 Fluid-Injection Experimental Setup

Specimen Configuration and Fluid-Injection Setup

In order to investigate the effects of fluids on the frictional faulting, a hydraulic setup was designed to inject pressurized water onto the interface of a Poly(Methyl Meth-Acrylate) (PMMA) specimen (Figs. 4.1 and 4.2). The specimen is a $200 \times 250 \times 12.5 \text{ mm}^3$ PMMA prism divided into two identical

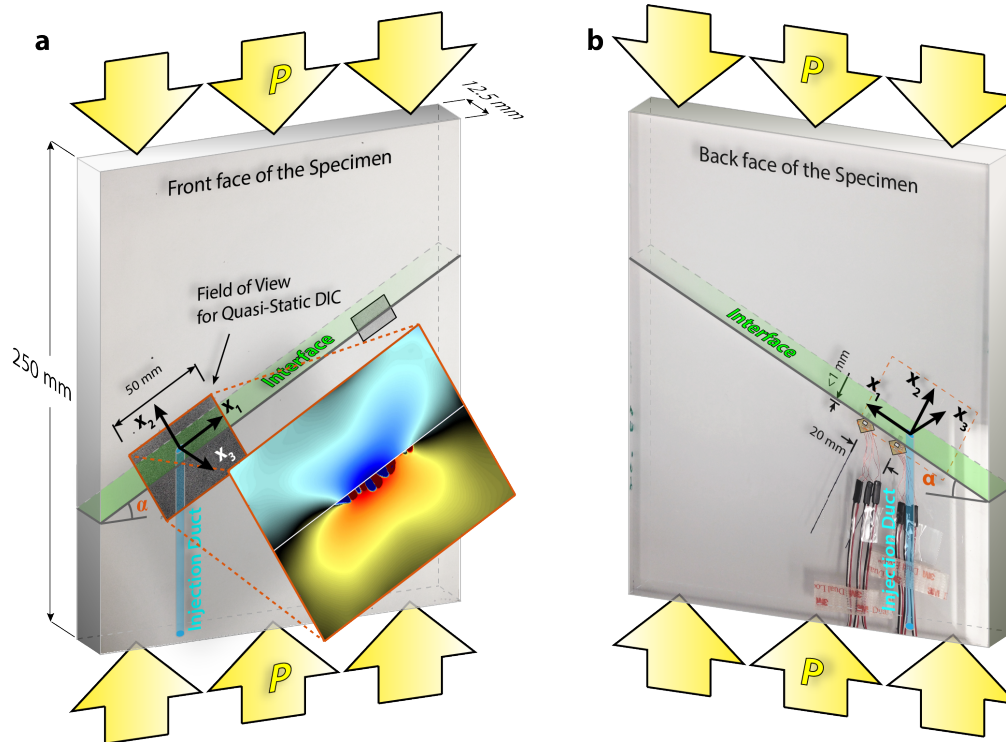


Figure 4.2: Specimen setup front and back side views. A $250 \times 200 \times 12.5\text{-mm}^3$ PMMA sample is separated into two halves by an oblique interface (green-shaded area) at an angle $\alpha = 29^\circ$, and is preloaded by a vertical component $P = 15\text{ MPa}$ (yellow arrows). A thin duct of 1-mm diameter enables the injection of pressurized fluid directly onto the interface. (a) On the front side, a pattern of random black dots is painted over a flat white background in a region of $50 \times 40\text{ mm}^2$ in order to allow displacement measurements through the DIC technique. The temporal derivative of the displacement fields produces velocity fields, of which the horizontal component \dot{u}_1 is shown in the inset during a foreshock event (Fig. 4.14). (b) On the back side, two strain rosettes are glued just below the interface and 20 mm from each other, which are each capable of measuring three strain tensorial components, separated by 45° angles. These components can be converted into the strains along the fault ε_{11} , normal to it ε_{22} , and the shear one ε_{12} .

halves by an oblique cut at an angle α with respect to the 200-mm dimension (Fig. 4.2). The juxtaposition of these two halves creates an interface (green-shaded area), whose surfaces have been polished and bead-blasted to obtain desired and repeatable tribological conditions (Mello et al., 2010). The setup allows us to achieve a wide range of water peak pressure, flow rate, pressure rise-time, and duration of pressure plateau. After the pressurization by the pump, the water pressure is modulated by a manual regulator and its flow rate by a needle valve (Figs. 4.2 and 4.4). The pressure regulator allows a wide range of rising times, spanning from few MPa per hour to few MPa per second. A solenoid valve, characterized by a rapid opening time, is employed to produce sharper rising times of the order of few MPa per tens of milliseconds, which would otherwise be impossible to replicate with the manual pressure regulator. In a zero-time-to-open approximation, the valve mimics a theoretical diaphragm separating a fluid at different pressure levels on either side. The sudden disappearance (opening) of such diaphragm gives rise to a Riemann problem (Liepmann and Roshko, 1957; Roe, 1981) in which a shock wave travels downstream of the pipe followed by a (slower) contact discontinuity, while an expansion fan travels upstream. The solenoid valve, which is actuated via a small electrical circuit, allows the creation of much sharper pressure ramp-up signals to be delivered to the specimen's interface (Figs. 4.2 and 4.4). Two pressure transducers are located on either side of the solenoid valve in order to simultaneously measure the pressure upstream and downstream of it, regardless of the open or close configuration of the valve. These transducers are characterized by a cut-off frequency of 5 Hz and 3 kHz, respectively. For the sake of clarity, the same color scheme associated with each of the two pressure transducers in Figure 4.4b will be consistently adopted in the plots throughout this manuscript: purple refers to the pressure measured upstream of the solenoid valve and blue to the pressure downstream of it. The pressure value measured downstream of the valve is delivered to the specimen's

interface (Fig. 4.4b). At the ambient pressure and temperature, the speed of sound in water is approximately 1.5 km/s. In order to achieve pressure equilibrium over a 2-meter-long pipe, 5 ms are needed for 3 – 4 wave reverberations to occur. Considering that the shortest time scale in the injection circuit is that of the opening of the solenoid valve, which is in the order of tens of milliseconds, assuming pressure equilibrium between the pressure transducer downstream of the valve and the injection location on the specimen's interface is not a bad approximation.

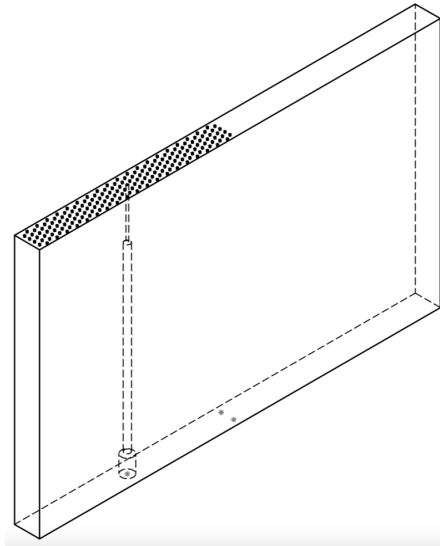


Figure 4.3: Drawing of the bottom half of the specimen, divided by a cut at an angle $\alpha = 0^\circ$. Over the interface a constellation of holes 0.5-mm in both diameter and depth allows the measurement of the pore pressure as the water fills them and the local pressure is increased.

Diagnostics

Local and Global Pressure Measurements

The pressure transducers provide a well-resolved temporal history in correspondence to the duct, however, they cannot quantify the pressure at other locations on the interface as the fluid diffuses over it. In order to measure the

pressure distribution over the interface, a specimen with a cut at an angle of $\alpha = 0^\circ$ is employed in order to avoid sliding and is loaded up to the resolved normal stress of the corresponding $\alpha = 29^\circ$ case, i.e., $P = 15 \cos^2(29^\circ) = 11.5$ MPa. A population of holes 0.5 mm in both diameter and depth are drilled on the bottom half interface (Fig. 4.3), so that, upon the juxtaposition of the two halves of the specimen, there is no surface contact in correspondence to each hole, and a small volume of air at ambient pressure ($p_{\text{amb}} \approx 0.1$ MPa) is trapped there. On the interface between the two halves of the specimen a 0.5-mm thick Fujifilm Prescale[®] tactile pressure-indicating sensor film is placed, which locally and irreversibly changes color in proportion to the amount of pressure it experiences. Its range of measurement spans between 2.4 and 9.7 MPa, with a spatial resolution of $5 \div 15 \mu\text{m}$, and an accuracy of $\pm 2\%$ (data provided by the manufacturer). For this reason, measured pressure values smaller than or equal to 2.4 MPa have been manually set to be equal to the ambient pressure. After the specimen is loaded to the desired level, the pressure film experiences the resolved normal stress ($P = 11.5$ MPa) in correspondence to the areas of contact. This stress level exceeds the upper bound of the pressure measurement range of the film (9.7 MPa), which thus chromatically saturates (Fig. 4.6). However, in the locations of the 0.5-mm holes, there is no contact and the pressure is equal to the ambient one ($p_{\text{amb}} \approx 0.1$ MPa). As a consequence, the film does not assume any coloration in correspondence to the holes.

As the water escapes from the injection location, driven by the high pressure gradient, it fills the holes and increases the pressure level inside them. This increase is picked up by the film, which assumes a coloration in proportion to the local-hole pressure level. In summary, the pressure measured by the film in correspondence to the population of holes is representative of the spatial distribution over the interface.

Full-field Imaging and Digital Image Correlation

In order to quantify both the slow slip δ and its rate $\dot{\delta}$ in the absence of pressurized fluid, on the front side of the specimen (Fig. 4.2a), a thin layer of white paint is deposited and a $50 \times 40 \text{ mm}^2$ random pattern of optimally-sized black dots is added on top of it, symmetrically with respect to the injection location and the fault. Images are acquired via a 2448×2050 pixel EO-5023M camera at 2 frames per minute, allowing displacement measurements via digital image correlation (DIC) (Sutton, Orteu, and Schreier, 2009) over a $45 \times 38 \text{ mm}^2$ field of view (FOV). The images are then filtered by means of non-local (NL) de-noising algorithms (Buades, Coll, and Morel, 2008; Rubino, Rosakis, and Lapusta, 2017) and numerically differentiated with respect to time in order to obtain velocity fields (see chapters 2 and 3). At the laboratory scale, displacements during creeping motion are well below the micron scale. Having 2448 pixels over a 45-mm long field of view corresponds to about $20 \mu\text{m}/\text{px}$. The accuracy of DIC algorithms with optimally chosen interpolating functions can reach $1/200$ of a pixel (Sutton, Orteu, and Schreier, 2009) and therefore $0.1 \mu\text{m}$, which, theoretically, fall in this range. However, a number of sources of noise can generate random vibrations well above the micron scale. In order to counteract these influences, for each frame, five images are collected at a rate of 3 per second and averaged among themselves, and a relatively large subset of $101 \times 101 \text{ pixel}^2$ is adopted to smoothen out the solution from the DIC technique (*ibid.*). The slip δ is computed as the difference of the fault-parallel displacement u_1 on either side of the interface, $\delta = |u_1^+ - u_1^-|$. Assuming the slip to be homogeneous during the slow-slip phase in the absence of pressurized fluid, all the displacement values below the interface can be averaged among themselves \bar{u}_1^- and then subtracted from the averaged ones above it \bar{u}_1^+ , in order to obtain, for each frame, a single value of averaged slip $\bar{\delta}$ and slip rate $\dot{\bar{\delta}}$.

All the results presented in this manuscript are with respect to the reference frame aligned with the inclined interface, where the x_1 -direction is along the fault plane, the x_2 -direction is normal to it (Figs. 4.2a and 4.4a) and the x_3 -direction is out-of-plane.

Strain Measurement System

On the back side of the specimen (Figs. 4.2b and 4.4a), two strain gages are placed just below the interface: one in proximity to the injection location (SG-0) and the other one 20 mm away from it (SG-20). They are connected to a high-speed acquisition system capable of collecting data (at a reduced sampling rate) over several minutes and also resolving the microsecond time scale once a triggering signal is received. Using this technique, strain signals are acquired at temporal scales spanning over nine orders of magnitude. Linear-elastic constitutive relationships are adopted to convert strains into stresses, where, given the viscoelastic nature of PMMA, low-strain-rate (LSR) material properties are used for the measurements acquired prior to the dynamic rupture, while high-strain-rate (HSR) material properties are employed otherwise (Chapter 2 and 3). Adjacent to the SG-0, just above the interface, a retro-reflective tape is used to mirror the laser beam from a vibrometer and provide a triggering signal as soon as the nucleation of the dynamic event occurs.

Upon the application of an external load P (Fig. 4.2, yellow arrows) of 15 MPa, the interface experiences a resolved normal and shear stress of $P \cos^2(\alpha)$ and $P \sin(\alpha) \cos(\alpha)$, respectively. Note that the load P is kept constant by setting the loading frame in the load-control mode.

Under these conditions, the pressurized fluid is introduced onto the interface through a 1-mm-diameter duct (Figs. 4.2 and 4.4a, blue channel). A Buna-N rubber o-ring, placed at the bottom of the specimen, guarantees the seal from

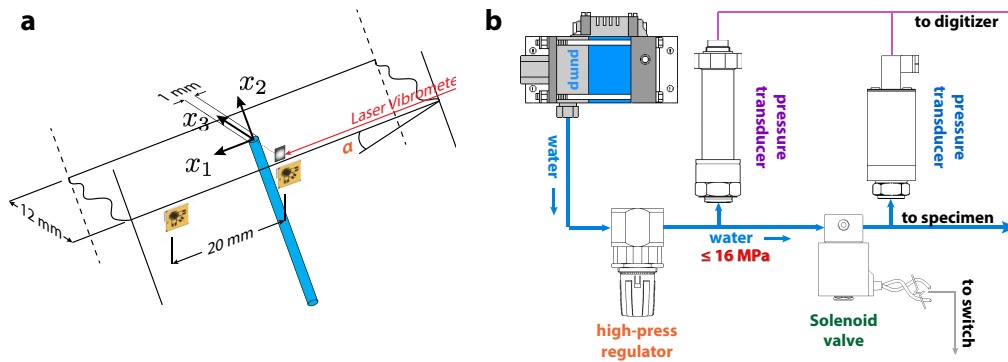


Figure 4.4: Fluid-injection setup. (a) Close-up view of the interface of the specimen about the injection location, on the back side where the strain gages are placed (Fig. 4.2b). The laser vibrometer signal is used to detect dynamic motion in the x_1 -direction associated with the laboratory-scale seismic event and trigger the acquisition of the strain gage signals at high-bandwidth (1 MHz). (b) The water, after being pressurized by the pump, crosses a series of components: a high-pressure regulator for manual pressure modulation in the range of few MPa over several minutes to few MPa per second; a pressure transducer for pressure readings upstream of the solenoid valve; a solenoid valve activated by a switch, allowing sharp pressure ramp-up profiles in the order of few MPa per hundred milliseconds; and another pressure transducer downstream with bandwidth capability of 3 kHz. This second transducers measures the fluid pressure just upstream of the duct prior to its delivery to the interface.

water spills, however, it adds a small thickness that is reduced as the specimen is compressed by the loading frame. This reduction in volume tends to squeeze a small quantity of fluid onto the interface. For this reason, a 1-cm-long layer of (compressible) air, approximately corresponding to $3.1 \times 10^{-8} \text{ m}^3$, is left on top of the fluid meniscus prior to starting the loading phase. After the desired far-field load is reached and the absence of liquid on the interface is confirmed, the fluid pressurization phase can begin.

PMMA vs. Natural Rock

One important advantage of using PMMA as the analog material is its reduced shear modulus ($\mu_{\text{PMMA}} \approx 1.2 \text{ GPa}$) compared to that of rocks ($\mu_{\text{Rock}} \approx 30 \text{ GPa}$). Since characteristic rupture length scales, such as the critical sizes previously mentioned, are proportional to the shear modulus of the host material,

ruptures propagating within the bulk of the specimen have characteristic rupture length scales smaller than rocks by a factor of $\mu_{\text{rock}}/\mu_{\text{PMMA}} \approx 25$, under the assumption of similar frictional properties. Indeed, the critical crack size falls in the range of few centimeters for the set of experimental conditions that we explore, allowing the flexibility to nucleate dynamic ruptures and letting them spontaneously develop within the 200-mm sample size (Lu, Lapusta, and Rosakis, 2009). For this reason, our laboratory experiments with PMMA offer a unique opportunity to study, in real time, rupture features that would otherwise be impossible to reproduce and observe on manageable samples made of natural rock material (Beeler et al., 2012; Dieterich, 1981; McLaskey and Kilgore, 2013; McLaskey, Kilgore, et al., 2014; Okubo and Dieterich, 1984).

4.3 Results and Discussion

Pressure Measurements: Slow vs. Fast Injection

Two fluid-induced seismic-initiation protocols are investigated: (a) a gentle pressure build-up until a dynamic rupture spontaneously occurs (Fig. 4.5a); and (b) an abrupt pressure build-up, where a sharp pressure profile is induced by the sudden opening of the solenoid valve (Fig. 4.5b). For consistency, in the latter case, the pressure upstream of the solenoid valve – prior to its opening – is set to the same level as that at which the rupture spontaneously nucleated in the slow opening counterpart. In addition, the same specimen is used to perform the experiments in both cases.

Throughout this chapter, the time of initiation of the dynamic event is set to be equal to zero. Thus, negative values of time indicate events prior to the triggering of the dynamic rupture. All tests have been performed on specimens at an angle of 29° and vertically loaded at 15 MPa (Fig. 4.2), resulting in a resolved normal and shear stresses of 11.5 and 6.4 MPa, respectively.

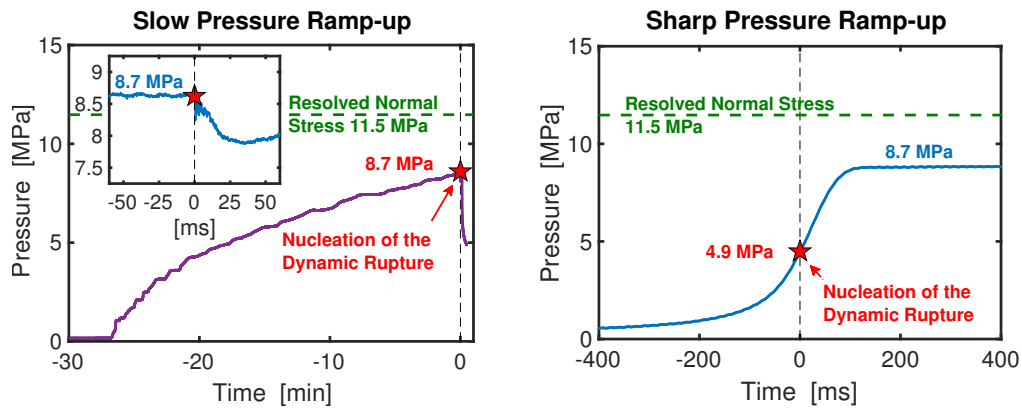


Figure 4.5: Pressure ramp-up profiles. Two protocols are employed to deliver pressurized fluid onto the interface of the specimen: (left) a slow pressure ramp-up over 27 minutes; and (right) a rapid one over few hundred of milliseconds, achieved via the quick opening of the solenoid valve. For the sake of clarity, the color code of the pressure data mimics that of the labels of the pressure transducers in Figure 4.4b: purple for upstream of the valve and blue for downstream. The red star indicates the triggering of the dynamic rupture recorded by the laser velocimeter (Fig. 4.4a), which is set at the origin of our temporal scale. The green dashed line represents the resolved normal stress $\sigma_n = P \cos^2(\alpha)$ the fluid pressure is competing with.

In the first scenario (Fig. 4.5a), the pressure is gradually increased from the ambient level (about 0.1 MPa) until the insurgence of the dynamic rupture (red star) at 8.7 MPa (76% of the resolved normal stress). With an average rate of 5.3×10^{-3} MPa/s, it takes approximately 27 minutes to reach the conditions for rupture initiation. The pressure transducer downstream of the solenoid valve (Figs. 4.1 and 4.4b) allows a higher temporal resolution (Fig. 4.5a, inset). Its measurement exhibits a marked pressure reduction over few tens of millisecond after the rupture initiation and is characterized by an initial brief oscillatory period. The pressure behavior after the nucleation of the dynamic rupture is influenced by four phenomena: (a) the increase of porosity due to slip-induced dilation (Marone, Raleigh, and Scholz, 1990; Segall and Rice, 1995); (b) the pressure waves' reverberations through the circuit pipes between the pump and the specimen's surface in the attempt to achieve pressure equilibrium; (c) the inability of the loading frame to keep the load constant after the rupture, due to

its reaction time several orders of magnitude slower than the characteristic times of the dynamic slip event; and **(d)** the fluid pump attempting to re-pressurize the circuit after a pressure loss is detected. While the pressure reduction due to dilation is related to the initial phases of the insurgence of the slip and is thus intrinsically characterized by time scales in the order of $10^0 \div 10^1 \mu s$, which are well below the pressure transducer temporal resolution, all other phenomena live in the milliseconds time scale. In particular, the initial oscillations (Fig. 4.5a, inset) are due to the waves' reverberations traveling through the pipes; the following pressure decrease phase is due to the dilatancy of the interface as a consequence of normal stress loss due to slip not compensated by the slower response time of the loading frame; and, finally, the subsequent pressure increase is due to the attempt of the pump to re-pressurize the circuit in reaction to the loss of pressure due to the fluid escaping through the lateral surfaces of the specimen ($x_3 = \pm \text{thickness}/2$). This behavior is not observed in the rapid pressure ramp-up scenario (Fig. 4.5b). We speculate that there are two possible reasons: first, the process is happening during a pressure increase with continuous provision of fluid from upstream; and second, the total accumulated slip is much lower, due to earlier rupture arrest, as opposed to the slow pressure ramp-up scenario.

The abrupt pressure ramp-up experiments are performed on the same specimen and in the same loading conditions as the previous case. The water pressure upstream of the valve and prior to its opening is set to the same level of 8.7 MPa at which the rupture spontaneously nucleated when a slow pressure ramp-up protocol was adopted (Fig. 4.5a). Upon the sudden opening of the valve, the pressure measured by the second transducer (Fig. 4.4b) shows an average rate of about 3.1×10^1 MPa/s over few hundreds of milliseconds (Fig. 4.5b). In these conditions, the rupture nucleation occurs at 4.9 MPa (42% of the resolved normal stress), which is about 56% of the 8.7 MPa reached by adopting the slow pressure ramp-up protocol, suggesting that, under the same conditions, the rate

of injection plays a major role in promoting the nucleation of dynamic ruptures by considerably reducing both the pressure and the volume of fluid required for the rupture initiation.

Pressure Diffusion over the Interface

Pressure Tactile Sensor Film

In order to measure the pressure distribution over the interface, a gradual pressure ramp-up profile equivalent to that in Figure 4.5a is imposed to a specimen whose inclination angle is $\alpha = 0^\circ$ and where holes 0.5 mm in both diameter and depth are excavated on the bottom half of the interface (see Fig. 4.3 and section 4.2). A Fujifilm Prescale[®] tactile pressure-indicating sensor film is inserted within the interface and the specimen is loaded to the resolved normal stress of the corresponding $\alpha = 29^\circ$ case, i.e., $P = 15 \cos^2(29^\circ) = 11.5$ MPa. The portion of the film where the two surfaces are in contact chromatically saturates (a reminiscence of the population of asperities is visible by the small-scale color variation over the contact portion of the interface), while the locations corresponding to the holes do not experience any pressure variation and therefore no color change is induced. Upon then the injection of the pressurized fluid, the hole corresponding to the injection duct assumes coloration as soon as 2.4 MPa are exceeded. As the pore pressure at the injection duct gradually increases all the way up to 8.7 MPa (Fig. 4.5a), the coloration becomes more and more intense (Fig. 4.6).

After the experiment is completed and the pressure film has assumed its coloration, the color reading at each pixel is converted into pressure. At each hole, the pressure level is the resulting from the average of the five smallest values among themselves (Figs. 4.6 and 4.7). This is justified by the idea that the less colored portions of each hole (closer to its center) are minimally affected by small

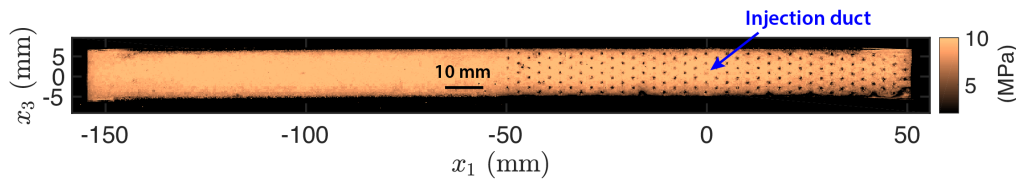


Figure 4.6: Pressure measurement from the Fujifilm tactile pressure-indicating sensor film. The sensor changes color as it experiences pressures in the range between 2.4 and 9.7 MPa. The specimen has been loaded to $P = 15 \cos^2(29^\circ) = 11.5$ MPa, which chromatically saturates the pressure film, except in correspondence to the holes (darker dots). The pore-pressure time history at the injection duct mimics that of the gradual ramp up (Fig. 4.5a), while the final distribution over the interface, corresponding to the same conditions the dynamic rupture occurred (at 8.7 MPa), is measured by the holes.

irregularities due to the interaction of the pressure film with the circular border of each hole, and therefore carry the actual pressure information. With time, as the fluid diffuses over the interface and the pressure level raises, the holes adjacent to the injection duct start experiencing this pressure increase, although so mildly that the color of the pressure film does not significantly change (Fig. 4.6). This suggests that the pore-pressure rapidly decays away from the injection location and, few millimeters away from it, its value falls below 2.4 MPa, which is the lower measurable bound for the tactile pressure film. Whenever the pore pressure drops below this limit, a value equal to the ambient pressure ($p_{\text{amb}} \approx 0.1$ MPa) has manually been imposed (Fig. 4.7).

Since the pressure film can only provide post-mortem scenarios, the rapid ramp-up protocol could not be reliably tested using this experimental configuration.

Pressure-Diffusion Model

A diffusive model is adopted to numerically estimate the pressure distribution over the interface given the knowledge of its time history at the injection site, measured by the pressure transducer downstream of the solenoid valve. The experimental results from the Fujifilm Prescale[®] tactile pressure-indicating sensor film are used as a benchmark.

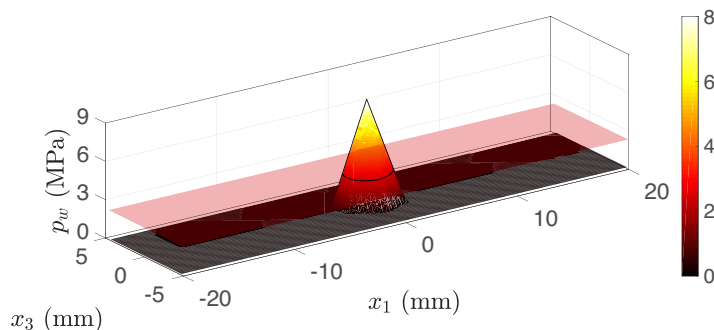


Figure 4.7: Pressure measurement corresponding to the 0.5-mm wide holes using the Fujifilm tactile pressure-indicating sensor film, derived from Figure 4.6. The pore pressure rapidly decays away from the injection duct due to the ambient pressure along the boundaries of the sample.

The combination of the fluid continuity equation and the Darcy's law, which relates the fluid flux with the pressure gradient in a saturated medium under steady state conditions and laminar flow (low Reynolds number), leads to a 2D transport equation for the fluid flow in thin layers (Detournay, 2004; Garagash and Detournay, 2000; Segall and Rice, 1995; Walder and Nur, 1984; Wong, Ko, and Olgaard, 1997; Zhang, Jeffrey, and Thiercelin, 2009):

$$\frac{\partial p}{\partial t} - c \nabla \cdot (\kappa \nabla p) = 0 \quad (4.2)$$

For the sake of simplicity, we linearize the problem by neglecting the dependence of permeability κ on the spatial location (and thus also on the pressure). In addition, the variation of both c and κ due to slow-slip-induced dilation has not been considered here (Segall and Rice, 1995).

$$\frac{\partial p}{\partial t} - \alpha_{\text{hy}} \nabla^2 p = 0 \quad (4.3)$$

where $\alpha_{\text{hy}} = c\kappa$ is the hydraulic diffusivity. An implicit Crank-Nicholson finite-difference scheme is adopted to numerically solve equation 4.3. The results are

summarized in Fig. 4.8, where a hydraulic diffusivity $\alpha_{hy} = 10^{-6} \text{ m}^2/\text{s}$ has been used.

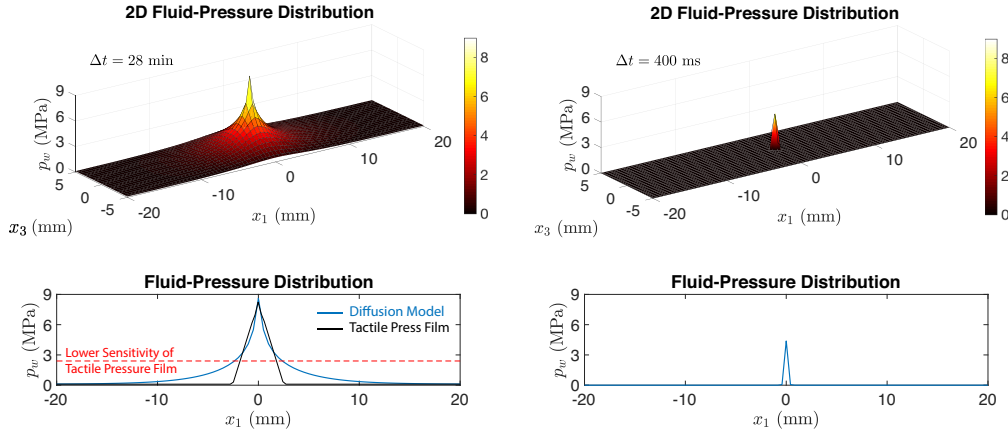


Figure 4.8: Fluid-pressure distribution over the interface at rupture initiation. The pressure distribution is estimated by numerically solving equation 4.3, where the pressure ramp-up profiles from Figure 4.5 are imposed at the node corresponding to the injection location, for the slow case (left) and the rapid one (right), respectively. The rapid decay of pressure away from the injection channel is due to the ambient-pressure boundary condition along the lateral sides of the interface. The bottom panels represent a slice through the plane $x_3 = 0$ and highlight the substantial different pressure distribution scenario under which the dynamic rupture nucleates.

In order to simulate the pressure diffusion over the interface, both the slow and rapid pressure ramp-up history profiles in Figure 4.5 are numerically imposed as a point source at the injection location. Figure 4.8 shows the computed 2D pressure distribution over the interface at the time when the rupture nucleates. Both cases are characterized by sharp gradients of pressure about the injection location, rapidly decaying away from it, although the fast ramp-up case (Figs.4.5b and 4.8b) exhibits steeper gradients.

Equation 4.1 can be re-arranged to find the corresponding critical value of pore pressure p^* for which, slip is initiated, assuming a peak (static) friction coefficient f_p :

$$p^* = \sigma_n - \frac{\tau}{f_p} = P \cos^2(\alpha) \left(1 - \frac{\tan(\alpha)}{f_p} \right) \quad (4.4)$$

If $P = 15$ MPa, $\alpha = 29^\circ$, and $f_p = 0.65$ (Rubino, Rosakis, and Lapusta, 2017), the slip is activated wherever the pore pressure exceeds the critical value $p^* = 1.7$ MPa over the interface. We emphasize that slip motion can be either stable (aseismic) or unstable (seismic), depending on whether the length of the slipping patch exceeds the nucleation size (see section 4.1). However, once the slip is initiated, the patches on the interface undergoing slip release shear stress, which is accumulated on the surrounding areas that are either locked or slipping at a slower rate. The slip-related stress redistribution gives rise to a highly heterogeneous problem, which cannot be solved analytically. We employ strain-gage measurements (see section 4.3) to experimentally explore this regime, and plan to explore the slip initiation in a future numerical study.

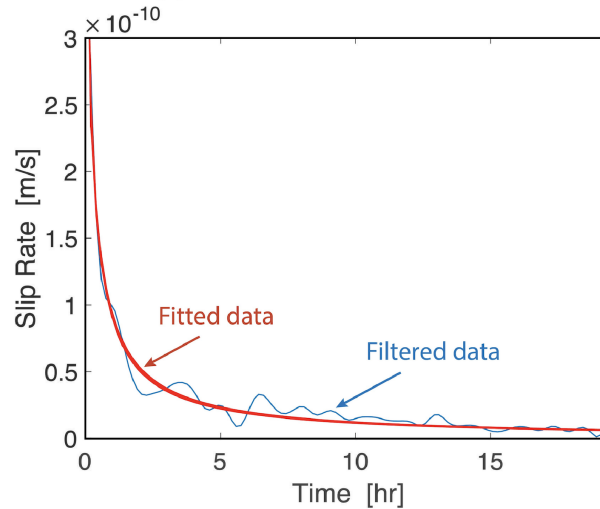


Figure 4.9: Slip rate temporal history of a loaded specimen. The blue curve represents the data obtained from quasi-static DIC measurements averaged and filtered, while the red curve is an exponential fitting, in compliance to the rate-and-state friction law. After the application of an external load of $P = 15$ MPa, the specimen is left untouched for the entire duration of the test. The slip rate spontaneously evolves from 3×10^{-10} m/s to 10^{-11} m/s. These values, despite being very small, prove that the interface is never fully locked.

The rate-and-state frictional formulation predicts that an interface is *always* slipping with rates that can range from quasi-static to dynamic (Di Toro et al., 2011; Marone, 1998; Scholz, 1998). As a consequence, the shear *stress* acting on a frictional surface always equals the shear *strength*. This formulation is supported by the experimental evidence. In order to explore the slip rate experienced by a sample over a 24-hour period, a specimen has been loaded up to $P = 15$ MPa and then left untouched for the entire duration of the test. Simultaneously, every 10 minutes, 5 frames are collected by an EO-5023M camera and then numerically averaged among each other to counteract the noise level. The fault-parallel displacement field, u_1 , has been derived via digital image correlation and, by time differentiation, also the velocity field, \dot{u}_1 . Assuming a homogeneous slip behavior along the interface, all the pixels just above and below the interface have been averaged in order to produce a single value of slip $\bar{\delta}$ and slip rate $\dot{\bar{\delta}}$ per image. This expedient is essential in order to counteract the noise level and obtain meaningful measurements at such low levels of slip (in the order of $1 \div 10 \mu\text{m}/\text{day}$) and slip rate (in the order of $10^{-11} \div 10^{-10}$ m/s). The temporal history of these values is reported in Figure 4.9, highlighting that the interface, despite experiencing a very small amount of slip and slip rate, is never fully locked. Moreover, the average slip rate $\dot{\bar{\delta}}$ continuously decreases from 3×10^{-10} m/s to 10^{-11} m/s, suggesting that a steady-state behavior is *not* achieved as a consequence of the evolving contact area of the micro-scale population of asperities, which is captured by the evolution of the state variable θ . This behavior is well described by the rate-and-state frictional formulation.

The measurement of slip-rate during slow slip tests presented in Figure 4.9 can be used to estimate the reference friction coefficient f_* within the rate-and-state framework as follows:

$$\tau \Big|_{10^{-9} \text{ m/s}} = \left[f_* + a \log \left(\frac{\dot{\delta}}{\dot{\delta}_*} \right) + b \log \left(\frac{\dot{\delta}_* \theta}{L} \right) \right] (\sigma_n - 0) \quad (4.5)$$

If $\dot{\delta}_* = 10^{-6}$ m/s, $a = 0.011$, $b = 0.016$, $L = 1 \mu\text{m}$, $\theta = 300$ s, $\sigma_n = P \cos^2(\alpha) = 11.5$ MPa and $\tau = P \sin(\alpha) \cos(\alpha) = 6.4$ MPa, this relationship can be solved for the reference value of the frictional coefficient $f_* = 0.54$ MPa that is required to sustain a slip rate of $\dot{\delta} = 10^{-9}$ m/s.

In this framework, the shear stress / strength required to achieve an instantaneous accelerated slip rate $\dot{\delta}$ of 10^{-4} m/s is:

$$\tau \Big|_{10^{-4} \text{ m/s}} = \left[f_* + a \log \left(\frac{\dot{\delta}}{\dot{\delta}_*} \right) + b \log \left(\frac{\dot{\delta}_* \theta}{L} \right) \right] (\sigma_n - p^*) \quad (4.6)$$

By adopting the same parameters, this relationship can be solved for the (upper bound) critical value of pressure $p^* = 2.1$ MPa that is required to induce an accelerated slip rate of $\dot{\delta} = 10^{-4}$ m/s. This pore pressure level is in good agreement with the one predicted by equation 4.4, suggesting that, under these conditions, activating accelerated slip motion requires less than 20% reduction of the effective normal stress.

Rapid Fluid-Injection and Locally-Elevated Slip Rate

An insight into the effects of rapid pressurization of the interface on slip can be obtained by considering the approximation of the rapid ramp-up profile by an instantaneous pressure change and how the associated strength, and hence stress drop, results in high, dynamic levels of slip rate that jump-start the rupture. The 2D elasto-dynamic relations allow the expression of the stress on the fault plane in terms of the slip history as:

$$\tau(x_1, t) = \tau_0(x_1, t) + g(x_1, t) - \frac{\mu}{2c_s} \dot{\delta}(x_1, t) \quad (4.7)$$

where $\mu = 1.2$ MPa is the shear modulus, $c_s = 1$ km/s is the shear wave speed, $\dot{\delta}$ is the slip rate, $\tau_0 = P \sin(\alpha) \cos(\alpha) = 6.4$ MPa is the initial shear stress, and $g(x_1, t)$ is a linear functional of the history of slip (Lapusta and Liu, 2009). If the interface is governed by the rate-and-state friction formulation, then the shear stress in equation 4.7 is assumed to be always equal to the frictional strength in equation 4.1 and, right before the fluid injection, the interface is not precisely locked, but rather creeping with negligible slip rates of the order of $\dot{\delta}_{\text{bef}} = 10^{-9}$ m/s (Fig. 4.9). Under such conditions, the second and third term in equation 4.7 are nearly equal to zero and:

$$\tau_{\text{bef}} = \tau_0 = f_{\text{bef}}(\sigma_n - 0) \quad (4.8)$$

where f_{bef} is the rate-and-state friction coefficient, and the pore fluid pressure p_{bef} is equal to zero. Let us assume that the pore pressure instantaneously increases from zero to its peak value of $p_{\text{aft}} = 4.9$ MPa from the rapid pressurization procedure. The resulting instantaneous balance of the shear strength and hence shear stress can be written as:

$$\tau_{\text{aft}} = \left\{ f_{\text{bef}} + a \log\left(\frac{\dot{\delta}_{\text{aft}}}{\dot{\delta}_{\text{bef}}}\right) \right\} (\sigma_n - p_{\text{aft}}) = \tau_0 - \frac{\mu}{2c_s} \dot{\delta}_{\text{aft}} \quad (4.9)$$

where $a = 0.011$ quantifies the direct effect of the rate-and-state friction and the functional g is assumed to be instantaneously zero, as would be the case for uniform slip. Solving numerically for $\dot{\delta}_{\text{aft}}$ with the direct effect included gives a value of 1.2 m/s. Ignoring the direct effect in the rate-and-state formulation, the predicted slip rate associated with an instantaneous pore-pressure increase is higher, since the energy needed for the direct effect is now available, according to this simplified model, for slipping:

$$\dot{\delta} = \frac{2c_s}{\mu} [\tau_0 - f_p(\sigma_n - p_{\text{aft}})] = 3.5 \text{ m/s} \quad (4.10)$$

These slip-rate estimates correspond to the 1-mm length scale of the duct. We notice that the actual slip rates should be somewhat lower than the predicted ones due to the non-instantaneous pore pressure increase. As a result, a non-uniform stress and slip would activate the stress-distributing functional g , ultimately penalizing the slip rate term of equation 4.9. Still, these estimates explain the dramatic initiation of the rupture in the scenario of fast pore-pressure increase, with essentially no wetting of the interface beyond the injection site. Such a high slip rate likely induces a dramatic dynamic weakening of the friction coefficient due to flash heating within several microns of slip (Rubino, Rosakis, and Lapusta, 2017), which, although local, is enough to initiate the dynamic rupture. This argument explains the considerably reduced nucleation length associated with the rapid pressure ramp-up scenario compared to the slow one.

Imaging the Fluid Diffusion

In order to track the fluid profile as it diffuses over the interface, a series of snapshots of the interface have been taken through the transparent back side of the specimen (Figs. 4.2b and 4.10). In the slow pressure ramp-up scenario, the rupture nucleates when the wetted portion of the interface reaches an average length of 74 mm, from the 1-mm initial one. Compared to our diffusion model (Fig. 4.8), the fluid seems to spread more rapidly in the actual test, likely because the dependence of permeability on the slip process is ignored in the modeling. Note that, prior to initiating the external loading phase, about a centimeter of air is left on top of the water meniscus, leaving about $3.1 \times 10^{-8} \text{ m}^3$ of volume of (compressible) air, at ambient pressure ($p_{\text{amb}} \approx 0.1 \text{ MPa}$). This procedure is adopted in order to avoid, during the far-field loading phase, squeezing a small

quantity of water from the thin channel onto the interface prior to the application of any pressure to it, due to the compression of the o-ring at the bottom of the specimen (see section 4.2). After the desired far-field load is reached and the absence of liquid on the interface is confirmed, the gradual pressurization of the water can begin, which drives the water diffusion over the interface. This lubrication problem (Detournay, 2004; Garagash and Detournay, 2000; Miller et al., 2004; Segall and Rice, 1995; Walder and Nur, 1984; Zhang, Jeffrey, and Thiercelin, 2009) is characterized by a highly non-uniform pressure decay from the peak value at the injection location outwards towards the ambient pressure lateral boundaries (Fig. 4.8).

Due to the non-uniformity of the pressure profile within the wet portion of the interface, it is not appropriate to directly compare the length of this region with the nucleation length estimates obtained under the assumption of a uniform effective stress. However, the wet portion of the interface represents an upper bound of the nucleation size and, most importantly, allows a direct comparison between the two nucleation modes under investigation: the slow and the rapid one. From the Rice and Ruina, 1983 formulation, h^* lies in the range between 25 and 120 mm, if a uniform fluid pore pressure p is considered in the range of 1 to 9 MPa (the higher value associated with the lower length), a normal stress σ_n of 11.5 MPa, a shear modulus μ of 1.2 GPa, a Poisson's ratio ν of 0.39, and rate-and-state parameters a , b , and L of 0.011, 0.016, and 1 μm respectively (Lu, 2009). By assuming the Rubin and Ampuero, 2005 formulation, h^* falls in the range between 70 and 320 mm, for the same choice of parameters. Hence, the 74-mm length of the wetted portion of the interface for the slow pore pressure increase case is broadly consistent with the theoretical estimates of the nucleation size. More detailed analysis of the nucleation procedure and nucleation sizes for non-uniform effective stress distributions will be explored in future numerical studies.

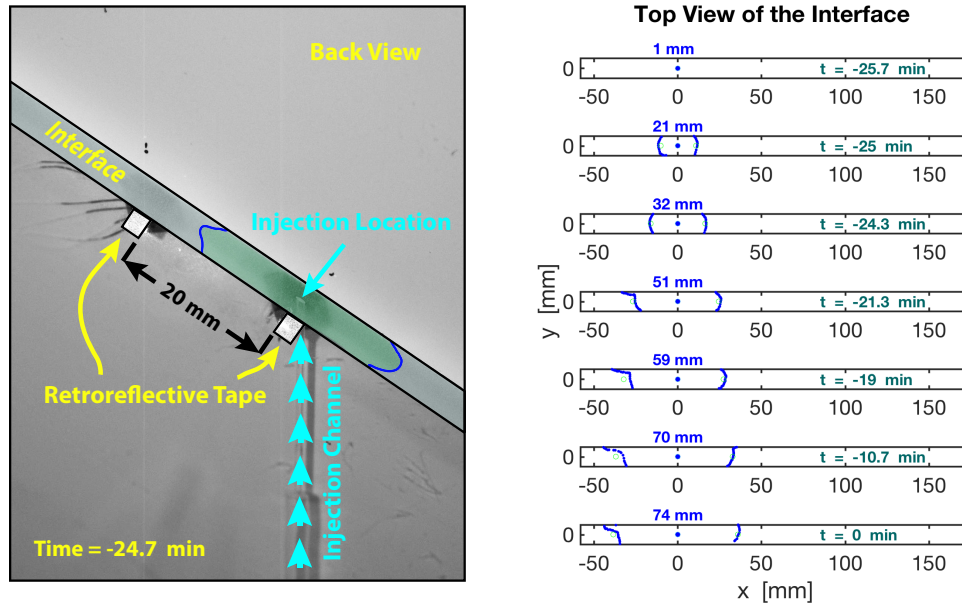


Figure 4.10: Fluid diffusion on the interface driven by pressure gradient. (left) Snapshot of the back side of the specimen (Fig. 4.2b) during a slow pressure ramp-up (Fig. 4.5a). For sake of clarity, we present a snapshot from another test, where no pattern for DIC was applied over the interface and the strain gages have been placed on the front side of the specimen. Instead, two $1 \times 1\text{-mm}^2$ squares of retro-reflective tape are positioned corresponding to the strain gages on the back side. The wet portion of the interface has been enhanced and enclosed into blue lines for better visibility. (right) Top view of the interface for the case corresponding to the test exhibited in Figure 4.5a. The wet portion (enclosed by the blue lines) is shown at several temporal instances, indicated by the green label on the right-hand side. Its average length is indicated in millimeters just above the corresponding case, and, at rupture initiation ($t = 0$), amounts to 74 mm.

In order to record the rupture initiation in the rapid pressure ramp-up scenario, in analogy to the result shown in Figure 4.10, a Shimadzu HPV-X high-speed camera, capable of resolving the millisecond time scale, has been employed. Interestingly, at rupture initiation, no fluid is visible on the interface, indicating that the thin volume of air above the water meniscus in the fluid channel acts itself as a (compressible) fluid by transmitting the overpressure to the interface above it. The presence of water on the interface becomes visible about 1 ms after the initiation. It is difficult to estimate a characteristic length for the fluid (air) extension over the interface. However, it is clear that, in comparison

to the slow nucleation procedure, the quantity of fluid delivered to the interface is much smaller, which, in addition to the lower pressure required to initiate the rupture (Fig. 4.5), suggests that the concept of rupture-nucleation length must include a previously-unexplored rate dependency. Clearly, if the rate of injection is sufficiently fast, dynamic events can be triggered at much lower fluid pressures and smaller volumes of injected fluid.

Strain measurements unveil non-uniform slip leading to rupture nucleation

The adoption of strain rosettes enables the local reconstruction of the strain tensor over more than nine orders of magnitude in time. Under the linear-elastic plane-stress approximation, stresses can be derived from strains, where the low strain-rate material properties are used for the slow and accelerated slip scenarios and the high strain-rate properties for the dynamic one. Figures 4.11 and 4.12 show the shear τ_{12} (yellow), fault-normal σ_{22} (green) and fault-parallel σ_{11} (cyan) stresses over three time scales, from minutes on the left, to milliseconds in the center and microseconds on the right. The solid, brighter lines correspond to SG-0 and the dashed, darker lines to SG-20 (Fig. 4.4). As before, $t = 0$ corresponds to the initiation of the dynamic rupture.

The vertical far-field load (Fig. 4.2, yellow arrows) is applied at a constant rate of strain of $6.7 \times 10^{-5} \text{ s}^{-1}$. Upon reaching of the final level of 15 MPa, the system switches to the load-control mode, keeps the load constant, and the strain rates drastically diminish. At this point, the strain acquisition system is zeroed and the strain values are recorded. Thus, all strain (and stress) readings represent incremental values with respect to this initial condition. Under strain, the polymeric material undergoes slow viscoelastic relaxation. As a consequence, to keep the applied load constant, the loading frame continues to compress the specimen, giving rise to compressive vertical strains and, due to the Poisson's

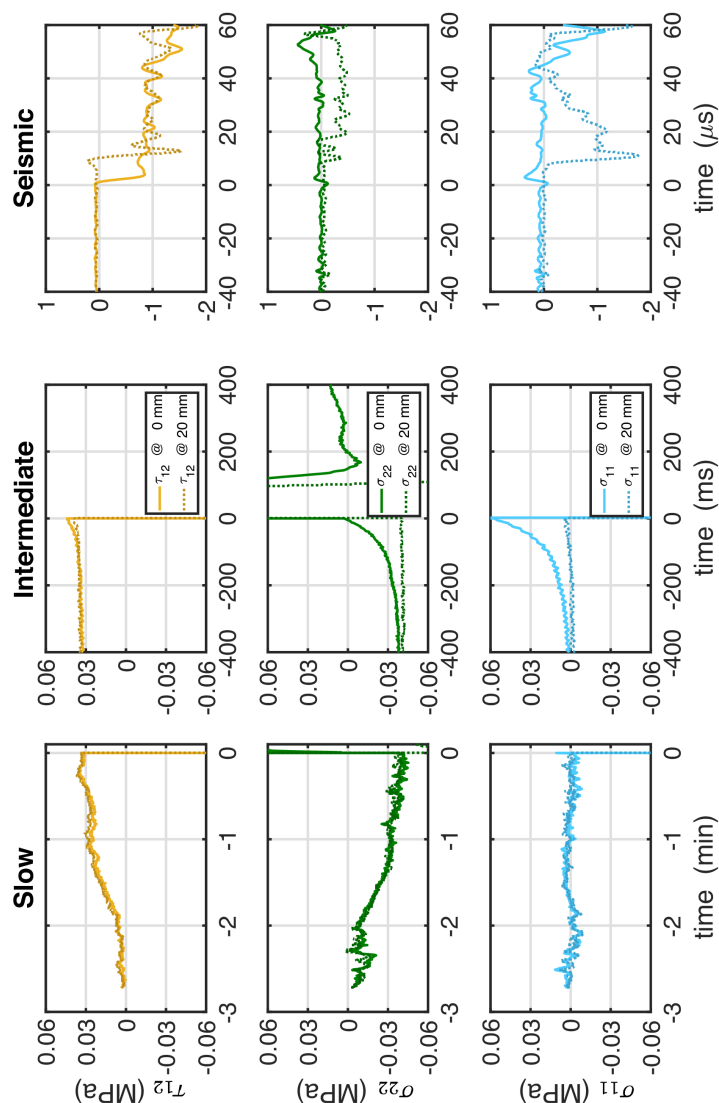


Figure 4.11: Stress time history during a rapid pressure ramp-up protocol. The shear (top row), fault-normal (center row) and fault-parallel (bottom row) stresses are shown over three time scales: minutes (left column), milliseconds (center column), and microseconds (right column), where the temporal origin coincides with the rupture initiation. Prior to the valve opening (left column) no fluid has been delivered to the interface yet, and strains and stresses accumulate as a consequence of the viscoelastic relaxation of the bulk polymer under load control mode. After the valve opening, in the few hundreds of milliseconds prior to the rupture initiation, the stress redistribution is related to the different slip behavior of patches with respect to the surrounding ones. After the rupture is triggered (right column), a laboratory-scale seismic event is recorded where left-lateral propagation arises.

effect, tensile strains in the horizontal direction. The strain gages measure these strains in a reference system aligned with the fault ($\alpha = 29^\circ$). Hence, the accumulation of the strain and the stress signals over several minutes prior to the initiation of the dynamic rupture embeds the contribution of the viscoelastic relaxation effects of our polymeric sample (Figs. 4.11 and 4.12, left columns). However, the difference the strain and stress signals between the two measurement stations is an indication of the different slip those locations experience. In fact, in order to understand the stress behavior at these locations, one needs to keep in mind the 2D nature of the interface (Fig. 4.4a). In particular, as the pressure is delivered to the interface, heterogeneous pressure and slip profiles arise, where patches at higher pressure tend to accumulate more slip. The shear stresses that are released are delivered to the surrounding patches, which, in turn, will experience more or less slip, depending on their local frictional strength. Locked patches, close to the slipping ones, experience shear and normal stress accumulation, while weaker patches slip more easily and accumulate less (or release) shear stress.

Stress variation at the lateral surface during a rapid pressure ramp-up nucleation protocol

We start by discussing the the stress changes (Fig. 4.11) from the strain measurements with the rapid pressure ramp-up nucleation protocol (Fig. 4.5b), as these results are simpler to interpret. In the few minutes required for the preparation to launch the test, a slight increase of all stress components is observable. The strain-gage stations – SG-0 and SG-20 – closely agree with each other and, since no fluid is injected on the interface yet (the valve is closed), the displayed values are only due to viscoelastic relaxation. Upon the opening of the solenoid valve, a sharp water pressure profile, developing over several tens to

few hundreds of milliseconds (Fig. 4.5b), is delivered to the interface through the 1-mm diameter injection duct. As a consequence, slip quickly accelerates at the injection location, with slip-rate values of the order of several meters per second, as estimated by the analysis under the assumption of instantaneous pore-pressure increase (see section 4.3). Such high levels of slip rate should induce the slip motion to rapidly propagate to locations further away from the injection location and, in particular, towards the lateral surface, where the SG-0 measurement station is placed. However, the pore pressure there is considerably lower than at the injection location (see sections 4.3 and 4.3), therefore SG-0 is frictionally stronger and undergoes smaller accelerated slip motion. As a result, the shear stress τ_{12} is accumulated there, however, the fault-normal one σ_{22} is released as a testimony that the patch about the SG-0 measurement station is itself undergoing slip (Fig. 4.11, central column, solid brighter line). The fault-parallel stress σ_{11} being positive suggests that the accelerating slip is inducing a tensile lobe at SG-0 (Mello, Bhat, and Rosakis, 2016; Mello et al., 2010), indicating that the accelerated slip has been nucleated in the positive x_1 -direction. These effects are, however, very small and are responsible for stress variations of the order of 5×10^{-2} MPa at most. The accelerated slip quickly decays away from the injection location and is barely experienced by the SG-20 station (Fig. 4.11, central column, dashed darker line). After the dynamic rupture initiates (Fig. 4.11, right column), at SG-0 the compressional and extensional lobes arising on either side of the rupture tip (Mello, Bhat, and Rosakis, 2016; Mello et al., 2010) cancel out due to anti-symmetry, resulting in the absence of significant variations of σ_{11} and σ_{22} (Fig. 4.11, right column, middle and bottom panels, brighter lines). The small tensile σ_{11} signal suggests that the rupture nucleates closely to SG-0, yet in the positive x_1 -direction, in agreement to what was already observed in the accelerated-slip phase. Conversely, the SG-20 station (dashed darker lines) does experience the compressional lobe, which

induces compressive fault-parallel strain ε_{11} and, due to Poisson's effects, tensile fault-normal strain ε_{22} , reflected in the corresponding stresses (right column, middle and bottom panels). Interestingly, the fault-parallel stress σ_{11} (bottom panel) exhibits a pulse-like behavior and the fault-normal stress σ_{22} (middle panel) becomes initially compressive. The shear components (top panel) for both stations – SG-0 and SG-20 – are characterized by an initial small increase (particularly visible at the SG-20 station), likely corresponding to the direct effect of the rate-and-state friction and peak value of the friction coefficient, followed by a substantial decrease, corresponding to the frictional weakening adjacent to the rupture tip (Rubino, Rosakis, and Lapusta, 2017), which can also be interpreted as an analog to a cohesive zone (Freund, 1998; Rosakis, 2002; Samudrala, Huang, and Rosakis, 2002a). By tracking the peaks of these quantities, separated by approximately $\Delta t = 8.8 \mu\text{s}$, and using the knowledge of the distance between the measurement stations of about $\Delta x = 20 \text{ mm}$, the projection of the rupture speed onto the lateral surface in its initial phase of propagation can be computed as $V_r = \Delta x / \Delta t = 2.27 \text{ km/s}$. By now considering the time interval $\Delta t^{(s)}$ of the shear stress to decay from the peak value to the residual one, the corresponding cohesive zone (CZ) size can be approximately computed as $\Delta x^{(CZ)} = V_r \Delta t^{(s)}$, yielding 8.2 and 8.6 mm for the SG-0 and SG-20 stations, respectively. After the rapid initial shear stress decrease, the dynamic level of the shear stress change continues to gradually decrease overall, indicating crack-like rupture propagation within the observation window; for a pulse-like rupture, the shear stress would increase at the end of the slip pulse.

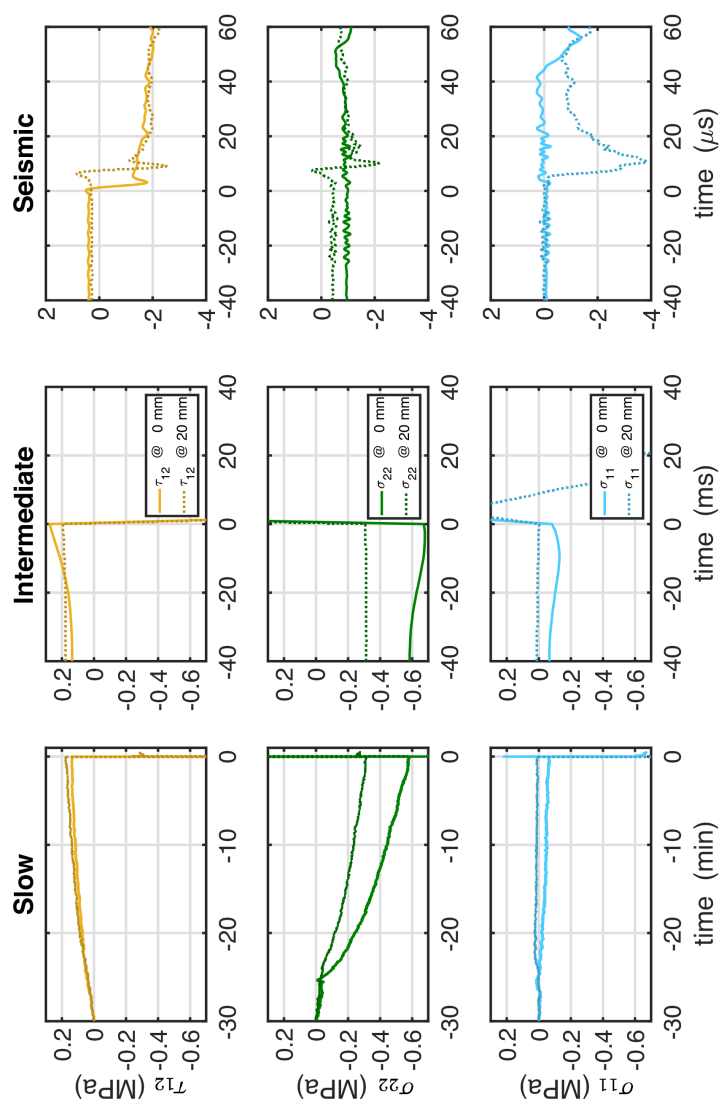


Figure 4.12: Stress time history during a slow pressure ramp-up protocol. The shear (top row), fault-normal (center row), and fault-parallel (bottom row) stresses are shown over three time scales: minutes (left column), milliseconds (center column), and microseconds (right column), where the temporal origin coincides with the rupture initiation. The delivery of pressurized fluid begins approximately 27 minutes prior to the rupture initiation (left column), promoting slow slip. One must remember that strains and stresses partially accumulate as a consequence of the viscoelastic relaxation of the bulk polymer under load control mode. In the few hundreds of milliseconds prior to the rupture initiation, the stress redistribution is related to the different slip behavior of patches with respect to the surrounding ones. After the rupture is triggered (right column), a laboratory-scale seismic event is recorded where left-lateral propagation arises.

Stress variation at the lateral surface during a slow pressure ramp-up nucleation protocol

The stress values – converted from the strain measurements – for the gradual pressure ramp-up nucleation protocol (Fig. 4.5a) are presented in Figure 4.12. The fluid injection protocol is started about three minutes after the beginning of recording ($t \approx -27$ min), due to the initial preparation required prior to launching the test. During this pre-time, in similarity to the rapid ramp-up scenario (section 4.3 and Fig. 4.11, left column), the strain gages only record the viscoelastic relaxation of the material manifesting in strain due to the load control mode, and the measurements from the two stations are in mutual agreement. After the fluid injection phase begins, their measurements start deviating from each other, indicating pronounced injection-induced effects at the location of SG-0 compared to that of SG-20. As the fluid diffuses over the interface, the pore pressure increases and frictionally weakens the corresponding portion of the interface, endorsing slow slip. The propagation and amount of slip is governed by a complex interplay of three factors: **(a)** the weakening due to both fluid pressure and friction evolution; **(b)** the accumulation of shear stress τ_{12} on the portions of the interface that are adjacent to actively slipping patches; and **(c)** the redistribution of the normal load σ_{22} on the interface. Slipping patches weaken and transfer stress to the nearby areas, which first resist the slip but, as the shear stress accumulates and weakening progresses, also experience increased slip motion. Depending on the amount of slip in relation to that of the surrounding fault areas, portions of the interface either release shear stress or accumulate it. Hence, in order to interpret the experimental results, one needs to bear in mind both the pore pressure profile that is inhomogeneously building up with time on the interface and the resulting slip / shear stress interplay along the interface characterized by spatially and temporally varying frictional and pore-pressure

conditions. It is likely that, due to the significantly higher pore pressure, the portion of the interface around the injection location slips more than the adjacent areas. As a consequence, less shear stress (Fig. 4.12, left column, top panel) is accumulated at SG-0 which is closer to the injection location than SG-20. At the same time, the compressive fault-normal stress increases at both locations and more so at SG-0, likely because the fluid-induced and perhaps slip-induced dilation of the interface at the injection location transfers the normal stress to the surrounding areas, again more so to the closer location at SG-0.

In the few tens of milliseconds prior to the initiation of the dynamic rupture (Fig. 4.12, center column), our measurements indicate that the interface around the injection location experiences an acceleration of slip motion. The measurements closer to the injection location (SG-0) show more significant increase in shear stress, pointing to increasing slip nearby, while there is not much change at the farther location (SG-20), indicating that the acceleration is relatively local, less than 3 to 5 mm in diameter around the injection site. Note that the shear stress increase is more than an order of magnitude larger than that of the rapid pressure ramp-up scenario (Fig. 4.11, center column). There are similar increasing effects in the normal stress components.

After the dynamic rupture initiates (Fig. 4.12, right column), both measurement locations exhibit an initial increase in shear stress up to a peak value followed by a sudden release about twice as large as the one observed in the rapid pressure ramp-up protocol. By performing the same calculations as before, the initial rupture speed is computed as $V_r = 3.13$ km/s and the cohesive zone lengths $\Delta x^{(CZ)}$ are 9.8 and 8.8 mm for SG-0 and SG-20, respectively, similar to the case of the rapid pressure ramp-up. As in the previous case, the SG-0 station (solid brighter line) does not exhibit much variations of fault-parallel or normal stress, due to the bilateral anti-symmetric nature of the compressional and tensional

lobes at the rupture tip (Mello, Bhat, and Rosakis, 2016; Mello et al., 2010). On the other hand, SG-20 (dashed darker line) shows a variable profile, similar to the one of the previous case. One potential difference is that the fault-parallel stress component σ_{11} (bottom panel, dashed line) is non-zero throughout, in contrast to becoming zero briefly in the rapid ramp-up case. Once nucleated, the rupture produces approximately twice as much shear stress release (Fig. 4.12, right column) than the rapid ramp-up counterpart (Fig. 4.11, right column). As in the rapid pressure ramp-up scenario, after the initial rapid shear-stress decrease, the dynamic level of the shear-stress change continues to gradually decrease overall, indicating crack-like rupture propagation within the observation window, but with larger slip corresponding to the larger shear-stress variation.

Detection of a foreshock during a slow pressure ramp-up nucleation protocol

The third representative case presented in this manuscript is another slow pressure ramp-up nucleation scenario (Fig. 4.13), which exhibits a foreshock-like much smaller event before the dynamic rupture of the entire interface. The experiment has been performed on a different specimen. While most experiments under the same conditions are quite repeatable even for different specimens as a result of the same polishing and bead-blasting protocols the employed to produce repeatable surface conditions (Lu, 2009; Mello et al., 2010), sometimes we observe variations in the experimental outcomes under nominally the same conditions, likely due to small variations in the spatial distribution of the surface waviness and roughness. Due to the highly nonlinear nature of the friction instability that enters our problem (Lapusta and Liu, 2009), these small tribological differences can lead to substantial variations in the macroscopic behavior during the pressure-diffusion phase prior to the rupture initiation. In the experiment of Figure 4.13, differently from the previous case (section 4.3

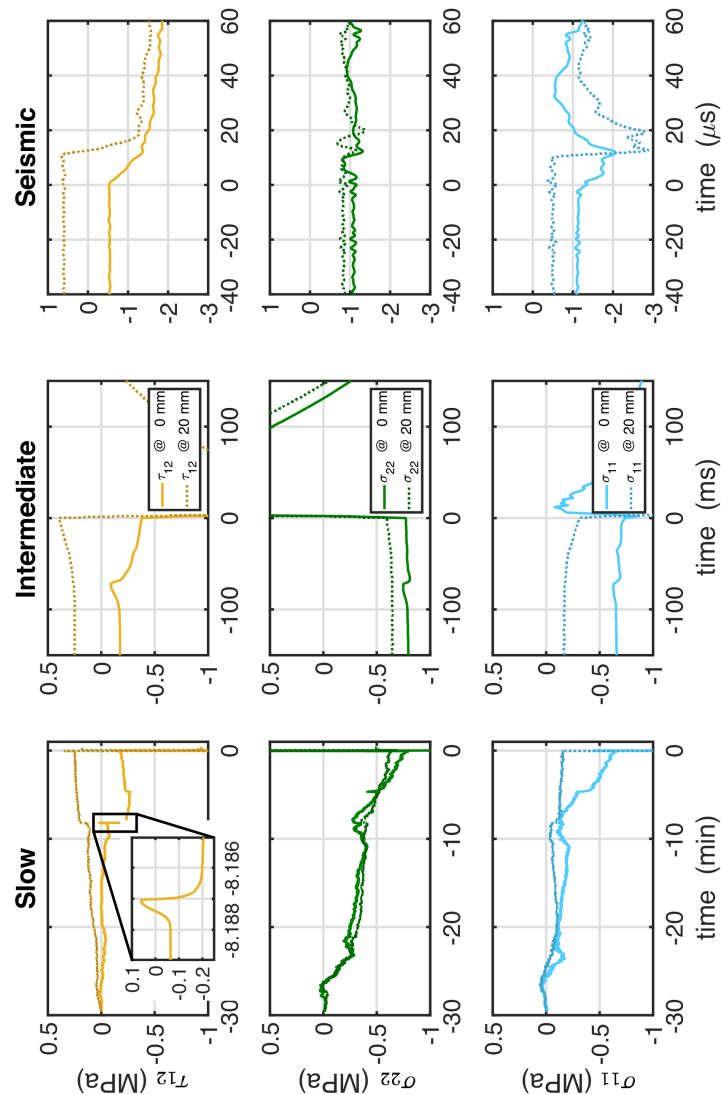


Figure 4.13: Stress time history during a slow pressure ramp-up protocol. The shear (top row), fault-normal (center row), and fault-parallel (bottom row) stresses are shown over three time scales: minutes (left column), milliseconds (center column), and microseconds (right column), where the temporal origin coincides with the rupture initiation. The delivery of pressurized fluid begins approximately 28 minutes prior to the rupture initiation (left column), promoting slow slip and few mini-foreshocks, one of which propagates slip all the way to the surface where the SG-0 station is located (inset in the top left panel). One must remember that strains and stresses partially accumulate as a consequence of the viscoelastic relaxation of the bulk polymer under load control mode. In the few hundreds of milliseconds prior to the rupture initiation, the stress redistribution is related to the different slip behavior of patches with respect to the surrounding ones. After the rupture is triggered (right column), a laboratory-scale seismic event is recorded where left-lateral propagation arises.

and Fig. 4.12), the strain gage SG-0 (solid brighter line) does not accumulate shear stress (Fig. 4.13, top left panel). This points to more slip developing near the sensor, and hence more slip overall around the injection site in this case, compared to the one in Figure 4.12. Approximately 8.2 minutes prior to the rupture initiation, the SG-0 experiences a relatively fast increase in shear stress of about 0.12 MPa followed by a release of about 0.26 MPa over about 42 ms (Fig. 4.13, inset in the top left panel). Such a rapid (milliseconds), but not dynamic (microseconds) shear-stress variation corresponds to a localized highly accelerated slip. The variation is not rapid enough to be dynamic at the location of the sensor, but the slip may have been dynamic over the injection site. Such a much smaller precursor event, occurring in spatial and temporal proximity to a later much larger rupture, is commonly referred to as a foreshock. The interaction between slow slip motion with the micro-scale asperities can trigger the foreshock activity (Bouchon, Durand, et al., 2013; Brodsky and Lay, 2014; Dodge, Beroza, and Ellsworth, 1995; Jones and Molnar, 1979; Kanamori and Stewart, 1976; Kato, 2012; McGuire, Boettcher, and Jordan, 2005). In addition, both the size of the nucleation region and the number of foreshocks is related to the fault-zone heterogeneity (Dodge, Beroza, and Ellsworth, 1995), which can also explain why small seismic events – such as the one under investigation – can develop without cascading into a main, larger event in the seismogenic zone (Higgins and Lapusta, 2016). The foreshock observed in our experiment clearly was unable to cascade into a larger event. The patch at SG-20 experiences a sharp corresponding shear-stress increase of about 0.07 MPa, indicating that the foreshock arrested before reaching that location. From the amount of stress drop and the size of the event, an approximate estimate of the total average slip can be computed by using the well-known analytical relation for planar cracks in an elastic medium (Eshelby, 1957; Kanamori and Anderson, 1975):

$$\Delta\tau = C\mu\frac{\bar{\delta}}{a} \quad (4.11)$$

where $\Delta\tau$ is the shear-stress drop, μ is the shear modulus, $\bar{\delta}$ is the average slip, a is the rupture radius, and C is the shape factor equal to $7\pi/16$ for circular cracks and similar for other similar shapes (Noda and Lapusta, 2013); we assume $C = 1$ for simplicity. In this case, $\Delta\tau = 0.14$ MPa based on the measurement, $\mu \approx 1$ GPa, a is bounded between 1 and 40 mm, the first case for a mini-rupture right at SG-0, the latter for a larger rupture just short of SG-20. From equation 4.11, the average slip $\bar{\delta}$ ranges between 0.14 and 5.6 μm . We are able to quantify such small amounts through the effect on the shear stress thanks to our strain acquisition setup, specifically optimized for these measurements. To achieve better estimates of the stress changes as the strain rates change during slip accumulation, we need a viscoelastic model to separate the stress changes from viscoelastic and slip effects, a subject of our future work.

In the few tens of milliseconds prior to the larger dynamic rupture initiation (Fig. 4.13, center column), the shear-stress variation points to an accelerated slip at the location of SG-0, as it can be inferred from the decreasing shear stress; while no (or minor) accelerated slip occurs at the location of SG-20, which exhibits a shear-stress increase.

The extra shear stress that SG-20 accumulated over SG-0 prior to the occurrence of the dynamic rupture is released as soon as the seismic motion is triggered and a larger initial shear-stress drop equilibrates the disparity (Fig. 4.13, right column, top panel). The extra drop of shear stress amounts to about 1.1 MPa. At SG-0, the fault-parallel (bottom panel) and fault-normal (middle panel) traces exhibit a non-negligible signal, indicating that the compressional and tensional lobe anti-symmetry has been lost there. This implies that the accelerated slip did not initiate exactly at the injection location ($x_1 = 0$). In fact, the compressive

fault-parallel lobe, in conjunction with the tensile fault-normal one, suggests that the rupture initiation location has shifted towards $x_1 < 0$. The rupture speed, calculated from the time of arrival of the peaks of the fault-parallel signals, amounts to $V_r = 2.44$ km/s. Since SG-0 has been a part of the nucleation region, the rupture did not necessarily propagated through this location in a traditional sense, and hence the estimated value is more uncertain than in other cases. Due to the peculiar shape of the shear traces in this scenario, the cohesive zone computation carries a certain degree of uncertainty. Their values amount to 20 mm for SG-20 and 40 mm for SG-0.

Note that the dynamic ruptures in all three cases show healthy crack-like behavior, indicating that, regardless of how the rupture is nucleated, its evolution under these conditions is similarly dynamic, although with different stress changes. The differences can hold clues to variations in friction resistance on interfaces with different pore pressure values, which we can explore through modeling.

DIC to capture surface motion during precursory activity

The full-field fault-parallel displacement map $u_1(\mathbf{x})$ (Fig. 4.14a) shows the local nature of the mini event in the center of the field of view, where the red color indicates movement towards the positive x_1 -direction, while the blue color towards the negative one. The color-saturated circular shapes of few-millimeters in size, clustered at the center of the interface and in particular right below it, are water droplets exiting the interface due to the elevated pressure gradient. Due to the frame acquisition rate of the camera (2 frames per minute), the output corresponds to an average value over a 30-s window; however, the foreshock occurs over just 42 ms (Fig. 4.13a, inset). For this reason, the fault-parallel velocity map $\dot{u}_1(\mathbf{x})$ (Fig. 4.14b) has been rescaled by a factor $30/0.042$, assuming that most of the slip occurred during the event. The slip velocity represents an

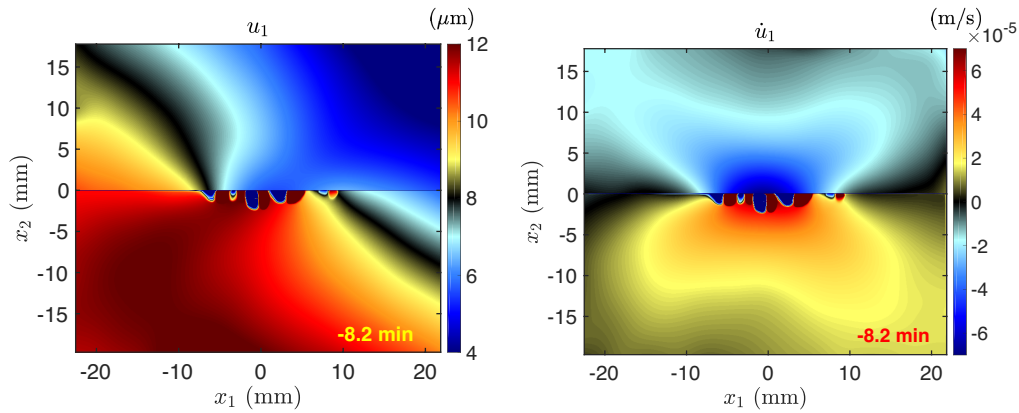


Figure 4.14: DIC full-field measurements after the foreshock event observed in Figure 4.13 (top left). The camera acquires pictures at a rate of one frame every 30 seconds. (left) Cumulative fault-parallel displacement u_1 . The upper half creeps leftwards (blue), while the bottom one creeps rightwards (red). At the center portion of the interface 5 – 6 μm of slip are cumulatively accumulated, decaying to less than 1 μm towards the side of the field of view. (right) Fault-parallel velocity \dot{u}_1 , at the net of rigid body motion, obtained by applying a first-order forward finite difference scheme on the frames just before and after the foreshock event. The velocity has been rescaled by a factor of 30/0.042, based on the knowledge of the temporal duration of the event from the strain gage measurement (Figure 4.13, top left, inset). During the foreshock event, the motion is concentrated at the center of the interface and rapidly decays away from it. The color-saturated shapes concentrated just below the center portion of the interface are water droplets escaping from the interface and causing the DIC algorithm to decorrelate (Sutton, Orteu, and Schreier, 2009).

estimate of an average value over the entire mini-event; however, it may have been much higher for a sub-portion of the slip period. This full-field map highlights the concentration of motion towards the center of the field of view, demonstrating that the slip propagated all the way to the lateral surface. DIC measurements of single foreshock events are most useful if the slip propagates all the way to the surface of the specimen. In the cases where the shear stress is accumulated rather than released at the surface, the DIC is unable to detect any significant displacement and the strain gages have proven to be the only technique able to capture, indirectly, such small events.

The full-field DIC measurements have been collected on the front side of

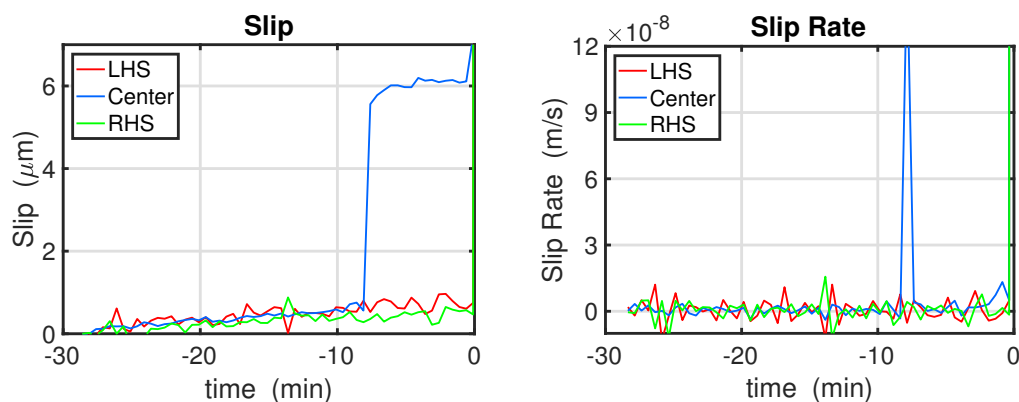


Figure 4.15: Slip (left) and slip-rate (right) temporal histories measured via DIC applied to the experiment presented in Figure 4.13. (left) The red and green lines indicate the slip close to the boundary of the field of view, respectively, along the interface, while the blue one corresponds to the center portion, for which the values underneath the interface have been taken below the water droplets (Fig. 4.14). In order to counteract the random noise and be able to measure such small signals, the values at each of the three locations have been averaged over 11 points (5 per side) along the x_1 -direction, both above and below the interface. Overall the interface accumulates less than a micron of slip during the fluid injection phase, with the exception of the center portion of it, which, at about -8.2 minutes, experiences the foreshock event accumulating $4.8 \mu\text{m}$ of slip over 42 ms. (right) The slip rate is computed from the slip using a first order forward finite difference scheme and averages to 10^{-9} m/s. Since the temporal resolution of the camera is of one frame every 30 s, it cannot resolve dynamic events such as the foreshock. The computed slip-rate peak value of 1.6×10^{-7} m/s therefore represents a lower bound. By rescaling this value by the factor of $30/0.042$, where 42 ms is the duration of the foreshock event measured by the SG-0 station (Fig. 4.13, top left, inset), the value of 1.1×10^{-4} m/s is obtained.

the specimen over a $45 \times 38 \text{ mm}^2$ field of view (Fig. 4.2a). These results refer to the foreshock observed in the third test presented in the previous section (Fig. 4.13). By analyzing the full-field fault-parallel displacement $u_1(\mathbf{x})$, the slip δ (Fig. 4.15a) can be computed as the difference between the values just above and below the interface (see section 4.2). In Figure 4.15, LHS and RHS refer to locations 0.56-mm away from the left and right borders of the field of view. The Center and the RHS locations coincide with the SG-0 and SG-20 measurement stations, but on the opposite face of the specimen (Fig. 4.2). Both LHS and RHS experience a gradual accumulation of average slip $\bar{\delta}$ of approximately $1 \mu\text{m}$ over

the entire duration of the pressurizing phase (Fig. 4.14a, red and green lines). The center location (blue line) follows a similar behavior until the occurrence of the foreshock event at about 8.2 minutes prior to the rupture nucleation. The sudden slip accumulation of $4.8 \mu\text{m}$ is in the range of the previous estimate between 0.14 and $5.6 \mu\text{m}$ using equation 4.11 and suggests that, for a shear-stress drop of 0.14 MPa (Fig. 4.13, inset in the top left panel), the slipping patch has a size of 34.3 mm . This size is consistent with the DIC measurements presented in Figure 4.14.

The average rate of slip $\dot{\delta}$ at all three locations (Fig. 4.15b) amounts to 10^{-9} m/s , with the exception of the foreshock event (blue line). If the slip rate is rescaled according to the temporal ratio of $30/0.042$, its value – during the foreshock – amounts to $1.1 \times 10^{-4} \text{ m/s}$.

4.4 Conclusions

As expected, our experiments show that fluid pore pressure promotes fault slip. The conditions under which dynamic ruptures are triggered have been investigated by exploring two fluid-injection scenarios: **(a)** a slow pressure ramp-up over approximately 30 minutes; and **(b)** a rapid pressure ramp-up over few hundreds of milliseconds. In the cases of rapid increase in pore pressure, the dynamic rupture initiates at about half the pressure level than that of the slow counterpart. Both a tactile pressure-indicating sensor film and simplistic diffusion model have been adopted to determine the pressure profile over the interface. They show that, in the slow pressure ramp-up scenario, the pressure gradually diffuses over the interface of the specimen away from the injection location, while in the rapid pressure ramp-up scenario, the pressure is elevated mostly in the immediate vicinity of the injection site.

The fluid diffusion and the associated pore pressure increase on the interface

have the dual effect of reducing the shear strength of the fault and of increasing the nucleation length. In the slow pressure ramp-up scenario, slow (stable) slip motion is induced as the result first, resulting in a slow, quasi-static nucleation slip process often observed in numerical models. The nucleation process is followed by the spontaneous initiation of the dynamic rupture. Prior to the dynamic event, the cumulative slip motion amounts to about $1 \mu\text{m}$ (measured on the lateral surface). We observe accelerated interface slip around the injection site in the several tens of milliseconds before the initiation of the dynamic rupture, expressed as the rapid redistribution of strains and stresses onto our strain measurement stations. A foreshock event, where the slip propagated all the way to the lateral surface, has been observed in one of the experiments and investigated. The presence of such foreshock events in some experiments, but not others highlights the sensitivity of the development of highly nonlinear frictional slip instability due to minute differences in the interface preparation of different specimen.

In contrast, the rapid-pressure-increase experiments always show similar nucleation behavior, with dynamic rupture initiating with small enough amounts of slow slip in a small enough area around the injection site that their effects cannot be observed at the lateral surface. These observations suggest much smaller nucleation lengths associated with the high injection rates, in addition to almost twice lower levels of pore pressures at the rupture initiation.

Once initiated, via either one of the nucleation protocols, the dynamic ruptures have similar behavior. One important difference is that, in the slow pressure ramp-up scenario, the dynamic rupture weakens the interface more, with larger shear stress changes. We speculate that this behavior may be related to either reduced friction coefficients associated to the lubricating effect due to the presence of water on the interface or, perhaps, to shear-heating effects such

as thermal pressurization.

Bibliography

- Abraham, Farid F and Huajian Gao (2000). “How fast can cracks propagate?” In: *Physical Review Letters* 84.14, p. 3113.
- Abraham, Farid F, Robert Walkup, et al. (2002). “Simulating materials failure by using up to one billion atoms and the world’s fastest computer: Brittle fracture”. In: *Proceedings of the National Academy of Sciences* 99.9, pp. 5777–5782.
- Ake, Jon et al. (2005). “Deep-injection and closely monitored induced seismicity at Paradox Valley, Colorado”. In: *Bulletin of the Seismological Society of America* 95.2, pp. 664–683.
- Anderson Jr, John David (2010). *Fundamentals of aerodynamics*. Tata McGraw-Hill Education. ISBN: 0070700125.
- Bauwens-Crowet, C (1973). “The compression yield behaviour of polymethyl methacrylate over a wide range of temperatures and strain-rates”. In: *Journal of Materials Science* 8.7, pp. 968–979.
- Bayart, Elsa, Ilya Svetlizky, and Jay Fineberg (2016). “Slippery but Tough: The Rapid Fracture of Lubricated Frictional Interfaces”. In: *Physical Review Letters* 116.19, p. 194301.
- Beeler, Nick et al. (2012). “Observed source parameters for dynamic rupture with non-uniform initial stress and relatively high fracture energy”. In: *Journal of Structural Geology* 38, pp. 77–89.

- Ben-David, Oded, Gil Cohen, and Jay Fineberg (2010). “The dynamics of the onset of frictional slip”. In: *Science* 330.6001, pp. 211–214.
- Ben-Zion, Yehuda (2008). “Collective behavior of earthquakes and faults: Continuum-discrete transitions, progressive evolutionary changes, and different dynamic regimes”. In: *Reviews of Geophysics* 46.4.
- Beroza, Gregory C and Satoshi Ide (2011). “Slow earthquakes and nonvolcanic tremor”. In: *Annual review of Earth and planetary sciences* 39, pp. 271–296.
- Blumenthal, W R et al. (2002). “Influence of temperature and strain rate on the compressive behavior of PMMA and polycarbonate polymers”. In: *AIP Conference Proceedings*. Vol. 620, pp. 665–668.
- Bouchon, Michel, Virginie Durand, et al. (2013). “The long precursory phase of most large interplate earthquakes”. In: *Nature Geoscience* 6.4, p. 299.
- Bouchon, Michel and Martin Vallée (2003). “Observation of long supershear rupture during the magnitude 8.1 Kunlunshan earthquake”. In: *Science* 301.5634, pp. 824–826.
- Broberg, K Bertram (1999). *Cracks and fracture*. Academic Press.
- Brodsky, Emily E and Thorne Lay (2014). “Recognizing foreshocks from the 1 April 2014 Chile earthquake”. In: *Science* 344.6185, pp. 700–702.
- Buades, Antoni, Bartomeu Coll, and Jean-Michel Morel (2008). “Nonlocal image and movie denoising”. In: *International Journal of Computer Vision* 76.2, pp. 123–139.
- Buehler, Markus J, Farid F Abraham, and Huajian Gao (2003). “Hyperelasticity governs dynamic fracture at a critical length scale”. In: *Nature* 426.6963, pp. 141–146.
- Capodagli, Julie and Roderic Lakes (2008). “Isothermal viscoelastic properties of PMMA and LDPE over 11 decades of frequency and time: a test of time–temperature superposition”. In: *Rheologica Acta* 47.7, pp. 777–786.
- Cappa, Frédéric, Yves Guglielmi, et al. (2005). “Hydromechanical interactions in a fractured carbonate reservoir inferred from hydraulic and mechanical measurements”. In: *International Journal of Rock Mechanics and Mining Sciences* 42.2, pp. 287–306.
- Cappa, Frédéric and Jonny Rutqvist (2012). “Seismic rupture and ground accelerations induced by CO₂ injection in the shallow crust”. In: *Geophysical Journal International* 190.3, pp. 1784–1789.

- Chen, Ting and Nadia Lapusta (2009). “Scaling of small repeating earthquakes explained by interaction of seismic and aseismic slip in a rate and state fault model”. In: *Journal of Geophysical Research: Solid Earth* 114.B1.
- Chen, W, F Lu, and M Cheng (2002). “Tension and compression tests of two polymers under quasi-static and dynamic loading”. In: *Polymer Testing* 21.2, pp. 113–121.
- Chou, S C, K D Robertson, and J H Rainey (1973). “The effect of strain rate and heat developed during deformation on the stress-strain curve of plastics”. In: *Experimental Mechanics* 13.10, pp. 422–432.
- Cochran, Elizabeth S et al. (2009). “Seismic and geodetic evidence for extensive, long-lived fault damage zones”. In: *Geology* 37.4, pp. 315–318.
- Cubas, Nadaya et al. (2015). “Numerical modeling of long-term earthquake sequences on the NE Japan megathrust: Comparison with observations and implications for fault friction”. In: *Earth and Planetary Science Letters* 419, pp. 187–198.
- Dahm, Torsten, Sebastian Hainzl, and Tomas Fischer (2010). “Bidirectional and unidirectional fracture growth during hydrofracturing: role of driving stress gradients”. In: *Journal of Geophysical Research: Solid Earth* 115.B12.
- Dalziel, Charles F (1946). “Dangerous electric currents”. In: *Transactions of the American Institute of Electrical Engineers* 65.8, pp. 579–585.
- (1972). “Electric shock hazard”. In: *IEEE spectrum* 9.2, pp. 41–50.
- Davies, E D H and S C Hunter (1963). “The dynamic compression testing of solids by the method of the split Hopkinson pressure bar”. In: *Journal of the Mechanics and Physics of Solids* 11.3, pp. 155–179.
- De Paola, Nicola et al. (2007). “A mechanical model for complex fault patterns induced by evaporite dehydration and cyclic changes in fluid pressure”. In: *Journal of Structural Geology* 29.10, pp. 1573–1584.
- Decker, R B et al. (2005). “Voyager 1 in the foreshock, termination shock, and heliosheath”. In: *Science* 309.5743, pp. 2020–2024.
- Detournay, E (2004). “Propagation regimes of fluid-driven fractures in impermeable rocks”. In: *International Journal of Geomechanics* 4.1, pp. 35–45.
- Di Toro, Giulio et al. (2011). “Fault lubrication during earthquakes”. In: *Nature* 471.7339, p. 494.
- Dieterich, James H (1981). “Constitutive properties of faults with simulated gouge”. In: *Mechanical behavior of crustal rocks: the Handin volume*, pp. 103–120.

- Dobson, David P, Philip G Meredith, and Stephen A Boon (2002). "Simulation of subduction zone seismicity by dehydration of serpentine". In: *Science* 298.5597, pp. 1407–1410.
- Dodge, Douglas A, Gregory C Beroza, and W L Ellsworth (1995). "Foreshock sequence of the 1992 Landers, California, earthquake and its implications for earthquake nucleation". In: *Journal of Geophysical Research: Solid Earth* 100.B6, pp. 9865–9880.
- Dougherty, M K et al. (2005). "Cassini magnetometer observations during Saturn orbit insertion". In: *Science* 307.5713, pp. 1266–1270.
- Dragert, Herb, Kelin Wang, and Thomas S James (2001). "A silent slip event on the deeper Cascadia subduction interface". In: *Science* 292.5521, pp. 1525–1528.
- Dunham, Eric M, Pascal Favreau, and J M Carlson (2003). "A supershear transition mechanism for cracks". In: *Science* 299.5612, pp. 1557–1559.
- Electrocution, Worker Deaths by (1998). "A Summary of NIOSH Surveillance and Investigative Findings". In: *US Department of Health and Human Services, DHHS (NIOSH) Publication* 98-131.
- Ellsworth, W L et al. (2004). "Near-field ground motion of the 2002 Denali fault, Alaska, earthquake recorded at pump station 10". In: *Earthquake Spectra* 20.3, pp. 597–615.
- Ellsworth, William L (2013). "Injection-induced earthquakes". In: *Science* 341.6142, p. 1225942.
- Eshelby, John D (1957). "The determination of the elastic field of an ellipsoidal inclusion, and related problems". In: *Proc. R. Soc. Lond. A*. Vol. 241. 1226. The Royal Society, pp. 376–396. ISBN: 0080-4630.
- Ferris, L P et al. (1936). "Effect of electric shock on the heart". In: *Electrical engineering* 55.5, pp. 498–515.
- Fialko, Y (2007). "Fracture and Frictional Mechanics–Theory". In:
- Fineberg, Jay and Eran Bouchbinder (2015). "Recent developments in dynamic fracture: some perspectives". In: *International Journal of Fracture* 196.1-2, pp. 33–57.
- Fish, Raymond M and Leslie A Geddes (2009). "Conduction of electrical current to and through the human body: a review". In: *Eplasty* 9.
- Fisk, Len A (2005). "Journey into the unknown beyond". In: *Science* 309.5743, pp. 2016–2017.

- Fleck, N A, W J Stronge, and J H Liu (1990). “High strain-rate shear response of polycarbonate and polymethyl methacrylate”. In: *Proceedings of the Royal Society of London A: Mathematical, Physical and Engineering Sciences*. Vol. 429, pp. 459–479.
- Foster, Mark et al. (2015). “The rate dependent tensile response of polycarbonate and poly-methylmethacrylate”. In: *Journal of Dynamic Behavior of Materials* 1.2, pp. 162–175.
- Freund, Lambert B (1998). *Dynamic fracture mechanics*. Cambridge university press.
- Frohlich, Cliff (2012). “Two-year survey comparing earthquake activity and injection-well locations in the Barnett Shale, Texas”. In: *Proceedings of the National Academy of Sciences* 109.35, pp. 13934–13938.
- Gabuchian, Vahe et al. (2017). “Experimental evidence that thrust earthquake ruptures might open faults”. In: *Nature* 545.7654, pp. 336–339.
- Gama, Bazle A, Sergey L Lopatnikov, and John W Gillespie (2004). “Hopkinson bar experimental technique: a critical review”. In: *Applied Mechanics Reviews* 57.4, pp. 223–250.
- Gan, Wei and Cliff Frohlich (2013). “Gas injection may have triggered earthquakes in the Cogdell oil field, Texas”. In: *Proceedings of the National Academy of Sciences* 110.47, pp. 18786–18791.
- Garagash, D and E Detournay (2000). “The tip region of a fluid-driven fracture in an elastic medium”. In: *Journal of Applied Mechanics* 67.1, pp. 183–192.
- Geddes, L A and L E Baker (1971). “Response to passage of electric current through the body”. In: *JAAMI: Journal of the Association for the Advancement of Medical Instrumentation* 5.1, pp. 13–18.
- Guglielmi, Yves et al. (2015). “Seismicity triggered by fluid injection–induced aseismic slip”. In: *Science* 348.6240, pp. 1224–1226.
- Gumbsch, Peter and Huajian Gao (1999). “Dislocations faster than the speed of sound”. In: *Science* 283.5404, pp. 965–968.
- Guo, Gaofeng, Wei Yang, and Y Huang (2003). “Supersonic crack growth in a solid of upturn stress–strain relation under anti-plane shear”. In: *Journal of the Mechanics and Physics of Solids* 51.11, pp. 1971–1985.
- Guozden, T M, E A Jagla, and M Marder (2010). “Supersonic cracks in lattice models”. In: *International Journal of Fracture* 162.1, pp. 107–125.
- Gurnett, D A and W S Kurth (2005). “Electron plasma oscillations upstream of the solar wind termination shock”. In: *Science* 309.5743, pp. 2025–2027.

- Hammam, Magda S and Rod S Baishiki (1983). “A range of body impedance values for low voltage, low source impedance systems of 60 Hz”. In: *IEEE Transactions on Power Apparatus and Systems* 5, pp. 1097–1105.
- Heap, M J et al. (2010). “Elastic moduli evolution and accompanying stress changes with increasing crack damage: implications for stress changes around fault zones and volcanoes during deformation”. In: *Geophysical Journal International* 183.1, pp. 225–236.
- Higgins, N and N Lapusta (2016). “Asperity-Type Potential Foreshock Sources Driven by Nucleation-Induced Creep within a Rate-and-State Fault Model”. In: *AGU Fall Meeting Abstracts*.
- Jones, Lucile M and Peter Molnar (1979). “Some characteristics of foreshocks and their possible relationship to earthquake prediction and premonitory slip on faults”. In: *Journal of Geophysical Research: Solid Earth* 84.B7, pp. 3596–3608.
- Jordan, J L et al. (2014). “Mechanics of particulate composites with glassy polymer binders in compression”. In: *Phil. Trans. R. Soc. A* 372.2015, p. 20130215.
- Jung, Haemyeong, Harry W Green II, and Larissa F Dobrzhinetskaya (2004). “Intermediate-depth earthquake faulting by dehydration embrittlement with negative volume change”. In: *Nature* 428.6982, p. 545.
- Kanamori, Hiroo and Don L Anderson (1975). “Theoretical basis of some empirical relations in seismology”. In: *Bulletin of the Seismological Society of America* 65.5, pp. 1073–1095.
- Kanamori, Hiroo and Gordon S Stewart (1976). “Mode of the strain release along the Gibbs fracture zone, Mid-Atlantic Ridge”. In: *Physics of the earth and planetary interiors* 11.4, pp. 312–332.
- Kato, Naoyuki (2012). “Dependence of earthquake stress drop on critical slip-weakening distance”. In: *Journal of Geophysical Research: Solid Earth* 117.B1.
- Keranen, Katie M et al. (2014). “Sharp increase in central Oklahoma seismicity since 2008 induced by massive wastewater injection”. In: *Science* 345.6195, pp. 448–451.
- Knauss, W G and W Zhu (2002). “Nonlinearly viscoelastic behavior of polycarbonate. I. Response under pure shear”. In: *Mechanics of Time-Dependent Materials* 6.3, pp. 231–269.
- Kouwenhoven, W B (1949). “Effects of electricity on the human body”. In: *Electrical engineering* 68.3, pp. 199–203.
- Lakes, Roderic S (2004). “Viscoelastic measurement techniques”. In: *Review of scientific instruments* 75.4, pp. 797–810.

- Lallement, Rosine et al. (2005). “Deflection of the interstellar neutral hydrogen flow across the heliospheric interface”. In: *Science* 307.5714, pp. 1447–1449.
- Lapusta, Nadia and Yi Liu (2009). “Three-dimensional boundary integral modeling of spontaneous earthquake sequences and aseismic slip”. In: *Journal of Geophysical Research: Solid Earth* 114.B9.
- Lee, S F and G M Swallowe (2006). “Quasi-static and dynamic compressive behaviour of poly (methyl methacrylate) and polystyrene at temperatures from 293 K to 363 K”. In: *Journal of Materials Science* 41.19, pp. 6280–6289.
- Li, Rongzhi (2000). “Time-temperature superposition method for glass transition temperature of plastic materials”. In: *Materials Science and Engineering: A* 278.1-2, pp. 36–45.
- Li, Zhouhua and John Lambros (2001). “Strain rate effects on the thermomechanical behavior of polymers”. In: *International Journal of Solids and Structures* 38.20, pp. 3549–3562.
- Liepmann, Hans Wolfgang and Anatol Roshko (1957). *Elements of gasdynamics*. Courier Corporation. ISBN: 0486419630.
- Lighthill, Michael James (2001). *Waves in fluids*. Cambridge University Press. ISBN: 0521010454.
- Limbach, Rene, Bruno P Rodrigues, and Lothar Wondraczek (2014). “Strain-rate sensitivity of glasses”. In: *Journal of Non-Crystalline Solids* 404, pp. 124–134.
- Liu, Yi and Nadia Lapusta (2008). “Transition of mode II cracks from sub-Rayleigh to intersonic speeds in the presence of favorable heterogeneity”. In: *Journal of the Mechanics and Physics of Solids* 56.1, pp. 25–50.
- Lu, H, X Zhang, and W G Knauss (1997). “Uniaxial, shear, and Poisson relaxation and their conversion to bulk relaxation: studies on poly (methyl methacrylate)”. In: *Polymer Engineering & Science* 37.6, pp. 1053–1064.
- Lu, Xiao (2009). *Combined experimental and numerical study of spontaneous dynamic rupture on frictional interfaces*. California Institute of Technology. ISBN: 1267467533.
- Lu, Xiao, Nadia Lapusta, and Ares J Rosakis (2007). “Pulse-like and crack-like ruptures in experiments mimicking crustal earthquakes”. In: *Proceedings of the National Academy of Sciences* 104.48, pp. 18931–18936.
- (2009). “Analysis of supershear transition regimes in rupture experiments: the effect of nucleation conditions and friction parameters”. In: *Geophysical Journal International* 177.2, pp. 717–732.

- Marder, M (2006). “Supersonic rupture of rubber”. In: *Journal of the Mechanics and Physics of Solids* 54.3, pp. 491–532.
- Marone, Chris (1998). “Laboratory-derived friction laws and their application to seismic faulting”. In: *Annual review of Earth and planetary sciences* 26.1, pp. 643–696.
- Marone, Chris, C Barry Raleigh, and C H Scholz (1990). “Frictional behavior and constitutive modeling of simulated fault gouge”. In: *Journal of Geophysical Research: Solid Earth* 95.B5, pp. 7007–7025.
- McGarr, Arthur et al. (2015). “Coping with earthquakes induced by fluid injection”. In: *Science* 347.6224, pp. 830–831.
- McGuire, Jeffrey J, Margaret S Boettcher, and Thomas H Jordan (2005). “Fore-shock sequences and short-term earthquake predictability on East Pacific Rise transform faults”. In: *Nature* 434.7032, p. 457.
- McLaskey, Gregory C and Brian D Kilgore (2013). “Foreshocks during the nucleation of stick-slip instability”. In: *Journal of Geophysical Research: Solid Earth* 118.6, pp. 2982–2997.
- McLaskey, Gregory C, Brian D Kilgore, et al. (2014). “Laboratory generated M-6 earthquakes”. In: *Pure and Applied Geophysics* 171.10, pp. 2601–2615.
- Mello, Michael, Harsha S Bhat, and Ares J Rosakis (2016). “Spatiotemporal properties of Sub-Rayleigh and supershear rupture velocity fields: Theory and experiments”. In: *Journal of the Mechanics and Physics of Solids* 93, pp. 153–181.
- Mello, Michael et al. (2010). “Identifying the unique ground motion signatures of supershear earthquakes: Theory and experiments”. In: *Tectonophysics* 493.3, pp. 297–326.
- Mello, M et al. (2014). “Reproducing the supershear portion of the 2002 Denali earthquake rupture in laboratory”. In: *Earth and Planetary Science Letters* 387, pp. 89–96.
- Miller, Stephen A et al. (2004). “Aftershocks driven by a high-pressure CO₂ source at depth”. In: *Nature* 427.6976, p. 724.
- Moy, Paul et al. (2003). “Dynamic stress-strain response and failure behavior of PMMA”. In: *ASME 2003 International Mechanical Engineering Congress and Exposition*, pp. 105–109.
- Mulliken, A D and M C Boyce (2006). “Mechanics of the rate-dependent elastic–plastic deformation of glassy polymers from low to high strain rates”. In: *International Journal of Solids and Structures* 43.5, pp. 1331–1356.

- Needleman, A (1999). “An analysis of intersonic crack growth under shear loading”. In: *Journal of Applied Mechanics* 66.4, pp. 847–857.
- Noda, Hiroyuki and Nadia Lapusta (2010). “Three-dimensional earthquake sequence simulations with evolving temperature and pore pressure due to shear heating: Effect of heterogeneous hydraulic diffusivity”. In: *Journal of Geophysical Research: Solid Earth* 115.B12.
- (2013). “Stable creeping fault segments can become destructive as a result of dynamic weakening”. In: *Nature* 493.7433, p. 518.
- Nosenko, V, S Zhdanov, and G Morfill (2007). “Supersonic dislocations observed in a plasma crystal”. In: *Physical Review Letters* 99.2, p. 25002.
- Okazaki, Keishi and Greg Hirth (2016). “Dehydration of lawsonite could directly trigger earthquakes in subducting oceanic crust”. In: *Nature* 530.7588, p. 81.
- Okubo, Paul G and James H Dieterich (1984). “Effects of physical fault properties on frictional instabilities produced on simulated faults”. In: *Journal of Geophysical Research: Solid Earth* 89.B7, pp. 5817–5827.
- Peng, Zhigang and Joan Gomberg (2010). “An integrated perspective of the continuum between earthquakes and slow-slip phenomena”. In: *Nature Geoscience* 3.9, p. 599.
- Petersan, Paul J et al. (2004). “Cracks in rubber under tension exceed the shear wave speed”. In: *Physical Review Letters* 93.1, p. 15504.
- Plazek, Donald J (1996). “1995 Bingham Medal Address: Oh, thermorheological simplicity, wherefore art thou?” In: *Journal of rheology* 40.6, pp. 987–1014.
- Qiao, Lan et al. (2016). “A Strain Rate Dependent Damage Viscoelastic Model for Granite”. In: 21.
- Rice, J R and A L Ruina (1983). “Stability of steady frictional slipping”. In: *Journal of Applied Mechanics* 50.2, pp. 343–349.
- Rice, James R (2001). “New perspectives on crack and fault dynamics”. In: *Mechanics for a New Millennium*. Springer, pp. 1–24.
- Rice, James R, Nadia Lapusta, and K Ranjith (2001). “Rate and state dependent friction and the stability of sliding between elastically deformable solids”. In: *Journal of the Mechanics and Physics of Solids* 49.9, pp. 1865–1898.
- Richeton, J, S Ahzi, K S Vecchio, F C Jiang, and R R Adharapurapu (2006). “Influence of temperature and strain rate on the mechanical behavior of three amorphous polymers: characterization and modeling of the compressive yield stress”. In: *International Journal of Solids and Structures* 43.7, pp. 2318–2335.

- Richeton, J, S Ahzi, K S Vecchio, F C Jiang, and A Makradi (2007). “Modeling and validation of the large deformation inelastic response of amorphous polymers over a wide range of temperatures and strain rates”. In: *International Journal of Solids and Structures* 44.24, pp. 7938–7954.
- Richeton, J, G Schlatter, et al. (2005). “A unified model for stiffness modulus of amorphous polymers across transition temperatures and strain rates”. In: *Polymer* 46.19, pp. 8194–8201.
- Rittel, D and A Brill (2008). “Dynamic flow and failure of confined polymethylmethacrylate”. In: *Journal of the Mechanics and Physics of Solids* 56.4, pp. 1401–1416.
- Roe, Philip L (1981). “Approximate Riemann solvers, parameter vectors, and difference schemes”. In: *Journal of computational physics* 43.2, pp. 357–372.
- Rosakis, A J, K Xia, et al. (2007). “Dynamic shear rupture in frictional interfaces: speeds, directionality, and modes”. In: *Treatise in Geophysics*, pp. 183–213.
- Rosakis, Ares J (2002). “Intersonic shear cracks and fault ruptures”. In: *Advances in Physics* 51.4, pp. 1189–1257.
- Rosakis, Ares J, Omprakash Samudrala, et al. (1998). “Intersonic crack propagation in bimaterial systems”. In: *Journal of the Mechanics and Physics of Solids* 46.10, pp. 1789–1814.
- Rosakis, Phoebus (2001). “Supersonic dislocation kinetics from an augmented Peierls model”. In: *Physical Review Letters* 86.1, p. 95.
- Rubin, A M and J-P Ampuero (2005). “Earthquake nucleation on (aging) rate and state faults”. In: *Journal of Geophysical Research: Solid Earth* 110.B11.
- Rubino, Vito, Ares John Rosakis, and Nadia Lapusta (2017). “Understanding dynamic friction through spontaneously evolving laboratory earthquakes”. In: *Nature Communications*, pp. 1–12. doi: [10.1038/ncomms15991](https://doi.org/10.1038/ncomms15991).
- Samudrala, O, Y Huang, and A J Rosakis (2002a). “Subsonic and intersonic mode II crack propagation with a rate-dependent cohesive zone”. In: *Journal of the Mechanics and Physics of Solids* 50.6, pp. 1231–1268.
- (2002b). “Subsonic and intersonic shear rupture of weak planes with a velocity weakening cohesive zone”. In: *Journal of Geophysical Research: Solid Earth* 107.B8.
- Sane, S B and Wolfgang G Knauss (2001). “On interconversion of various material functions of PMMA”. In: *Mechanics of Time-Dependent Materials* 5.4, pp. 325–343.

- Schapery, Richard Allan (1965). "A method of viscoelastic stress analysis using elastic solutions". In: *Journal of the Franklin Institute* 279.4, pp. 268–289.
- Scholz, Christopher H (1998). "Earthquakes and friction laws". In: *Nature* 391.6662, p. 37.
- Schwarzl, F and A J Staverman (1952). "Time-temperature dependence of linear viscoelastic behavior". In: *Journal of Applied Physics* 23.8, pp. 838–843.
- Segall, Paul and James R Rice (1995). "Dilatancy, compaction, and slip instability of a fluid-infiltrated fault". In: *Journal of Geophysical Research: Solid Earth* 100.B11, pp. 22155–22171.
- (2006). "Does shear heating of pore fluid contribute to earthquake nucleation?" In: *Journal of Geophysical Research: Solid Earth* 111.B9.
- Segall, Paul, Allan M Rubin, et al. (2010). "Dilatant strengthening as a mechanism for slow slip events". In: *Journal of Geophysical Research: Solid Earth* 115.B12.
- Singh, Raman P and Venkitanarayanan Parameswaran (2003). "An experimental investigation of dynamic crack propagation in a brittle material reinforced with a ductile layer". In: *Optics and Lasers in Engineering* 40.4, pp. 289–306.
- Siviour, C R, S M Walley, et al. (2005). "The high strain rate compressive behaviour of polycarbonate and polyvinylidene difluoride". In: *Polymer* 46.26, pp. 12546–12555.
- Siviour, Clive R and Jennifer L Jordan (2016). "High strain rate mechanics of polymers: a review". In: *Journal of Dynamic Behavior of Materials* 2.1, pp. 15–32.
- Slepyan, Leonid I (2002). *Waves*. Berlin: Springer, pp. 71–110.
- Song, B and W Chen (2004). "Loading and unloading split Hopkinson pressure bar pulse-shaping techniques for dynamic hysteretic loops". In: *Experimental Mechanics* 44.6, pp. 622–627.
- Sutton, Michael A, Jean Jose Orteu, and Hubert Schreier (2009). *Image correlation for shape, motion and deformation measurements: basic concepts, theory and applications*. Springer Science & Business Media.
- Svetlizky, Ilya, Elsa Bayart, et al. (2017). "Frictional resistance within the wake of frictional rupture fronts". In: *Physical Review Letters* 118.23, p. 234301.
- Svetlizky, Ilya and Jay Fineberg (2014). "Classical shear cracks drive the onset of dry frictional motion". In: *Nature* 509.7499, p. 205.

- Tschoegl, Nicholas W, Wolfgang G Knauss, and Igor Emri (2002). “Poisson’s ratio in linear viscoelasticity—a critical review”. In: *Mechanics of Time-Dependent Materials* 6.1, pp. 3–51.
- Uenishi, Koji and James R Rice (2003). “Universal nucleation length for slip-weakening rupture instability under nonuniform fault loading”. In: *Journal of Geophysical Research: Solid Earth* 108.B1.
- Van Gorp, Marnix and Jo Palmen (1998). “Time-temperature superposition for polymeric blends”. In: *Rheol Bull* 67.1, pp. 5–8.
- Walder, Joseph and Amos Nur (1984). “Porosity reduction and crustal pore pressure development”. In: *Journal of Geophysical Research: Solid Earth* 89.B13, pp. 11539–11548.
- Walley, S M and J E Field (1994). “Strain rate sensitivity of polymers in compression from low to high rates”. In: *DYMAT j* 1.3, pp. 211–227.
- Wang, Weineng, Zhiqiang Wang, and Xiao Peng (2013). “Effects of the Earth Current Frequency and Distortion on Residual Current Devices”. In: *Scientific Journal of Control Engineering* 3.6, pp. 417–422.
- Weertman, J (1967). “Uniformly moving transonic and supersonic dislocations”. In: *Journal of Applied Physics* 38.13, pp. 5293–5301.
- Wei, Shengji et al. (2015). “The 2012 Brawley swarm triggered by injection-induced aseismic slip”. In: *Earth and Planetary Science Letters* 422, pp. 115–125.
- Wong, Teng-Fong, Suz-Chung Ko, and David L Olgaard (1997). “Generation and maintenance of pore pressure excess in a dehydrating system 2. Theoretical analysis”. In: *Journal of Geophysical Research: Solid Earth* 102.B1, pp. 841–852.
- Wu, Hengyi, Gang Ma, and Yuanming Xia (2004). “Experimental study of tensile properties of PMMA at intermediate strain rate”. In: *Materials Letters* 58.29, pp. 3681–3685.
- Xia, Kaiwen, Ares J Rosakis, and Hiroo Kanamori (2004). “Laboratory earthquakes: The sub-Rayleigh-to-supershear rupture transition”. In: *Science* 303.5665, pp. 1859–1861.
- Xia, Kaiwen, Ares J Rosakis, Hiroo Kanamori, and James R Rice (2005). “Laboratory earthquakes along inhomogeneous faults: Directionality and supershear”. In: *Science* 308.5722, pp. 681–684.
- Xing, H Z et al. (2017). “High-Speed Photography and Digital Optical Measurement Techniques for Geomaterials: Fundamentals and Applications”. In: *Rock Mechanics and Rock Engineering*, pp. 1–49.

- Yee, A F and M T Takemori (1982). “Dynamic bulk and shear relaxation in glassy polymers. I. Experimental techniques and results on PMMA”. In: *Journal of Polymer Science Part B: Polymer Physics* 20.2, pp. 205–224.
- Zhang, Q B and Jian Zhao (2014). “A review of dynamic experimental techniques and mechanical behaviour of rock materials”. In: *Rock Mechanics and Rock Engineering* 47.4, pp. 1411–1478.
- Zhang, Xi, Robert G Jeffrey, and Marc Thiercelin (2009). “Mechanics of fluid-driven fracture growth in naturally fractured reservoirs with simple network geometries”. In: *Journal of Geophysical Research: Solid Earth* 114.B12.